

# Study of Critical Behaviour on Layered Organic Conductors

Tomotaka Uehara

Taniguchi Laboratory

Course in Material Science, Program in Science and Engineering  
Graduate School of Science and Engineering, Saitama University

March, 2016

## Preface

This dissertation is submitted for the degree of Doctor of Philosophy at Saitama University. The research described herein was conducted under the supervision of Professor H. Taniguchi in the Course in Material Science, Graduate School of Science and Engineering, Saitama University, between April 2011 and March 2016.

Parts of this work have been published in following reviewed publications:

- T. Uehara, M. Ito, H. Taniguchi, and K. Satoh, J. Phys. Soc. Jpn. **82**, 073706 (2013).
- M. Ito, T. Uehara, H. Taniguchi, K. Satoh, Y. Ishii, and I. Watanabe, J. Phys. Soc. Jpn. **84**, 053703 (2015).
- T. Uehara, M. Ito, J. Angel, J. Shimada, N. Komakine, T. Tsuchiya, H. Taniguchi, K. Satoh, K. Triyana, Y. Ishii, and I. Watanabe, J. Phys. Soc. Jpn. **85**, 024710 (2016).

## **Acknowledgements**

I would like to show my sincere appreciation to my supervisor Hiromi Taniguchi for his encouragement, knowledge, suggestion and support. I also like to thank all Professors of Department of Physics, Saitama University for fruitful suggestions and discussions.

I would like to appreciate Isao Watanabe from RIKEN-RAL and Yasuyuki Ishii from Shibaura Institute of Technology for their support and suggestions related to  $\mu$ SR and He-gas pressurised SQUID measurements.

Thanks also to all of the labmates, my friends, especially Fumi Suzaki from RIKEN, and to all the people I met during my research and study in Saitama University. I cannot accomplish this work without their help and support.

Finally, I take this opportunity to express my gratitude to my family for their unfailing support and love.

## Abstract

Over several decades, the strongly correlated system is one of the most attractive target systems for solid state physicist because of numerous physical properties they show. Since the strongly correlated system shows various states, the electrons with strong correlation are performing the most important role in such system. One of the best stages to investigate the effect of electronic correlation is the organic system because of its simpleness. In addition to that, the most part of organic material with strong correlation can be facilitated by chemical reaction, which leads to low-impurity samples which helps us to perform precise measurements.

The purpose of this research is to put a detailed investigation on the criticality of transitions on molecule-based strong correlation system,  $\kappa$ -(BEDT-TTF)<sub>2</sub>X. This system is known to show superconducting, magnetic and Mott transition. The criticalities of these three transitions are strongly related to fundamental questions in the field of solid state physics. However, the investigation of the criticality is not reported with a few exceptions.

In this dissertation, we report experimental results for these criticalities by  $\mu$ SR and magnetisation measurements. We succeed in clarifying several points such as i) Critical exponent of Mott transition in quasi-two-dimensional system probed by thermodynamic quantity, ii) Criticality of true (zero-field) magnetic ordering in  $\kappa$ -(BEDT-TTF)<sub>2</sub>X, and iii) Criticality of superconducting fluctuation which can be regarded as a precursor of superconductivity. Among them, we found that the Mott transition in this system has critical exponents which never observed by thermodynamic quantity, and that agrees to the theoretical prediction of quantum-Mott transition. This behaviour considered as a result of the low-temperature critical endpoint. In addition to that, we discovered that superconducting fluctuation (SCF) in this system has a rapid-growth nature which is an important clue to clarify its origin. We also find that magnetic ordering temperature in  $\kappa$ -(BEDT-TTF)<sub>2</sub>X shows intriguing behaviour while the system approaches to Mott transition, which may suggest the dipolar interaction as an origin of magnetic ordering.

# Contents

<b>1</b>	<b>Introduction</b>	<b>7</b>
1.1	Organic Conductor System $\kappa$ -(BEDT-TTF) <sub>2</sub> X . . . . .	7
1.2	Mott Transition . . . . .	13
1.3	Antiferromagnetic Transition . . . . .	15
1.4	Superconducting fluctuation . . . . .	17
<b>2</b>	<b>Experiments</b>	<b>19</b>
2.1	Magnetisation Measurement . . . . .	19
2.2	Helium-gas Pressurise Technique . . . . .	22
2.3	Muon Spin Relaxation/Rotation Measurement . . . . .	24
<b>3</b>	<b>Results for Mott transition</b>	<b>30</b>
3.1	Measurement under ambient pressure . . . . .	30
3.2	Measurement under pressure I—Phase Diagram . . . . .	32
3.3	Measurement under pressure II—Criticality of Mott transition . . . . .	37
<b>4</b>	<b>Results for Antiferromagnetic Transition</b>	<b>40</b>
4.1	$\kappa$ -(BEDT-TTF) <sub>2</sub> Cu[N(CN) <sub>2</sub> ]Cl . . . . .	40
4.2	$\kappa$ -(d8-BEDT-TTF) <sub>2</sub> Cu[N(CN) <sub>2</sub> ]Br . . . . .	46
4.3	$\kappa$ -(d8-BEDT-TTF) <sub>2</sub> Cu[N(CN) <sub>2</sub> ]Cl . . . . .	53
<b>5</b>	<b>Results for superconducting fluctuation</b>	<b>64</b>
5.1	$\kappa$ -(BEDT-TTF) <sub>2</sub> Cu[N(CN) <sub>2</sub> ]Br . . . . .	64
5.2	Pressurised $\kappa$ -(BEDT-TTF) <sub>2</sub> Cu[N(CN) <sub>2</sub> ]Cl . . . . .	69
<b>6</b>	<b>Remarks</b>	<b>74</b>
<b>A</b>	<b>Appendix</b>	<b>i</b>
A.1	Muon site estimation . . . . .	i
	<b>References</b>	<b>xiii</b>

## List of Abbreviations

$\kappa$ -(ET)<sub>2</sub>X  $\kappa$ -(BEDT-TTF)<sub>2</sub>X

$\kappa$ -Br  $\kappa$ -(BEDT-TTF)<sub>2</sub>Cu[N(CN)<sub>2</sub>]Br

$\kappa$ -Cl  $\kappa$ -(BEDT-TTF)<sub>2</sub>Cu[N(CN)<sub>2</sub>]Cl

$\kappa$ -NCS  $\kappa$ -(BEDT-TTF)<sub>2</sub>Cu(NCS)<sub>2</sub>

$\mu$ SR Muon Spin Relaxation/Rotation

AFI antiferromagnetic insulator

d8- $\kappa$ -Br  $\kappa$ -(d8-BEDT-TTF)<sub>2</sub>Cu[N(CN)<sub>2</sub>]Br

d8- $\kappa$ -Cl  $\kappa$ -(d8-BEDT-TTF)<sub>2</sub>Cu[N(CN)<sub>2</sub>]Cl

DM Dzyaloshinsky-Moriya

FFT fast Fourier transformation

PI paramagnetic insulator

PM paramagnetic metal

SC superconductivity

SCF superconducting fluctuation

# 1 Introduction

## 1.1 Organic Conductor System $\kappa$ -(BEDT-TTF)<sub>2</sub>X

The research target of this study is a group of the organic conductor, so-called  $\kappa$ -(BEDT-TTF)<sub>2</sub>X ( $\kappa$ -(ET)<sub>2</sub>X) that consist of BEDT-TTF (ET) molecule and monovalent anion X. When these systems crystallised, ET molecules will form monovalent radical cation [2BEDT-TTF]<sup>+</sup> due to its strong electro-donicity and this radical forms a charge-transfer salt with monovalent anion X<sup>-</sup>. In such crystallised state, the highest occupied molecular orbit (HOMO) band of ET become quarter-filled states and system can gain electric conductivity in a simplified scenario. Despite this scenario, some members of the  $\kappa$ -(ET)<sub>2</sub>X system show insulating behaviour. To describe this controversy, we need to take account of the interaction between carriers.

Hubbard model, which considers a lattice with a single electron on each site, can explain why these systems can show both metallic and insulating behaviour. Two electrons which sit on the same site would take a Coulomb repulsion  $U$  because of their negative charge (see figure 1.1.1). On the other hand, there is a transfer integral  $t$  between two neighbouring sites. In this modelling, each system has two characteristic physical quantities, Coulomb repulsion  $U$  and bandwidth  $W$ , and the behaviour of this electric system depends on the ratio,  $U/W$ .

In the case of a one-dimensional chain like figure 1.1.1, Bloch function with the tight-binding model can be written as

$$\Psi = c \sum_{j=0}^N e^{ijk_a} \psi_j \quad (1.1)$$

then the energy can be calculated as

$$E = \alpha + 2t \cos(ka), \text{ where } t = \int \psi_1^* H \psi_2 d\tau \quad (1.2)$$

, which indicates bandwidth  $W$  equals to  $4t$ . If bandwidth  $W$  exceeds Coulomb repulsion  $U$  ( $U/W < 1$ ), the system shows conducting behaviour simply because each carrier has enough energy to “overcome” Coulomb barrier from neighbouring

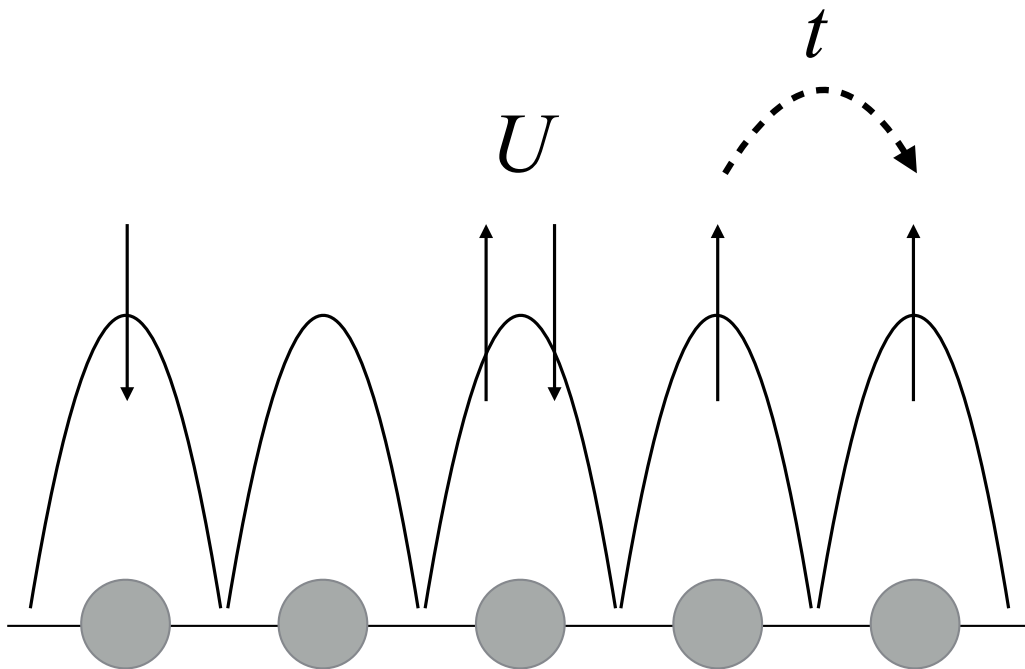


Figure 1.1.1: Schematic of Hubbard model in one-dimensional chain case. Grey circle corresponds to site, arrows indicates spin of each electron.

sites. Another situation is realised in a condition of  $U/W > 1$ . In this situation, each carrier sits on each site by the Coulomb repulsion and they cannot provide conductivity to the system.

This modelling describes  $\kappa$ -(ET)<sub>2</sub>X system quite well. As an example of the crystal structure of  $\kappa$ -(ET)<sub>2</sub>X, the crystal structure of  $\kappa$ -(BEDT-TTF)<sub>2</sub>Cu[N(CN)<sub>2</sub>]Cl ( $\kappa$ -Cl) is shown in figure 1.1.2a (Structural data is taken from ref. 8).  $\kappa$ -(ET)<sub>2</sub>X systems have layered structure in common, and intra-plane molecule stack pattern of  $\kappa$  phase are also shown in figure 1.1.2b. As its nature of charge-transfer salt as described above, each HOMO band of ET molecule in  $\kappa$ -(ET)<sub>2</sub>X has a quarter of hole. From the spatial distribution of ET molecule, each transfer-integral between each site on the molecule can be defined as figure 1.1.3a. In addition to that, two neighbouring ET molecules sit spatially close position in  $\kappa$ -phase stack. This placement makes molecules form a dimer and each dimer can be treated as a single

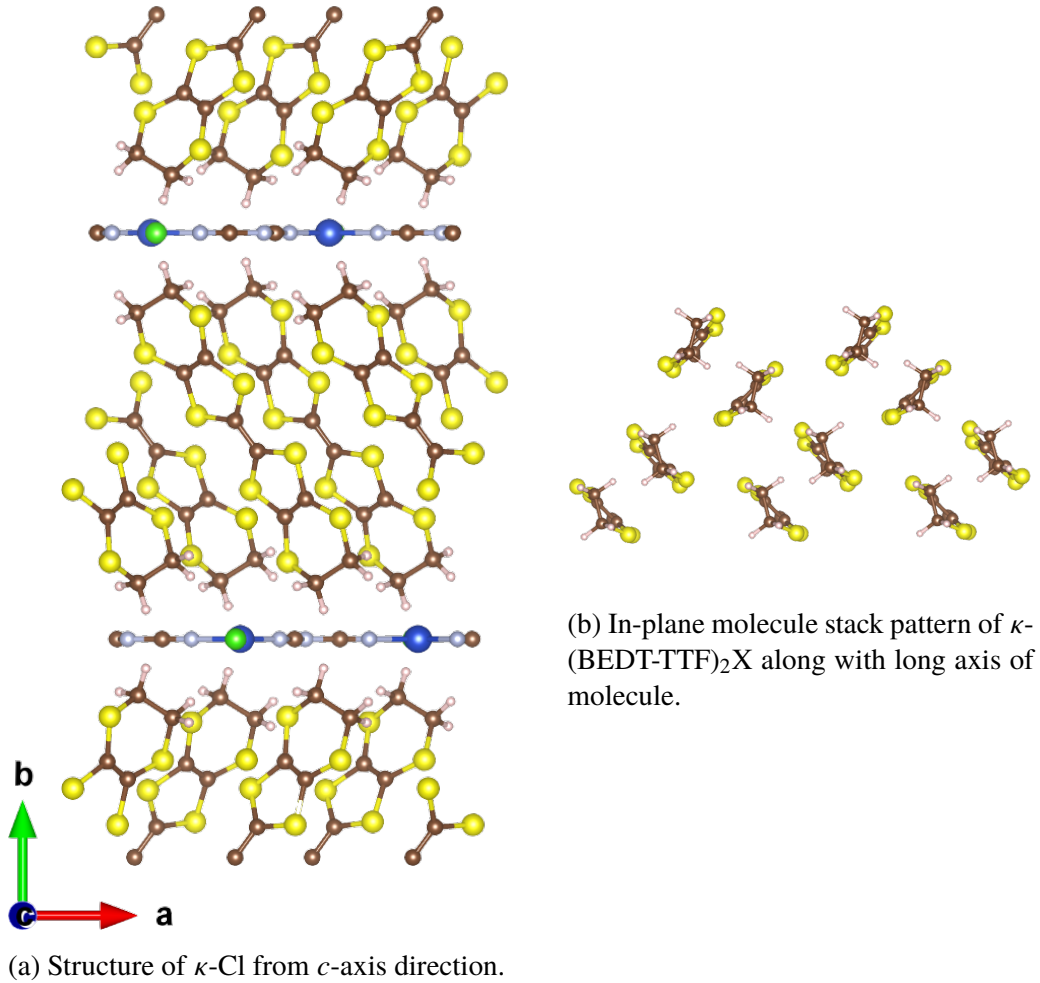


Figure 1.1.2: Crystal structure of  $\kappa$ -(BEDT-TTF) $_2$ Cu[N(CN) $_2$ ]Cl.

site with approximations as

$$t = (|t_p| + |t_q|)/2 \quad (1.3)$$

$$t' = t_{b2}/2 \quad (1.4)$$

and figure 1.1.3b showing schematic of dimerized ET in  $\kappa$ -(ET) $_2$ X. This dimerization changes the filling of their antibonding band of HOMO from quarter-filled to the half-filled situation. In such case, each ET dimer corresponds to site, and each hole on dimers is corresponded to carriers in the model, respectively.

To control bandwidth  $W$ , two common ways are adopted in the case of

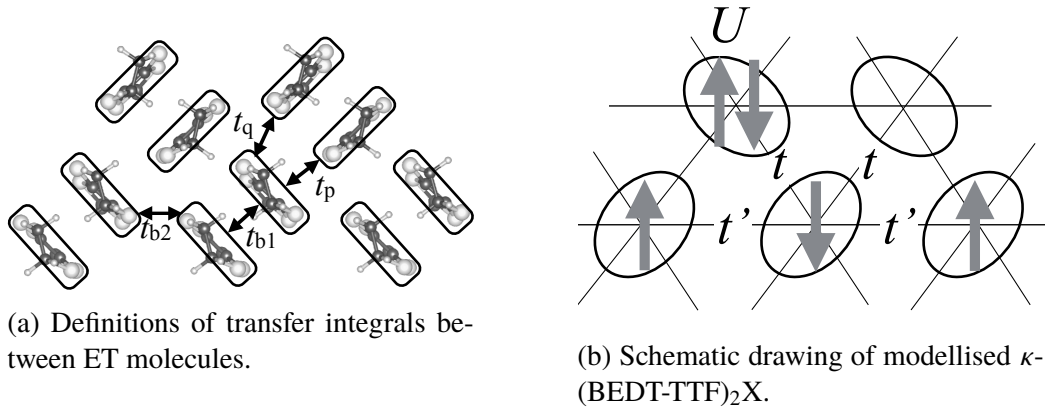


Figure 1.1.3: Modelisation of molecular plane of  $\kappa$ -(BEDT-TTF)<sub>2</sub>X.

the  $\kappa$ -(ET)<sub>2</sub>X system: physical pressure and deuteration of ethylene bases of BEDT-TTF. For this research, physical pressure is adopted to investigate Mott transition and SCF, and deuteration is used for investigation of magnetic ordering. It is worth noting that each material in the  $\kappa$ -(ET)<sub>2</sub>X system with different anion X<sup>-</sup> can be interpreted as a change of bandwidth. From such viewpoint, target materials in this dissertation are divided to two groups.  $\kappa$ -(BEDT-TTF)<sub>2</sub>Cu[N(CN)<sub>2</sub>]Br ( $\kappa$ -Br) corresponds to conducting ( $U < W$ ) situation and  $\kappa$ -(BEDT-TTF)<sub>2</sub>Cu[N(CN)<sub>2</sub>]Cl ( $\kappa$ -Cl),  $\kappa$ -(d8-BEDT-TTF)<sub>2</sub>Cu[N(CN)<sub>2</sub>]Cl (d8- $\kappa$ -Cl) and  $\kappa$ -(d8-BEDT-TTF)<sub>2</sub>Cu[N(CN)<sub>2</sub>]Br (d8- $\kappa$ -Br) correspond to insulating ( $U > W$ ) situation.

These target materials can be summarised by using the phase diagram of  $\kappa$ -Cl [9, 10], which was shown in figure 1.1.4 (lines in figure are based on series of data was taken from reference [10]). Each material of the  $\kappa$ -(ET)<sub>2</sub>X system can be situated on this phase diagram by comparing several physical properties such as transition temperature or calculated  $t/U$ . In this sense, it can be said we can apply “chemical pressure” by anion substitution. To show this effect, positions of  $\kappa$ -Br and  $\kappa$ -(BEDT-TTF)<sub>2</sub>Cu(NCS)<sub>2</sub> ( $\kappa$ -NCS) on this diagram were shown in figure 1.1.4 as grey broad arrows.

As shown in figure 1.1.4, the phase diagram of  $\kappa$ -(ET)<sub>2</sub>X was divided into five phases (antiferromagnetic insulator (AFI), superconductivity (SC), paramagnetic metal (PM), paramagnetic insulator (PI) and percolation phase between SC and AFI) by three phase transitions (**A**, **B**, **C**). Each of these three transitions should be

investigated to examine the critical behaviour of the bandwidth-controlled quasi-two-dimensional system. Next few subsections are dedicated to explaining the situation of each transition.

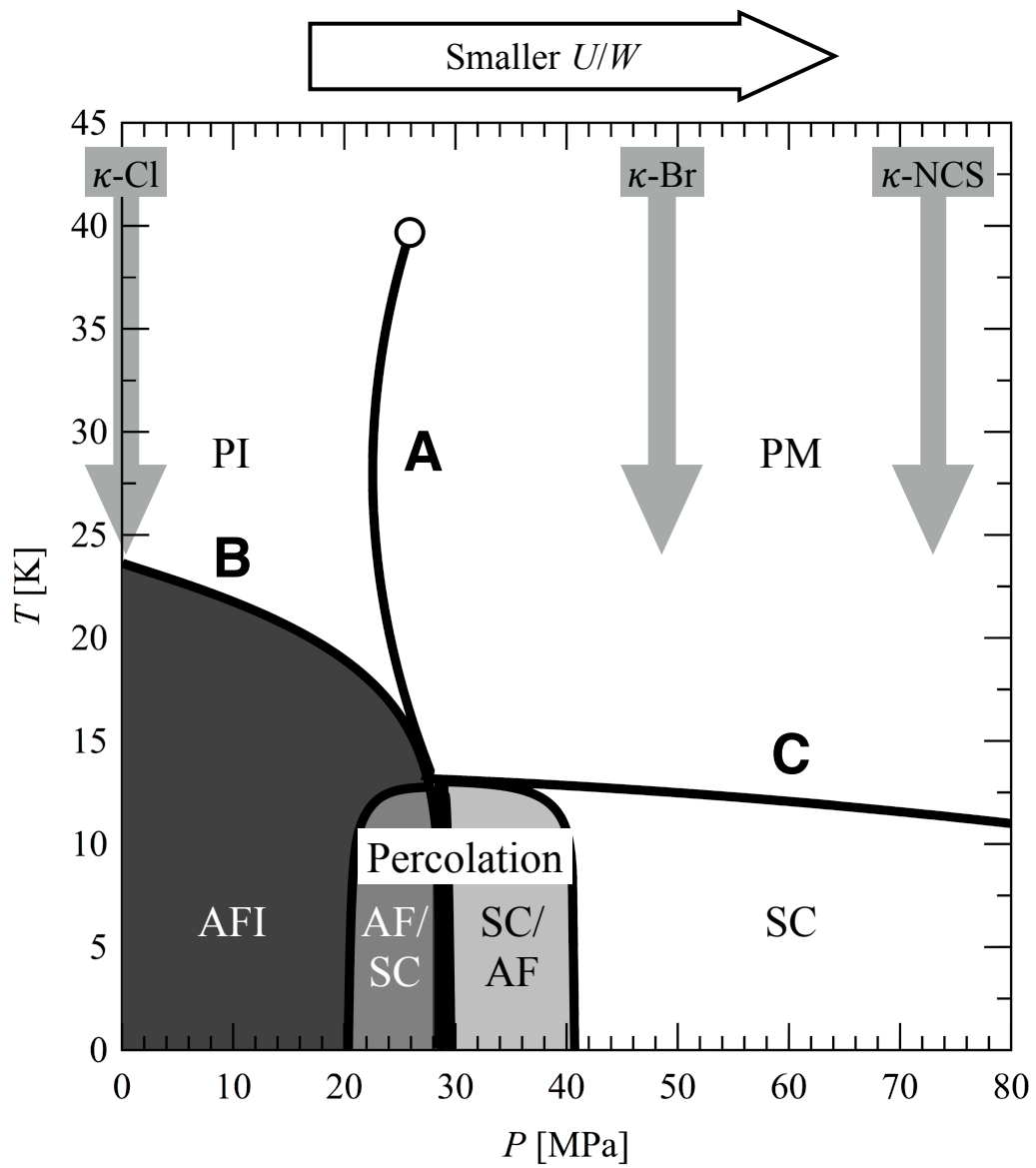


Figure 1.1.4: Schematic phase diagram of  $\kappa$ -(BEDT-TTF) $_2$ X.

## 1.2 Mott Transition

As mentioned above, in the system which well described by Hubbard model, Mott transition can be observed where  $U/W = 1$ . However, when the system undergoes to insulating (localised) state, the exchange interaction between each spin of the carriers became appreciable and spins often form ferromagnetically ordered state. Consequently, such metal-insulator transition with magnetic ordering cannot be treated as a Mott transition since symmetries of two states between phase transition are no longer the same. Actually, it is hard to find material that shows “genuine” Mott transition without any change of symmetry. By lack of candidates, the critical behaviour of Mott transition has remained unclear despite its importance.

The first example of bandwidth-controlled Mott transition without magnetic ordering is  $(V_xCr_{1-x})_2O_3$  system that perform Mott transition by lowering temperature, applying pressure or inducing vanadium [11]. In 2003, Limelette *et al.* reported [12] three critical exponents of Mott transition of this system from electrical conductivity measurements. In their report, critical exponents  $(\delta, \beta, \gamma)$  are estimated as  $(3, 0.5, 1)$  in wide temperature and pressure range which coincides with the theoretical prediction of a classical system [13], which was predicted by Castellani *et al* [14]. However, at the vicinity of the critical endpoint, they estimated critical exponents as  $(\delta, \beta, \gamma) = (5, 0.34, 1)$  which coincide prediction [15] from 3D-Ising model. These results suggest that critical exponents in this system are strongly reflecting three-dimensional nature of this material.

On the other hand,  $\kappa$ -Cl shows strong two-dimensionality due to its crystal structure, which may suggest different critical exponents compared to  $(V_xCr_{1-x})_2O_3$  system. In 2005, Kagawa *et al.* reported [16] critical exponents in  $\kappa$ -Cl by means of electrical resistivity. They reported that electrical resistivity of  $\kappa$ -Cl also shows scalable behaviour, but with different exponents as  $(\delta, \beta, \gamma) = (2, 1, 1)$ . Such critical exponents do not belong to any of reported experimental results or theoretical predictions. Around the same time, Imada proposed [17] a regime of quantum-Mott transition which realised when Ginzburg-Landau-Wilson scheme is going to breakdown because of dominant quantum effect, which achieved when critical endpoint approaches zero. In such case, the dimensionality of system  $d$  plays an important role and critical exponents became depends on  $d$  as  $\delta = 4/d, \beta = d/2,$

and  $\gamma = 2 - d/2$ , which well reproduce experimental results [16] with  $d = 2$ .

However, one can argue about these experimental results of  $\kappa$ -CI because of the fact that their investigation is based on the transport property that may not reflect bulk property of the sample. Especially in the investigation by means of electrical conductivity such as in literature [12, 16], conductivity is assumed to reflect only doublon density, which may questionable. From this point, to uncover its true critical exponent, an investigation from thermodynamic quantity is needed.

### 1.3 Antiferromagnetic Transition

Another aspect of  $\kappa$ -Cl will appear in much lower temperature region. In 1995, Miyagawa *et al.* reported [18] that  $\kappa$ -Cl shows antiferromagnetic ordering at around 27 K from  $^1\text{H-NMR}$  and magnetisation measurements. Several groups reported that magnetic ordering comes along with weak ferromagnetism due to the canting of ordered spin [18, 19]. After that report, Smith *et al.* found [20] that weak ferromagnetism originates to Dzyaloshinsky-Moriya (DM) interaction which strongly depends on applied magnetic field.

However, Kagawa *et al.* argued [21] that system starts to have staggered component in its paramagnetic state when external magnetic field is applied. Their scenario also states that antiferromagnetic transition becomes a crossover without thermodynamic singularity under the finite magnetic field. This change reported to be caused by the interplay between DM and Zeeman interaction. In addition to that, they measured spontaneous magnetisation under zero-field condition after field cooling [21]. From this result, they suggested that “true” transition occurs at approximately 23 K under zero-field condition. In addition to this puzzling situation, quite recently, Lunkenheimer *et al.* found [22] that  $\kappa$ -Cl shows ferroelectric behaviour below 27 K, which coincides with onset temperature of crossover. From another viewpoint, Antal *et al.* reported [23] result of ESR measurement in antiferromagnetic phase which implies that exchange interaction between in-plane spin is almost  $10^{-6}$  times smaller than that between intra-plane spin, which is comparable of 1 mT of the dipolar field. This fact makes  $\kappa$ -Cl system be treated as almost pure-2D Heisenberg-spin system with  $S = 1/2$ . This statement raises one open question that long-range ordering may not be even achievable at finite temperature by the result of Mermin-Wagner theorem [24].

As pointed out [20, 21], this peculiar situation of magnetic ordering is partly due to DM interaction which reflects the symmetry of the system. In such situation, one should consider that, in these researches described above (refs. 18–21, 23), all experiments were conducted under the finite external magnetic field. This external field can be problematic due to the fact that such magnetic field is going to break spatial-continuous symmetry. It should be noted that, in specific heat measurements under zero field, there is no anomaly that can be related to magnetic ordering [25, 26].

From this situation, Muon Spin Relaxation/Rotation ( $\mu$ SR) measurement under zero-field environment seems the only way to solve this puzzling situation because of its high-sensitivity against the magnetic ordering. In addition to such advantage,  $\mu$ SR method allows us to determine one of the critical exponents,  $\beta$ , in terms of the temperature dependence of precession frequency, which is proportional to the internal field at a position of muon. Such information on  $\kappa$ -Cl was not reported so far, which give us a clue to classify the magnetic ordering of  $\kappa$ -(ET)<sub>2</sub>X system.

Such discussions also applies to another antiferromagnet, d8- $\kappa$ -Br, which has same crystal structure as  $\kappa$ -Cl. This system believed to be placed at nearby AFI-SC boundary in the schematic phase diagram [27]. This assumption is supported by the fact that d8- $\kappa$ -Br has a major fraction of AFI phase and a minor fraction of SC phase [27, 28], as same as in the case of  $\kappa$ -Cl under 20 to 28 MPa of pressure. In literature, tiny SC phase is observed [27, 29–33], in d8- $\kappa$ -Br. In the magnetisation measurement, a weak-ferromagnetic component is observed [27], which relates to DM interaction as same as in the case of  $\kappa$ -Cl. From such point, as same as in the case of  $\kappa$ -Cl [21], the field-induced crossover may take place at  $T > T_N$ , which requires zero-field  $\mu$ SR investigation. In addition to that, there is another important aspect of d8- $\kappa$ -Br. Due to its position on the schematic phase diagram, d8- $\kappa$ -Br enables us to investigate how magnetic ordering behaves towards Mott transition. As mentioned in section 1.2, exotic critical behaviour of Mott transition is reported in experimental [16] and theoretical [17] studies. If such behaviour is a characteristic nearby Mott transition, we may detect some peculiar behaviour of magnetic ordering towards Mott transition.

## 1.4 Superconducting fluctuation

In general, the wave function of Cooper pair in the superconducting state was described by two important parameters, amplitude and phase. These two quantities can fluctuate by thermal or quantum effects in a specific situation. When these fluctuations become appreciable without forming a bulk superconducting ordering, one may observe a precursor-like behaviour of superconductivity, superconducting fluctuation (SCF). Actually, in conventional superconductors, observation of these phenomena by magnetic susceptibility was already reported on the layered and intercalated system by Prober *et al.* [34]. They claimed that results of intercalated superconductor could be understandable by the idea of amplitude fluctuation due to classical thermal effect. In addition to that, due to the stroboscopic appearance of vortices, anomalous enhancement of Nernst coefficient in the SCF state was predicted and observed [35]. On the other hand, in the high- $T_c$  superconductors, quite fascinating behaviour that called pseudo-gap state can be found in the under-to-optimal doped region of them [36]. Recently, Xu *et al.* reported [37] anomalous enhancement of Nernst coefficient on high- $T_c$  cuprates which can be originated to emerge of SCF. To understand this result, Kontani suggested [38] that a Nernst signal observed below the pseudo-gap temperature in such cuprates can be explained by the reflection of the enhancement of  $d$ -wave SCFs and anti-ferromagnetic fluctuations, without assuming thermally excited vortices. Another interpretation is explained by Ussishkin *et al.* [39], which states that Gaussian amplitude fluctuations are sufficient to explain the Nernst effect in optimally doped and overdoped cuprates. Also, it is worth noting that, phase fluctuation was theoretically predicted to play an important role in their superconductivity in high- $T_c$  cuprates and organic superconductors, which was supported [40] by the theoretical study. One of the fascinating interpretations for this enhancement includes the scenario in which Cooper pairs formed at temperatures higher than  $T_c$  are subjected to the incoherent state, owing to above-discussed strong phase fluctuations. From this viewpoint, investigation on organic superconductor that is a more-simplified bandwidth-controlled superconductor is needed.

In 2007, Nam *et al.* reported [41] anomalous enhancement of Nernst coefficient just above superconducting transition temperature  $T_c$  on  $\kappa$ -Br. In this material,  $T_c$

was reported around 10 K in the literature [42], but anomalous enhancement starts around 19 K, which seems to suggest an origin of such anomaly is not the bulk coherence of SC wave function. The interesting fact is that another superconductor from  $\kappa$ -(ET)<sub>2</sub>X system,  $\kappa$ -NCS, does not show [41] such enhancement of Nernst coefficient down to  $T_c$ . They claimed [41] that existence of Mott transition is playing an important role in the appearance of SCF because of that only  $\kappa$ -Br shows SCF, which sits nearby AFI-SC transition on the schematic phase diagram. On the other hand, Tsuchiya *et al.* claimed that they observed [43,44] SCF behaviour not only at  $\kappa$ -Br but also at  $\kappa$ -NCS from a magnetic torque measurement by detecting tiny diamagnetic component. They argued that this inconsistency is originated to that strong in-plane magnetic field can help emerge of SCF which is inevitable for magnetic torque measurements. In addition to that, reported onset temperature of SCF from magnetic torque is around 15 K [44] in  $\kappa$ -Br, which also shows inconsistency between reports based on Nernst coefficient [41].

Recently, the onset temperature of SCF from Nernst coefficient measurement is reported [45] in  $\kappa$ -(BEDT-TTF)<sub>2</sub>Cu[N(CN)<sub>2</sub>]Cl<sub>1-x</sub>Br<sub>x</sub> system. They reported that onset temperature of SCF is enhanced when the value of  $x$  is decreased. In the most substituted superconductor, which with  $x = 0.73$ , which claimed to be equivalent of  $29.7 \pm 0.4$  MPa of pressure in  $\kappa$ -Cl, the onset temperature is enhanced to  $55 \pm 5$  K which is almost six times larger than that of superconducting transition. They suggest that SCF phase shows a trend to grow towards Mott transition, which also needed to be investigated by bulk measurements. From these reported results, there is still an open question about the origin of SCF and estimation of the characteristic temperature of SCF. To solve this puzzling situation, highly sensitive SCF probe is needed.

## 2 Experiments

### 2.1 Magnetisation Measurement

In this dissertation, magnetisation measurements were performed to investigate criticality of SCF and that of Mott transition. Throughout this dissertation, all of the magnetisation measurements were performed using a SQUID magnetometer (Quantum Design MPMS). They detect inductive voltage from four-turned pickup coil by using inductive coupled SQUID that enables detecting small signal down to the equivalent of  $10^{-7}$  emu of magnetisation. Reciprocal Sample Operation (RSO) technique is adapted to measurements under ambient pressure to increase precision and accuracy. This instrument also enables us to perform magnetisation measurement under magnetic field up to 70 kOe with the temperature down to around 2 K. This field and temperature ranges are enough to reach transitions such as superconducting, antiferromagnetic and Mott one in  $\kappa$ -Cl.

In the investigation of SCF, it is required to control the direction of magnetic field to perpendicular and parallel direction to conducting plane. To achieve such situation, we fabricated cubic-shaped sample holder with Kapton<sup>R</sup> film (see figure 2.1.2). Its diagonal length is matched to the diameter of the sample-introduce tube to hold the holder itself. This device enables us to change the sample direction against a magnetic field without detaching the sample from the holder. With the help of such technical improvement, we were able to detect a tiny amount of diamagnetic component that originates to SCF.

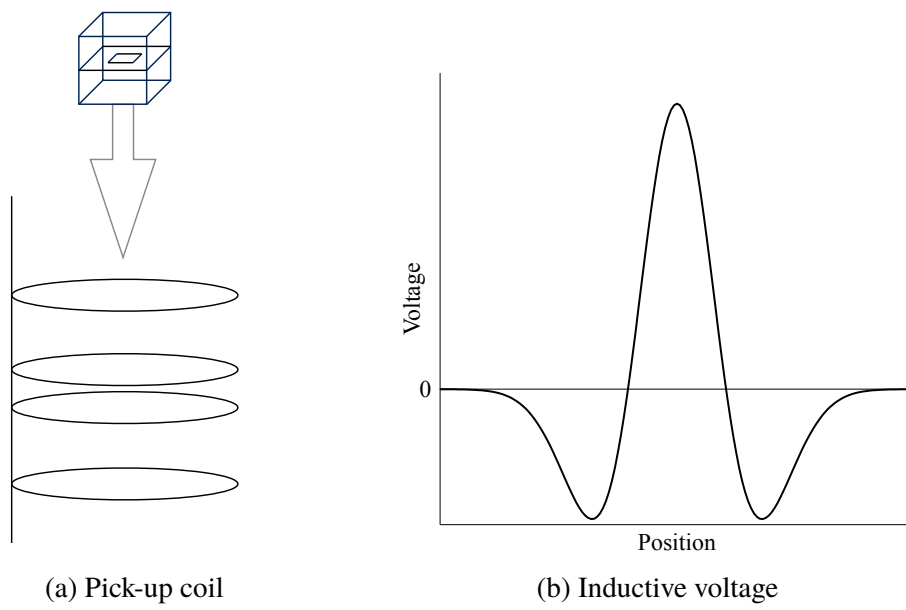


Figure 2.1.1: Schematic display of SQUID magnetometer.

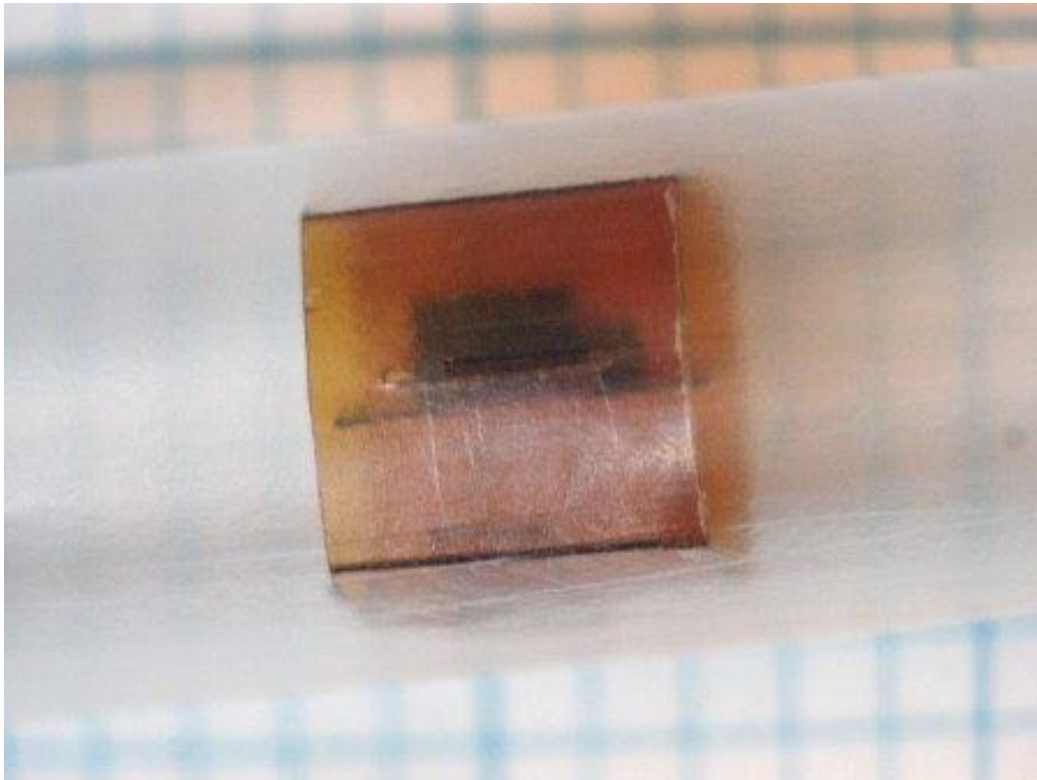


Figure 2.1.2: Fabricated cubic-shaped sample holder at inside of sample introduction tube.

## 2.2 Helium-gas Pressurise Technique

Pressure is one of the ways to control electronic correlation, especially in organic materials. To generate and hold high pressure, clamp-type pressure cell is commonly adopted with oil pressure medium. This technique can reach few GPa of pressure, and also it is easy to combine with experimental instruments such as cryostat or external magnet. However, this technique requires re-clamping to change the pressure inside the cell, which may take a significant amount of time especially in the case of low-temperature experiment. From this point, at RIKEN-RAL in UK, He gas pressurise system is installed for  $\mu$ SR experiments [46]. This device enables us to perform pressure-sweeping measurement without warming up or removal of the pressure cell from the instrument. Also, concomitantly, He gas provides good hydrostatic pressure due to its smaller particle size.

Reflecting such situation, we adopt such pressure-handling system into SQUID magnetometer. Figure 2.2.1 shows drawing of SQUID magnetometer with the pressure-handling system. Helium gas was supplied from a cylinder which filled up to 30 MPa of pressure and He-gas line goes through a pressure generate system which is composed of a compressor and a cylindrical intensifier. Cylindrical intensifier also provides roll as He-gas buffer to prevent a subtle change of pressure inside of the pressure cell. To seal medium firmly, modified Bridgman seal method is adopted. This technique enables our pressure cell to keep He gas inside up to 500 MPa of pressure. In this dissertation, pressure is controlled between ambient pressure to 120 MPa. Due to the mechanical structure of the instrument, it is inevitable to detect the contribution from pressure cell. To solve this issue, we used pencil-shaped pressure cell made out of CuBe that shows almost non-magnetic behaviour in this temperature/pressure region.

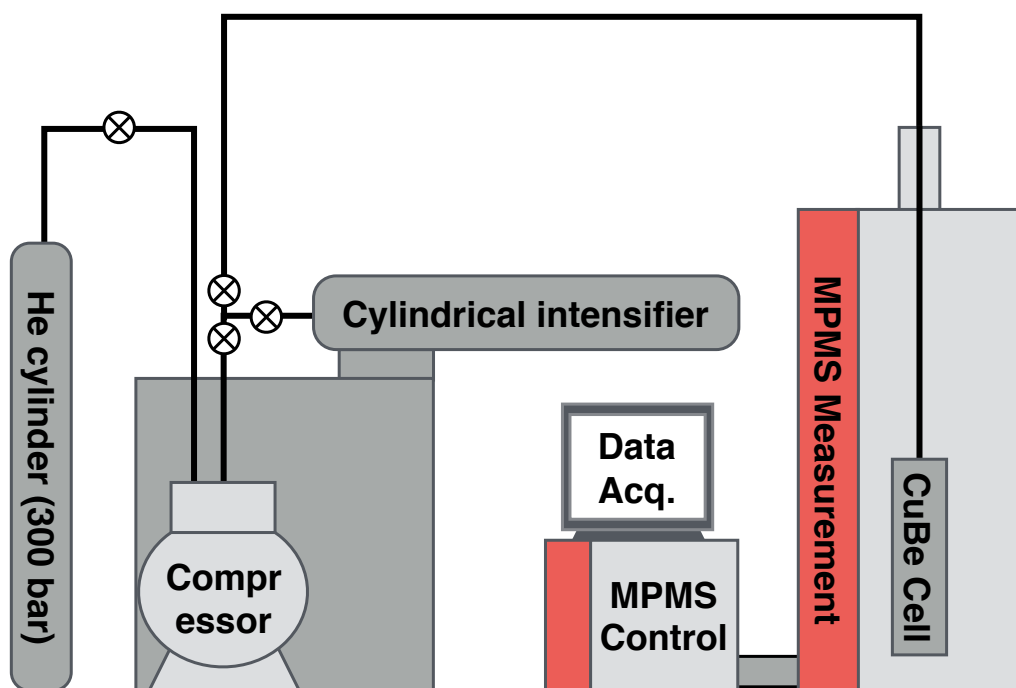


Figure 2.2.1: Schematic of SQUID magnetometer with pressure-handling system.

### 2.3 Muon Spin Relaxation/Rotation Measurement

Usually, the magnetic properties of material are observed as a response to the external magnetic field that can be problematic due to its magnetic field-dependent nature of AFI phase in  $\kappa$ -Cl [21]. A way to avoid this issue is to adopt another magnetism probe that works properly under zero-field condition,  $\mu$ SR [47, 48].

$\mu$ SR method uses the  $\mu^+$  as a probe to magnetism inside of the material. In actual experimental situation,  $\mu^+$  particles are provided by accelerator source to ensure the high intensity. Accelerated proton ( $p$ ) beams are fired to graphite target to produce positive pions ( $\pi^+$ ) by such reaction



where  $n$  represents neutron. After that,  $\pi^+$  subsequently decay with its life-time of 26 ns as



where  $\nu_\mu$  represents mu neutrino. The reaction described by equation (2.2) is a two-body reaction, which can be described in a simple picture. From pion rest frame, muon and mu-neutrino should have the equal amount and opposite direction of momentum to obey the momentum-conserve law. Addition to that, mu neutrino has negative helicity that means its spin is aligned antiparallel to its momentum. These restrictions makes muon to align its spin in same negative helicity manner as  $\nu_\mu$ . Such situation can be displayed in simple schematic such as fig. 2.3.1. Thus,

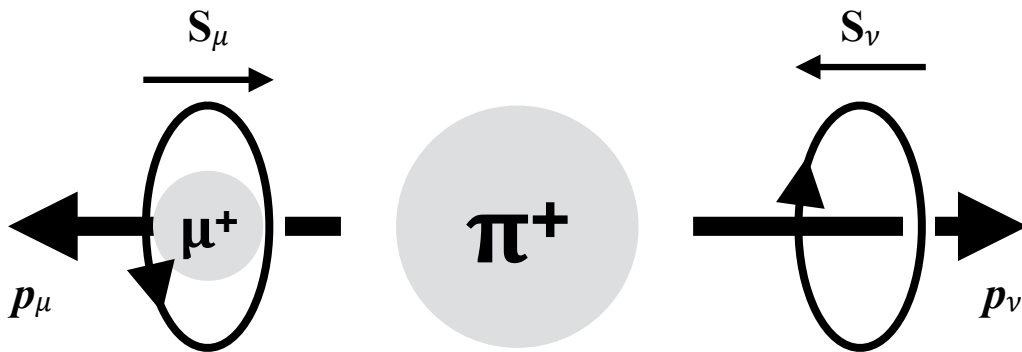


Figure 2.3.1: Schematic of  $\pi^+$  decay in pion rest frame.

by only use pion that stopped on the surface of the target, one can get a beam of 100% spin-polarised “surface muon”. These produced muons will be transported to inside sample by several magnets. When muons are delivered to sample, muons are stopped at preferable position that determined by static potential of the sample. After muons are delivered and stopped at muon site, muons start to decay with a probability proportional to  $e^{-t/\tau_\mu}$ , where  $\tau_\mu = 2.2 \mu\text{s}$  is the lifetime of the muon. Its decay can be written as (2.3) with electron neutrino ( $\nu_e$ ) and anti-mu neutrino ( $\bar{\nu}_\mu$ ), which is three-body process thus momentum of positron ( $e^+$ ) will show very broad distribution.

$$\mu^+ \rightarrow e^+ + \nu_e + \bar{\nu}_\mu \quad (2.3)$$

This decay process came with an important fact that enables us to prove magnetism of sample. Product positrons are emitted with certain angular distribution which described as (2.4) where  $\epsilon$  is the energy which normalised by the maximum energy of positron and  $A(\epsilon) = (2\epsilon - 1)/(3 - 2\epsilon)$  is an asymmetry factor.

$$W(\theta) = 1 + A(\epsilon) \cos \theta \quad (2.4)$$

As shown in in eq. 2.4, angular distribution of emitted positron strongly depends on its energy. This fact enables us to detect the spin direction of stopped muon if we detect spatial distribution of emitted positron with a number of events enough to cover its energy distribution. To detect spatial distribution, in most simple case, two detectors are placed at muon beam’s forward (**F**) and backwards (**B**) direction like figure 2.3.2.

Here, to obtain the information about the motion of muon, new physical amount, asymmetry is introduced. It is defined as normalised counts difference between forward and backwards counter, such as equation 2.5 with counts of backwards counter,  $N_B$  and forward counter,  $N_F$ .

$$A(t) = \frac{N_B - N_F}{N_B + N_F} \quad (2.5)$$

If we assume every each muon feels same intensity of the internal magnetic field, the time evolution of counts in both detectors can be calculated as figure 2.3.3a. At very first, the spin of muons should point to backwards counter due

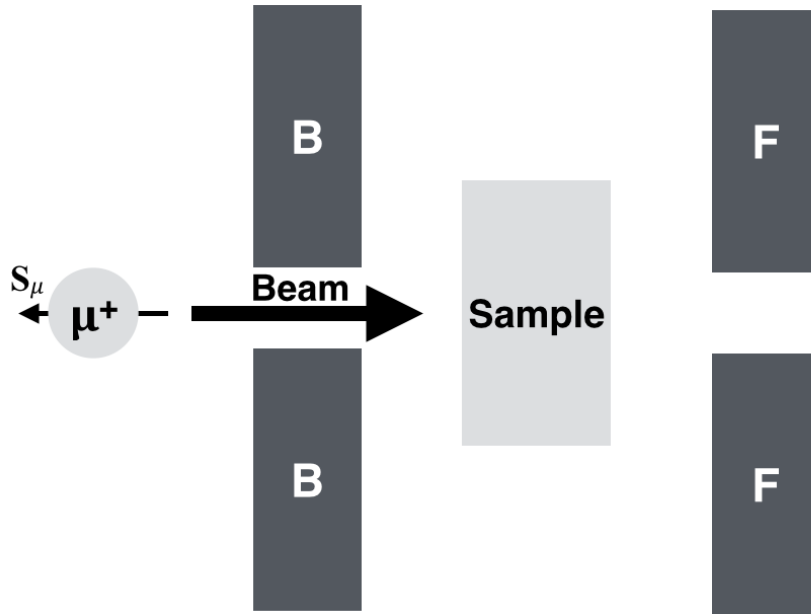


Figure 2.3.2: An example of detector configuration.

to its origin, then counts of the backwards counter should be higher compared to forward counter. Then, the spins of muons start precession motion that caused by the internal magnetic field. In such case, asymmetry  $A(t)$  shows behaviour illustrated in figure 2.3.3b. This assumption corresponds to a situation such as uniform internal field over the sample, or magnetically ordered sample with a completely fixed muon position. In actual samples, slight inhomogeneity or motion of muon will cause a distribution of internal field. When we consider the effect of distribution, precession signal with envelope can be observed (see figure 2.3.4). In such case, these signals contain information such as the norm of internal field, and breadth of the field distribution. This behaviour frequently observed in magnetically ordered samples. Envelope-relaxation component came from the slight difference of each muon such as small spatial discrepancy. In such

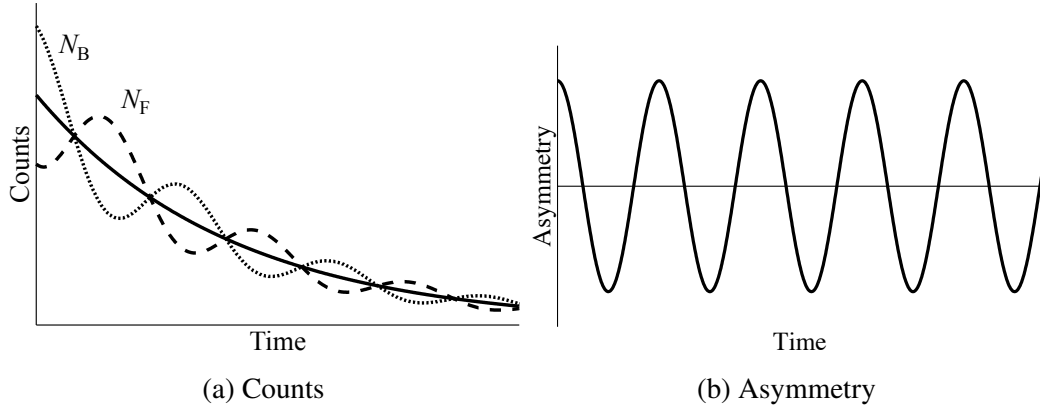


Figure 2.3.3: Counts and asymmetry for simplified scenario. See text for details.

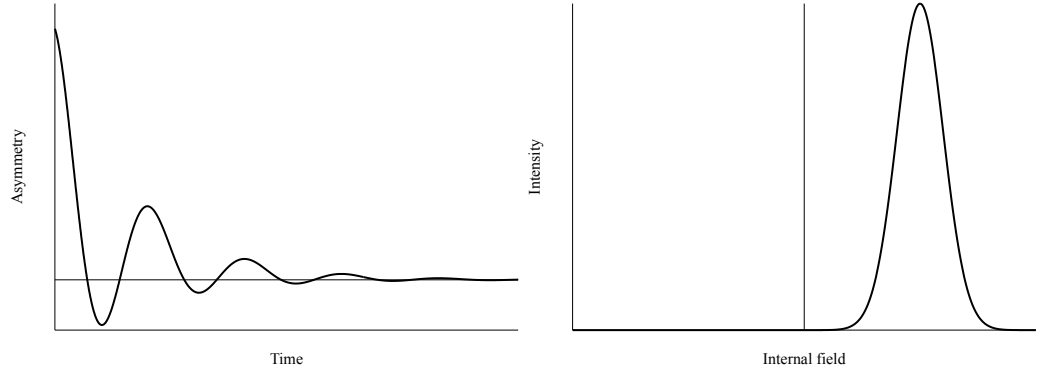


Figure 2.3.4: Left:Rotation signal with decaying envelope. Right:Distribution of internal field with center at finite value.

case, asymmetry spectrum from  $N$ -site muon can be fitted with function as

$$A(t) = A_0 \sum_{i=1}^N p_i \cos(\gamma_\mu B_i t + \phi) \exp(-\lambda_i t) \quad (2.6)$$

with the gyromagnetic ratio of  $\mu^+$ ,  $\gamma_\mu$  (see also figure 2.3.4). In such formulation, phase  $\phi$  corresponds to a slight incline of delivered muon,  $B_i$  corresponds to a norm of the internal field at muon site which labelled  $i$ , and the time constant of Lorentzian-like envelope  $\lambda_i$  gives us information about field distribution at site  $i$ . If the norm of the internal field at that site has a wider distribution, time constant  $\lambda$  should have a larger value.

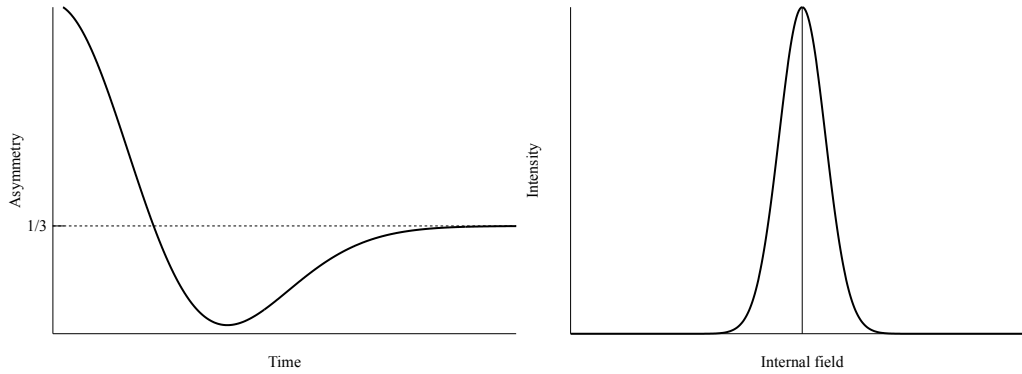


Figure 2.3.5: Left:Kubo-Toyabe function. Right:Gaussian distribution of internal field sits on zero field.

Otherwise, in paramagnetic phase, it is assumed that each muon respond to magnetic field originated from dipole moment of each nucleus, which seems static to muon due to its time window. In such case, muon detects Gaussian distribution of magnetic field that has centre at zero. With such distribution, so-called Kubo-Toyabe function is obtained (see equation 2.7 and figure 2.3.5).

$$G_{\text{KT}}(\Delta, t) = \frac{1}{3} + \frac{2}{3}[1 - \Delta^2 t^2] \exp[-\frac{1}{2}\Delta^2 t^2] \quad (2.7)$$

This function characterised by convex behaviour nearby  $t = 0$  and one-third of constant component. In other word, two-thirds of muons shows rotational behaviour due to Gaussian distribution at muon site and another one-third of muons shows no relaxation because of that spin direction of  $\mu^+$  is aligned to the nuclear-dipole field. In such situation, if we put disorder on muon or dipole, profile of asymmetry can be changed by broadning of internal field distribution (such effect will be discussed in Appendix).

However, there is another important factor about  $\mu\text{SR}$  experiment that is the time structure of muon beam. As mentioned above, to ensure intensity of muon, we use accelerator as a muon source. Time structure of beam was decided by the mechanism of the accelerator. In the case of a synchrotron, there is a part of accelerating process called bunching which forms two bunches of accelerated particles. With that effect, two bunches of muons with finite peak width were delivered to the sample. For example, the beam from ISIS synchrotron at Rutherford-Appleton

Laboratory (RAL) provides two pulses with a width of 80 ns and separation of 340 ns. These pulses were assumed to have the same time of arrival for each pulse because of it is difficult to distinguish every muon in a single pulse. On the other hand, in the case of a cyclotron, there is no process such as bunching and beam has continuous-wave time structure. Reflecting such situation, there is no assumption on muon's time of arrival. A problem about cyclotron is that, when a muon is stopped and starts motioning inside the sample, the next muon can arrived at sample. In such case, both two events should be discarded because of that one cannot distinguish which positron signal belongs to which muon. In addition to that, in the case of continuous-wave structure, it is inevitable to detect noise from particles other than  $\mu^+$ . With these issues, it is quite difficult to observe long-lived muon events within reliable statistical error. These situations can be summarised as follows.

- Synchrotron (Pulsed structure)
  - PROS: Can observe long-lived events
  - PROS: Low noise level
  - CONS: Assumed time of arrival causes time uncertainty.
  - Provided at: Rutherford-Appleton Lab.(UK), J-PARC(Japan)
- Cyclotron (Continuous-wave structure)
  - PROS: Precise time of arrival
  - CONS: Considerable level of noise due to another particle
  - CONS: Difficult to observe long-live muons
  - Provided at: Paul Scheller Institut(Switzerland), TRIUMF(Canada)

Under consideration on such characteristics, in this research, pulsed muon beam is used to investigate information such as internal field, especially nearby ordering temperature due to expected smaller internal field. Contrary, continuous-wave beam is used to investigate ordered phase at lower temperatures.

## 3 Results for Mott transition

### 3.1 Measurement under ambient pressure

Before investigating Mott transition by using SQUID magnetometer with pressurising device, it is needed to estimate the contribution from pressure cell. Figure 3.1.1 shows temperature dependence of spin susceptibility of  $\kappa$ -Cl under 10 kOe of magnetic field. Closed symbols represent the result obtained without pressure cell and open symbols represents that obtained with pressure cell. Two data sets almost coincide in this temperature region, which suggests the contribution from pressure cell is almost neglectable. Nevertheless, as shown in the inset of fig. 3.1.1, two data sets show small discrepancy in low-temperature region. However, such discrepancy does not affect the estimation of the onset temperature of SCF which will be discussed later.

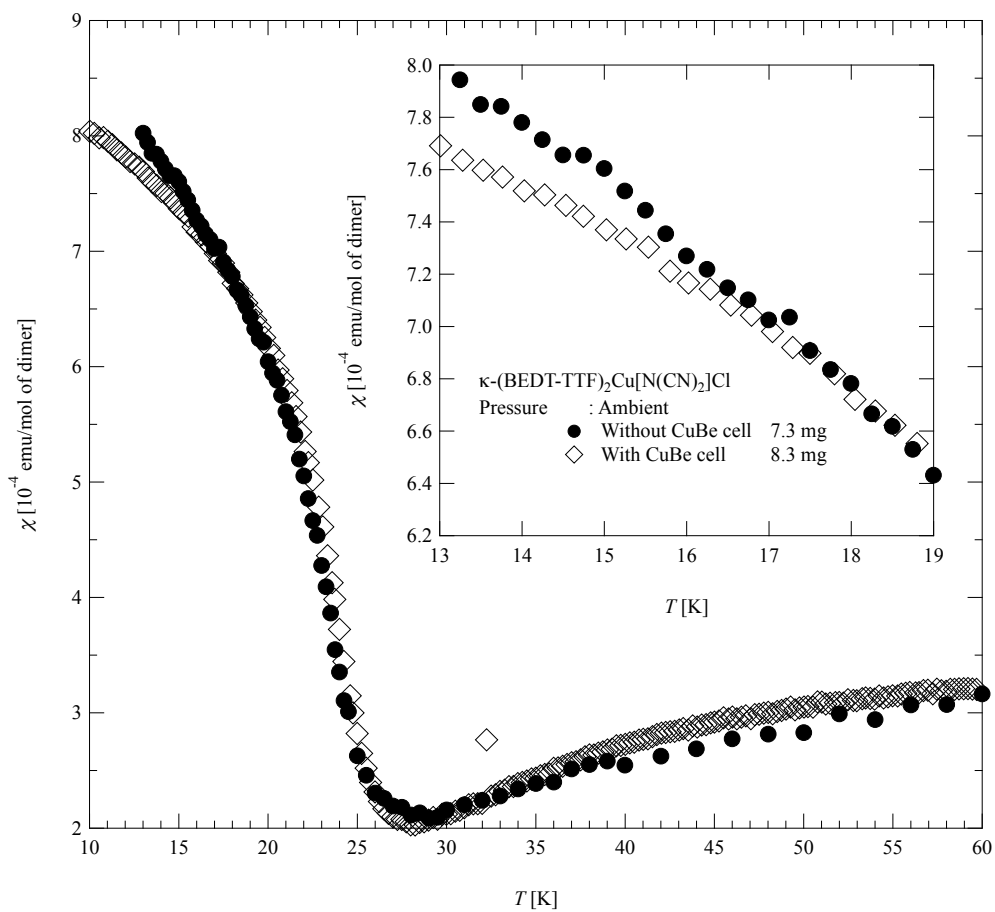


Figure 3.1.1: Spin susceptibility of  $\kappa$ -(BEDT-TTF)<sub>2</sub>Cu[N(CN)<sub>2</sub>]Cl. Closed symbols represents measurement without pressure cell and open symbols corresponds to measurement with pressure cell.

### 3.2 Measurement under pressure I—Phase Diagram

To begin the discussion of critical behaviour in  $\kappa$ -(ET)<sub>2</sub>X, we need to consider the validity of proposed schematic phase diagram [9, 10]. Accordingly, we constructed the pressure-temperature diagram of  $\kappa$ -Cl by magnetisation measurements.

Figure 3.2.1 shows the temperature dependence of magnetic susceptibility under 10 kOe of the magnetic field in the lower-pressure region. Magnetic sus-

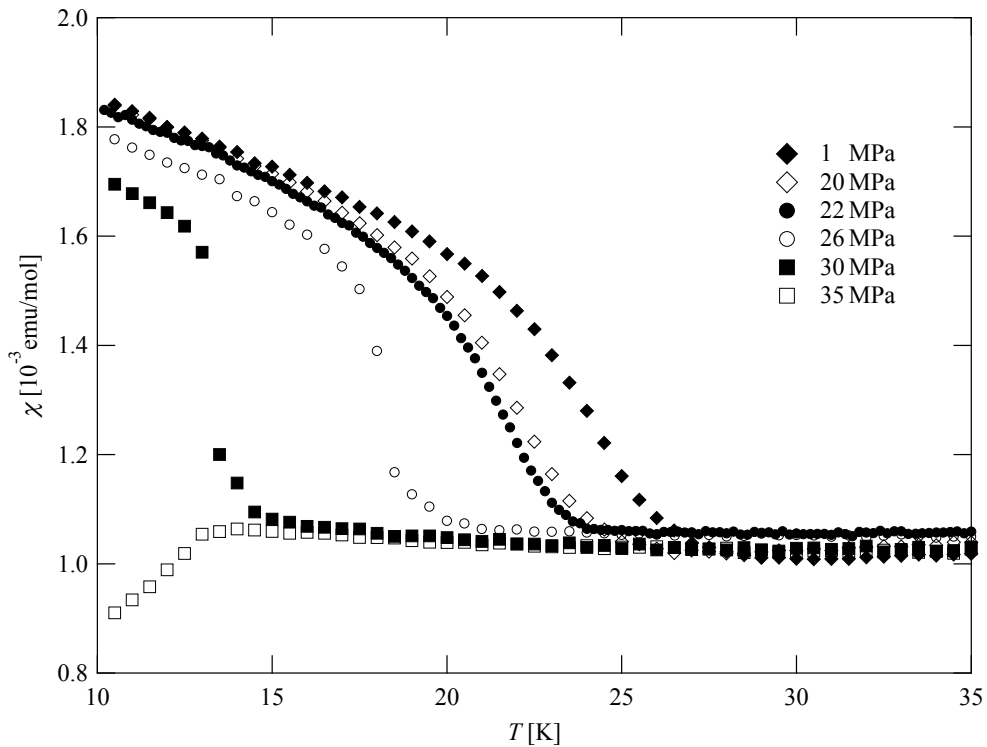


Figure 3.2.1: Spin susceptibility under 10 kOe. Values of pressure at high temperature are also shown.

ceptibilities obtained under less than 30 MPa of pressure show an increase along with cooling down, which is considered as an indication of magnetic ordering due to weak-ferromagnetic component [18, 19]. Such an increase diminishes under 35 MPa of pressure, which suggests AFI phase does not appear in this pressure region, or at least its weak-ferromagnetic component is smeared by SC component. The magnetic ordering temperature is defined by the onset of such increase. In addition to that, due to expected magnetic field dependence of ordering tempera-

ture [21], we performed the measurement in zero-field manner after field-applied cooling under 10 kOe. Figure 3.2.2 displays results of such measurements and values of magnetisation show sudden drop to negative value while system is warmed. This decreasing behaviour indicates existing of residual magnetic field from su-

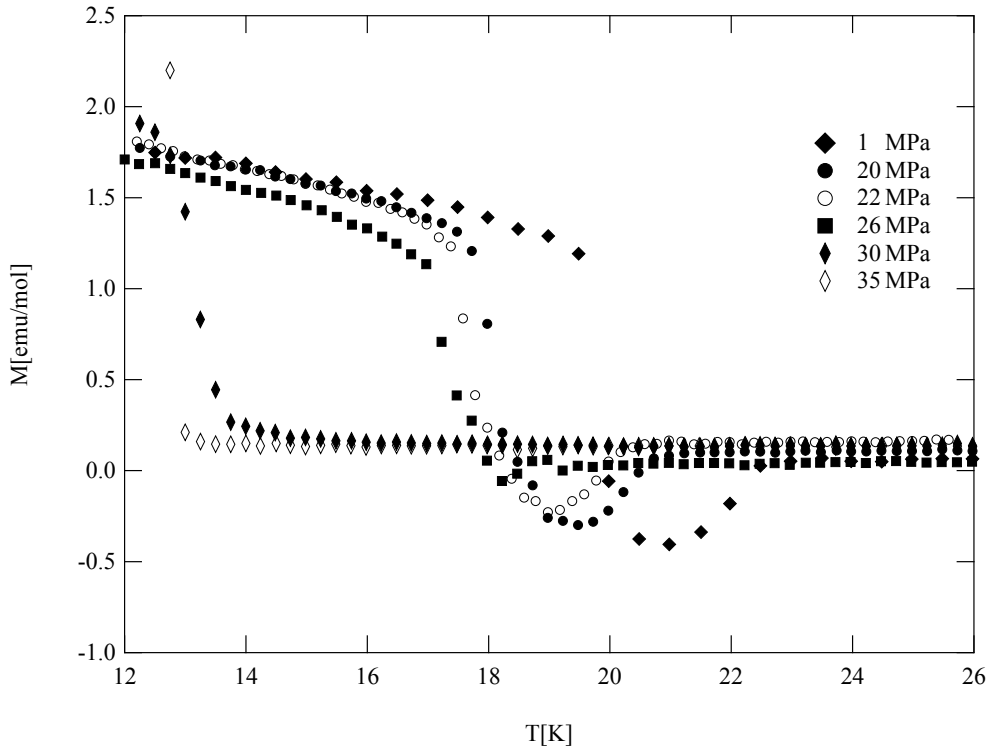


Figure 3.2.2: Magnetization under zero field after field cooling under 10 kOe.

perconducting magnet. From this point, we defined magnetic ordering point at the high-temperature end of the cusp. As shown in figures 3.2.1 and 3.2.2, these two sets of measurements clearly show different Néel temperature which supports suggested idea [21] of existence of crossover which replaces magnetic ordering.

On the other hand, to estimate SC transition temperature, magnetic susceptibilities under 5G at several pressures are measured (see figure 3.2.3 for examples). Each measurement was performed both zero-field-cooled (A in figure 3.2.3) and field-cooled manner (B). After field-cooled measurement, magnetic field was turned off at lower-temperature region to observe the release of residual magnetisation (C). SC transition temperature was defined as the point where three data

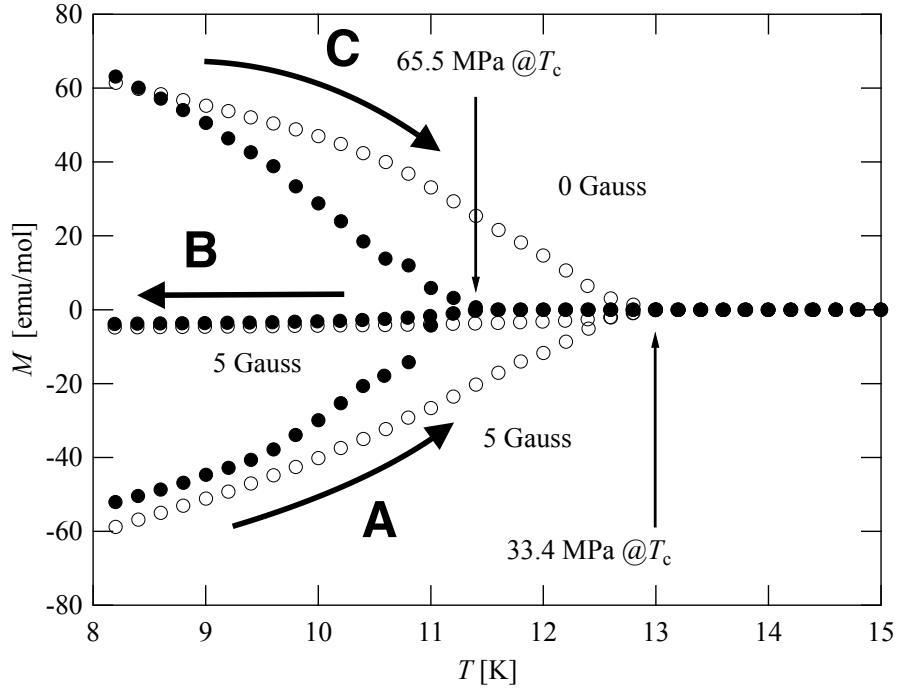


Figure 3.2.3: Magnetization under several higher pressure. (See text for details.)

sets are agreeing.

Additionally, transition points between SC and AFI are estimated by pressure sweep measurement in low temperature. Two data sets were obtained under zero-field cooled condition. Measurements are started at high pressure and system was depressurised to AFI state then pressurised to SC phase again. With this procedure, pressurising process will correspond to the field-cooled process in conventional temperature sweep measurement. These two data sets show small but finite hysteresis and the peak of differentiation coefficient are defined as transition point (see figure 3.2.4).

The position of Mott transition on phase diagram is also estimated by pressure-sweep measurements (detail will be discussed later at next subsection). These defined transition points are plotted in figure 3.2.5. This diagram characterised by i) field-dependent Néel point ii) small but distinct hysteresis between AFI and SC phase and iii) the existence of critical endpoint in Mott transition. Also, this phase diagram agreeing with proposed schematic phase diagram [9, 10] quite well.

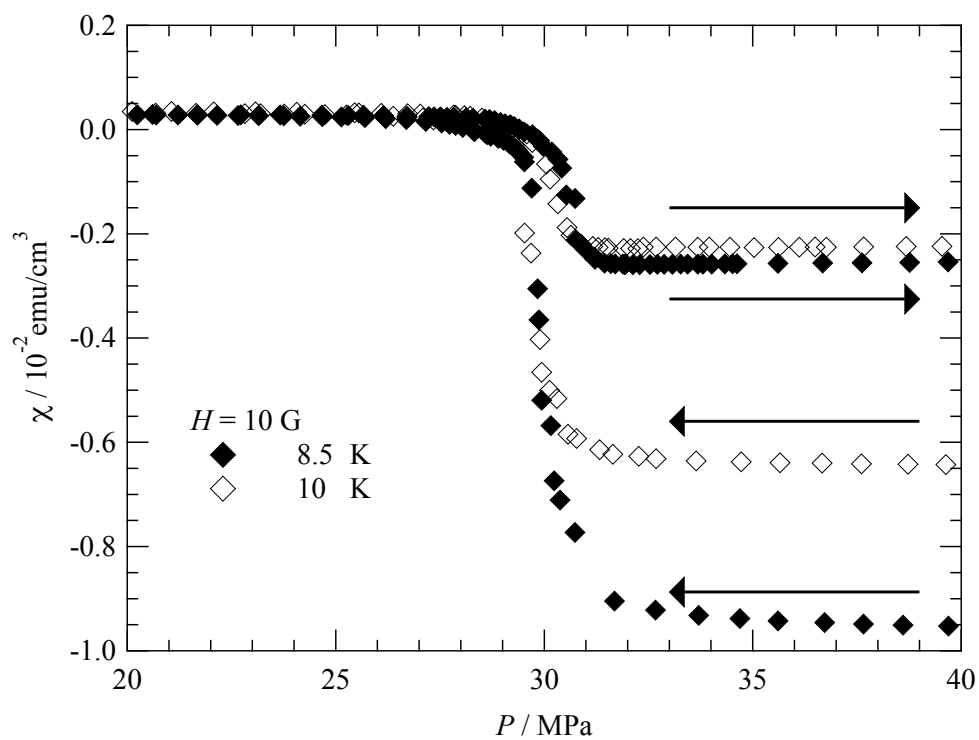


Figure 3.2.4: Pressure dependence of spin susceptibility in low temperature. Allows indicates process of pressure operation.

This fact allows us to we discuss different members of  $\kappa$ -(ET)<sub>2</sub>X family on phase diagram.

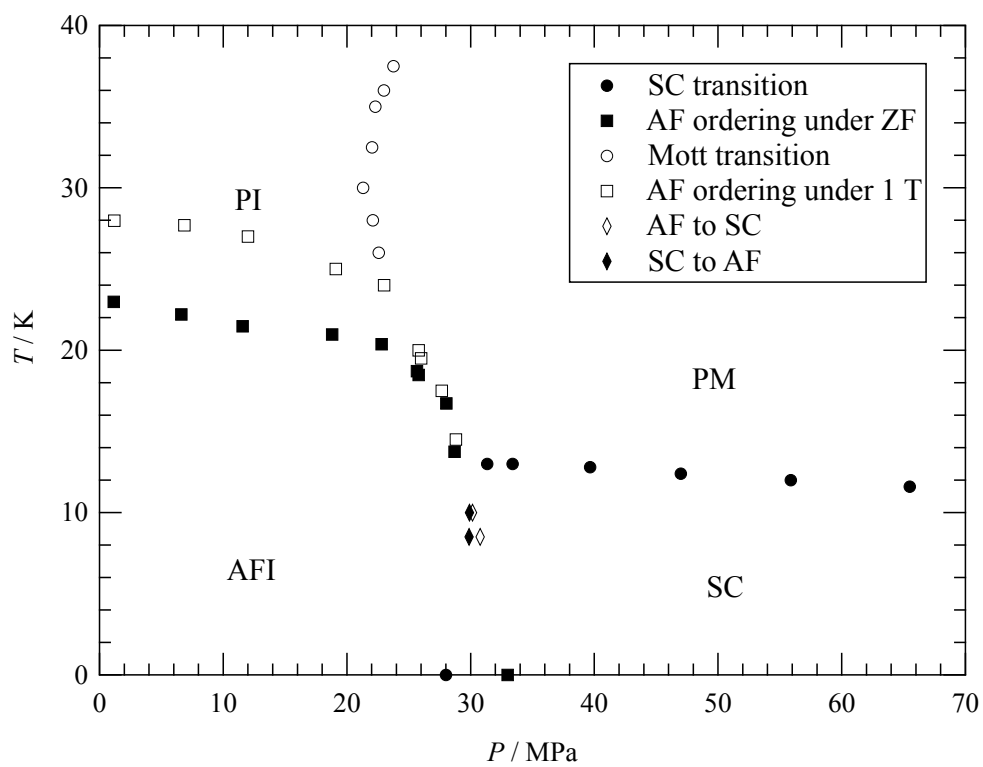


Figure 3.2.5: Phase diagram of  $\kappa$ -(BEDT-TTF)<sub>2</sub>Cu[N(CN)<sub>2</sub>]Cl which constructed by magnetisation measurements under pressure.

### 3.3 Measurement under pressure II—Criticality of Mott transition

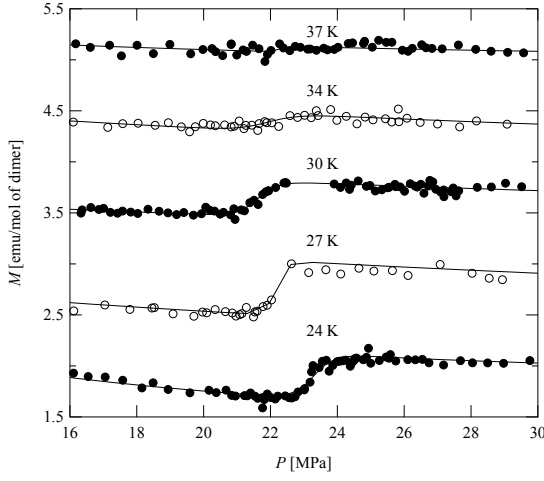
To investigate Mott transition by magnetisation measurement, pressure sweeping measurements were performed at fixed temperatures in the range of  $27 \text{ K} < T < 42 \text{ K}$ . Results at several temperatures are shown in figure 3.3.1 together with obtained phase diagram (each measurement was indicated by arrows). As shown in fig. 3.3.1a, they show discontinuous behaviour around 20 to 30 MPa, which seems to reflect the first order character of Mott transition. These jumps diminish with increasing temperature and disappear above 36 K, which is roughly consistent with the position of the critical endpoint  $(P_c, T_c) = (24.8 \text{ MPa}, 39.7 \text{ K})$  reported in the literature [16]. We cannot find the hysteresis of this jump within the present resolution of the experiment.

This abrupt jump assumed to be related to the difference of doublon density between metallic and insulating phases. In the case of Mott transition, doublon density would be considered as order parameter. Therefore, this jump on magnetisation seems to be proportional to order parameter. In this sense, we need to investigate the behaviour of this jump towards Mott transition to estimate the critical exponent,  $\beta$ . To estimate these jumps quantitatively, each data set are fitted with phenomenological function

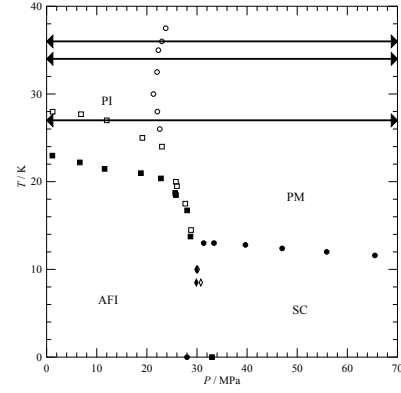
$$M(P) = M_0 + \frac{\Delta M}{1 + \exp((P_0 - P)/p)} + M_1 * \exp(-\Pi * P) \quad (3.1)$$

with fitting parameters  $M_0$ ,  $P_0$ ,  $\Delta M$ ,  $M_1$  and  $\Pi$ .  $P_0$  and  $\Delta M$  correspond to the transition pressure and the height of this jump, respectively. With this fitting, figure 3.3.2 shows the behaviour of  $\Delta M$  towards the critical endpoint. The dashed line is an eye-guide of exponent  $\beta = 1$  which is the value obtained by conductivity measurements [16]. We also performed a fitting analysis with a fitting function of  $\Delta M = M_0(|T - T_c|/T_c)^\beta$  and a best-fit parameter of  $\beta$  is  $0.96 \pm 0.16$  and that of  $T_c$  is  $39.5 \pm 0.02$ , which agree with reported values [16]. From this plot, we can conclude the critical exponent  $\beta$  of Mott transition in  $\kappa\text{-Cl}$  is 1 agree with theoretical prediction by Imada [17].

Imada's prediction suggests that, with the quantum effect which introduced



(a) Magnetization of  $\kappa$ -Cl in several temperatures.



(b) Obtained phase diagram of  $\kappa$ -Cl with arrows that indicate each measurement.

Figure 3.3.1: Results of pressure-sweep measurements at high temperature.

by path-integral formulation, free energy at  $T = 0$  can be expanded as form of equation 3.2 with  $a = a_0(g - g_c)$  nearby critical endpoint  $T_c = 0$  where  $g$  is order parameter and  $g_c$  represents the value of  $g$  at the critical endpoint.

$$F = -\mu X + aX^{\frac{d+2}{d}} + bX^{\frac{d+4}{d}} \quad (3.2)$$

If the parameter  $a$  in eq. 3.2 takes negative value, the first order transition is expected even in finite temperature. From relations such as  $\partial F/\partial X = 0$ , or  $\chi \propto |\mu|^{-\gamma}$  with  $\chi = (d^2F/dX^2)^{-1}$ , critical exponents of  $(\beta, \gamma, \delta)$  was estimated as  $\beta = 1, \gamma = 1$  and  $\delta = 2$  in the two dimensional case. In addition to that, Misawa found [49, 50] that, from numerical studies, even in finite temperature such as  $T \sim 0.01t$ , critical exponents of quantum Mott transition can emerge. They also claimed that, Ising-like exponents are unobservable in  $\kappa$ -Cl within the present resolution of the experiment.

On the basis of these theoretical predictions, we conclude that we indeed observed unique critical exponents of Mott transition in  $\kappa$ -Cl, which strongly reflects quantum effect and low-dimensionality of this system.

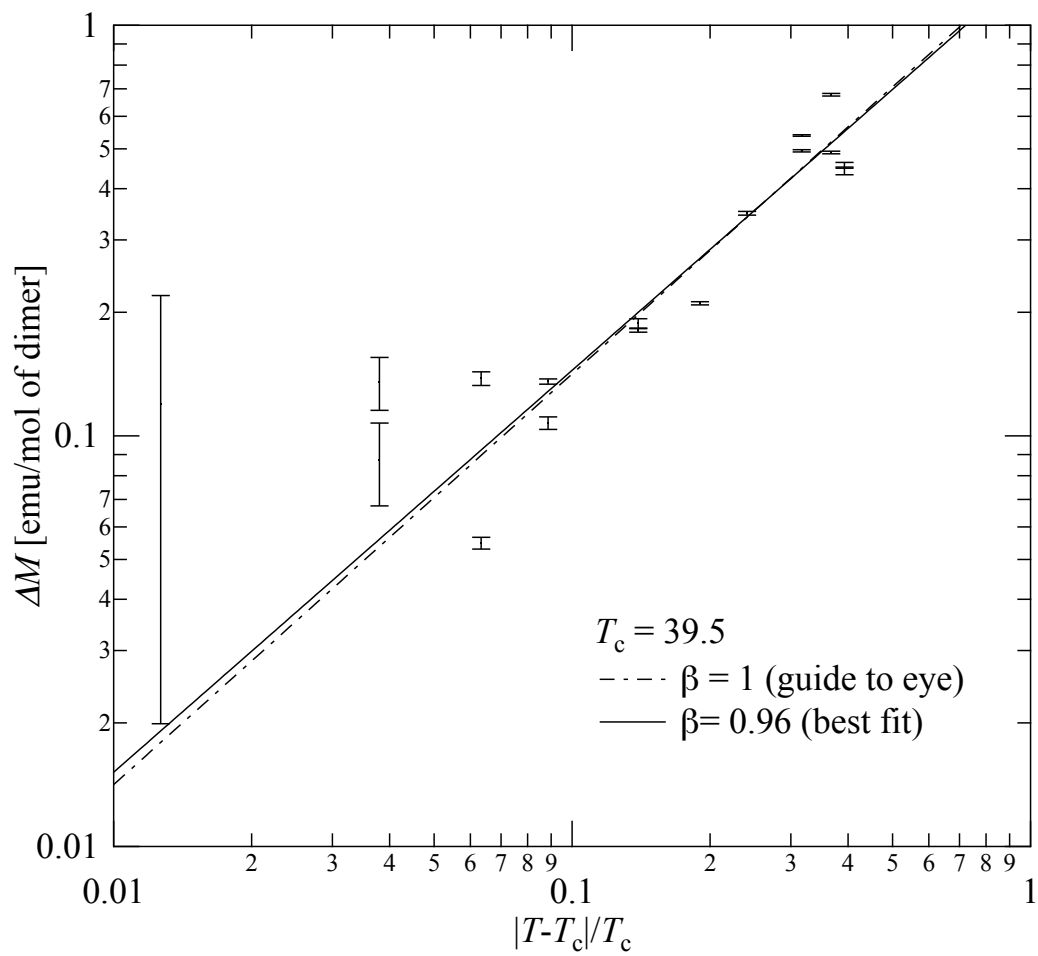


Figure 3.3.2: Temperature dependence of  $\Delta M$ . Dashed line is an eye-guide of exponent  $\beta = 1$ .

## 4 Results for Antiferromagnetic Transition

### 4.1 $\kappa$ -(BEDT-TTF)<sub>2</sub>Cu[N(CN)<sub>2</sub>]Cl

Figure 4.1.1 shows  $\mu$ SR spectra of  $\kappa$ -Cl in several temperatures. The clear precession behaviour was observed in the low-temperature region, which indicates the appearance of the magnetic ordering of electronic spins lying on BEDT-TTF dimer. In general, the magnitude of the internal field is proportional to precession frequency. Precession frequency  $\omega$  shows decreasing (i.e. slow precession) trend while the system is warmed. To investigate the detail of each spectrum, all spectra of  $\kappa$ -Cl were fitted with a function as equation 4.1.  $A_s$ ,  $A_{Ag}$ , and  $A_{const}$  represents contribution on the amplitude of asymmetry from the sample, sample holder which made by Ag foil, and the constant component which mainly from experimental condition respectively. To obtain a precise result, the value of parameter  $\sigma_{Ag}$  is fixed with known value (0.025  $\mu$ s) and values of  $A_{const}$  is also fixed with that at the lowest temperature.

$$A(t) = \begin{cases} A_s e^{-\lambda_0 t} G_{KT}(\Delta, t) + A_{Ag} e^{-(\sigma_{Ag} t)^2} + A_{const} & (T > 23.3 \text{ K}) \\ A_s [\sum_{i=1}^2 p_i e^{-\lambda_i t} \cos(\gamma_\mu B_i t + \phi) + p_3 e^{-\lambda_3 t}] + A_{Ag} e^{-(\sigma_{Ag} t)^2} + A_{const} & (T < 21.4 \text{ K}) \end{cases} \quad (4.1)$$

At 22.4 K, fitting by both functions with reasonable precision could not be achieved. From this fact, magnetic transition temperature is concluded to be in between 21.4 and 23.3 K. In the lower-temperature region, a relation between two fitted rotational frequency,  $\omega_1$  and  $\omega_2$  which converted by relation  $\omega_i = B_i/\gamma_\mu$  are plotted in figure 4.1.2a. They show linear relation in this scale and result evidences that two fitted rotational components correctly assigned to two different muon site which are observing the different intensity of internal magnetic moment from the same origin; electronic spin lying on BEDT-TTF dimer. To draw more-precise information from spectra, we fixed value as  $\omega_2 = 0.734 \omega_1$  and revisited all of the fitting. One example of revisited results is shown in figure 4.1.2b. From this fitting result, the temperature dependence of internal field  $B_{\mu 1}$  is plotted in figure 4.1.3.

From this plot, magnetic ordering seems to occur around 23 K. Unfortunately, due to the lack of data point nearby magnetic transition, we could not estimate critical exponent  $\beta$  and transition temperature  $T_N$ . However, low-temperature region ( $T < 15.6$  K) can be fitted by  $B_{\mu_1}(T) = B_{\mu_1}(0)(1 - (T/a_1)^{a_2})$  with fitting parameter  $B_{\mu_1}(0)$ ,  $a_1$  and  $a_2$  to estimate internal field at  $T = 0$  extrapolation (see dashed curve in figure 4.1.3). From this fitted result,  $B_{\mu_1}(0)$  was estimated as  $58.4 \pm 0.4$  G.

To investigate behaviour just above  $T_N$ , the spontaneous magnetisation of  $\kappa$ -Cl was investigated. Figure 4.1.4a shows isothermal magnetisation,  $M$ , as a function of magnetic field,  $H$ , parallel to the conducting layers. According to the previous report, [18] easy axis of the antiferromagnetism of  $\kappa$ -Cl is perpendicular to the layers. Also in the present data in Fig. 4.1.4a, hysteresis was clearly observed below around 20 K, while almost linear and reversible profile appeared at 25 K. From the observation of hysteresis, canting direction was found to be parallel to the layers. In order to obtain information about the spontaneous magnetism, we defined the residual magnetisation,  $M_r(T)$ , as shown in a Fig. 4.1.4b.  $M_r$  is not the spontaneous magnetisation itself but almost the same as it in this case; at lower temperature, nearly linear dependences in the reversible region lead us to have the extrapolated value almost the same as  $M_r$  (20 K in the figure 4.1.4b) and, at higher temperature, small coercive force allows us to obtain the collect value of the spontaneous magnetisation (22.5 K in the panel figure 4.1.4b). A temperature dependence of  $M_r(T)$  is shown in a Fig. 4.1.5. By fitting the data around the transition temperature with a function,  $M_r(T) = a_1(a_2 - T)^{a_3}$ ,  $T_N$  ( $\equiv a_2$ ) and one of the critical exponents,  $\beta$  ( $\equiv a_3$ ), were determined as  $22.80 \pm 0.02$  K and  $0.54 \pm 0.03$ , respectively. This value of  $T_N$  is consistent with the reported value. [21] In considering the 2D nature of the system, this  $\beta$  value larger than that of 3D Heisenberg model ( $\beta \sim 0.38$ ) is not reasonable. This may be due to the slight inhomogeneity of the sample, which could strongly affect the rapid transition like present case. An application of a fitting function of  $M_r(T) = a_4(1 - (T/a_5)^{a_6})$  to low-temperature data allow us to obtain the value of  $M_r(0)$  ( $\equiv a_4$ ) as  $0.987 \pm 0.009$   $10^{-2}$  emu/cm<sup>3</sup>. The value of  $a_6$ , which is representing magnetic excitations, is  $1.7 \pm 0.2$ . Our  $M_r(T)$  is the quantity similar to that of ref. 21 and actually almost reproduces the behaviour reported there.

From these results, we can conclude that we succeeded in observing magnetic ordering in  $\kappa$ -Cl under zero-field condition for the first time. We also succeeded in estimating the values of internal fields at two muon sites by means of precession frequency of  $\mu$ SR spectra. With these results, we continue to investigate the magnetic ordering in another antiferromagnet, d8- $\kappa$ -Br.

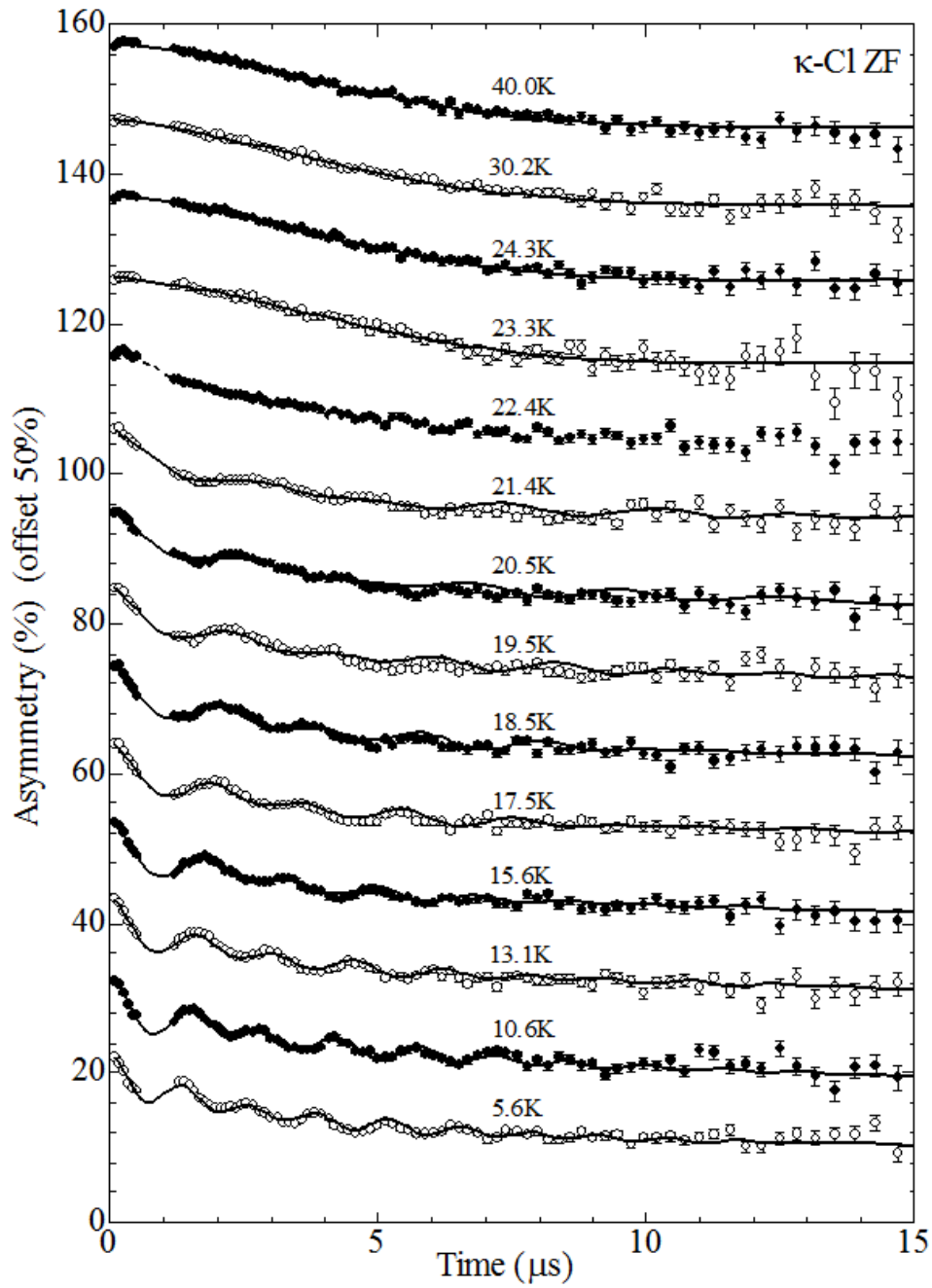
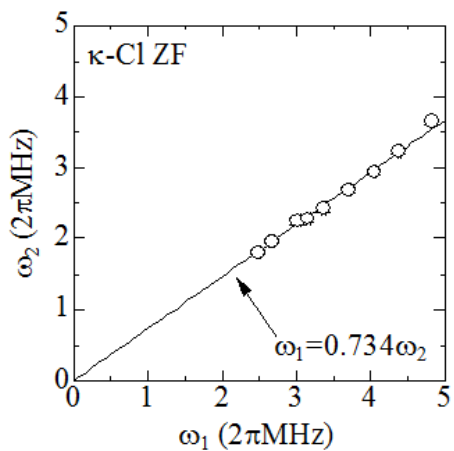
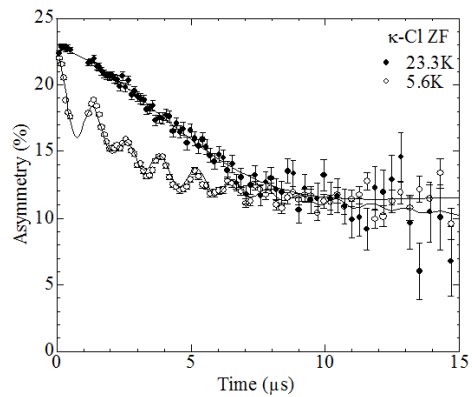


Figure 4.1.1:  $\mu$ SR spectra of  $\kappa$ -Cl in several temperatures with fitted result (see text for details). Each spectra was shifted by 50 % for clear demonstration.



(a) Relation between two rotation frequency in  $\kappa$ -Cl. Fitted line is also shown.



(b) Revisited result with fixed frequency ratio.

Figure 4.1.2: Details of estimation of model function.

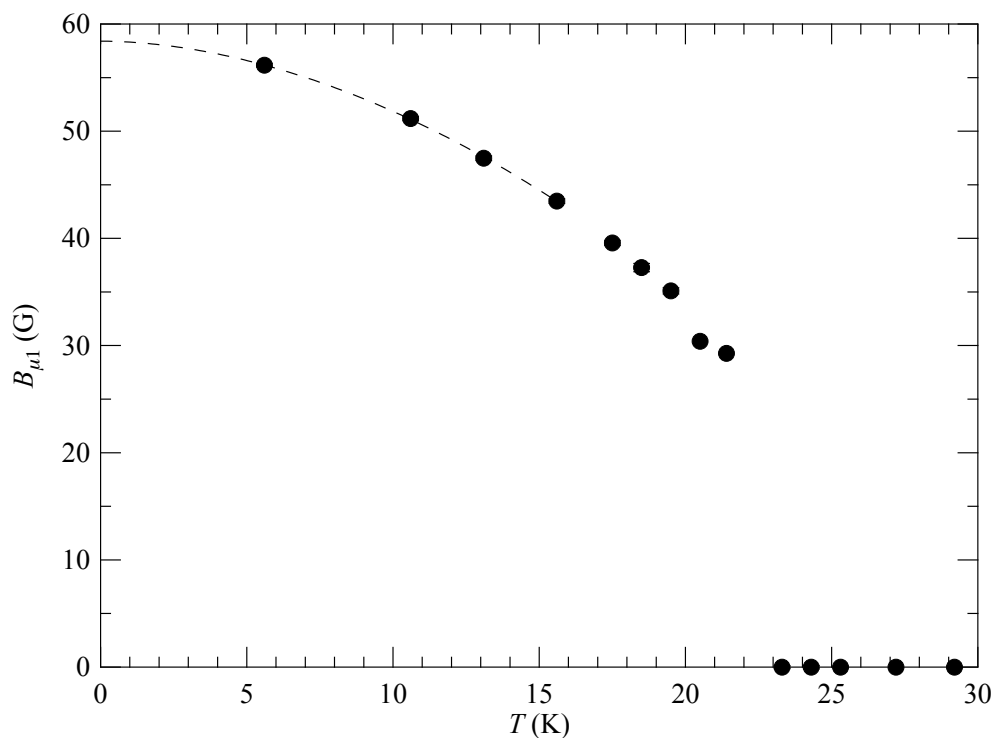
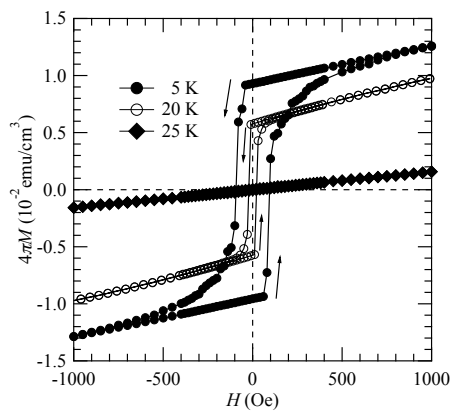
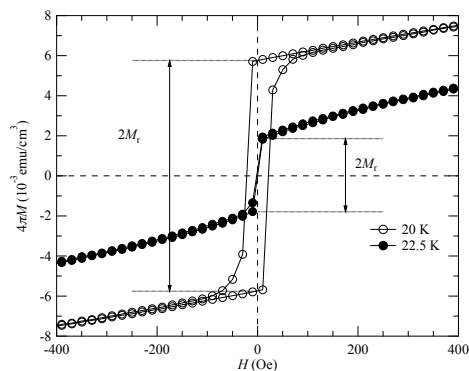


Figure 4.1.3: Temperature dependence of internal field  $B_{\mu 1}$  of  $\kappa$ -Cl.  $B_{\mu 1}$  were converted from rotational frequency by relation as  $\gamma_{\mu} B_{\mu 1} = \omega_1$  when gyromagnetic ratio of muon  $\gamma_{\mu} = 2\pi \times 13.554\text{kHz} / \text{G}$



(a) Irreversible behaviour of isothermal magnetisation in several temperatures.



(b) Examples of  $M_r$  estimation at 20 and 22.5 K.

Figure 4.1.4:  $M$ - $H$  curve of  $\kappa$ -(BEDT-TTF) $_2$ Cu[N(CN) $_2$ ]Cl in several temperature.

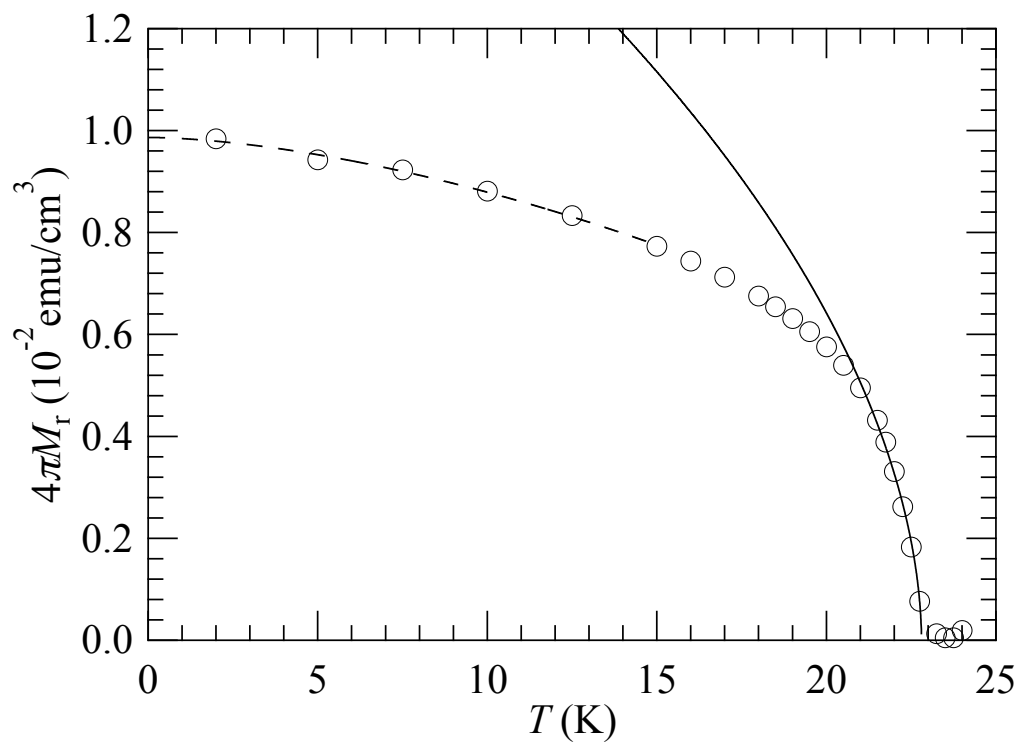


Figure 4.1.5: Temperature dependence of residual magnetisation  $M_r$  of  $\kappa$ -Cl. Fitted results are shown in solid and dashed curves (see text for details).

## 4.2 $\kappa$ -(d8-BEDT-TTF)<sub>2</sub>Cu[N(CN)<sub>2</sub>]Br

As in the case of  $\kappa$ -Cl, we measured magnetisation ( $M$ ) as a function of magnetic field parallel ( $H_{\parallel}$ ) and perpendicular ( $H_{\perp}$ ) to the conducting layers at several temperatures. In the perpendicular configuration, low-field magnetisation,  $M(H_{\perp})$ , is dominated by the contribution of the superconductivity as shown in Fig. 4.2.1 (a); the signal of the magnetic phase is hidden behind the huge peak at the zero field, which originates from the contribution of pinned vortices. The volume fraction of the superconductivity was evaluated in the Meissner state to be 8.9 % for the total volume, which is roughly consistent with previous reports [27, 51]. On the other hand, the magnetisation in the parallel field configuration,  $M(H_{\parallel})$ , does not show such a central peak. This is because the orbital current is effectively suppressed in this configuration. Hereafter, in order to get an insight into the magnetic phase, we focus on  $M(H_{\parallel})$ .

Figure 4.2.1 (b) shows isothermal magnetisation,  $M(H_{\parallel})$ , for various temperatures. While a linear profile is observed at 16.0 K for plotted field region, distinct nonlinear behaviours manifest at low temperatures. This behaviour, however, considerably differs from that of weak ferromagnetism of  $\kappa$ -Cl [18, 33]. Firstly, the value of the magnetic field for the saturation is quite different between the two salts. This value of  $\kappa$ -Cl, which would depend on the field-direction within the plane, was reported to be around 100 Oe [18]. On the other hand, d8- $\kappa$ -Br shows kink structures in  $M - H$  curve at around 3 kOe. We confirmed the absence of in-plane anisotropy in magnetisation through the measurements in two in-plane configurations along with diagonal of crystal. Therefore, we conclude that this salt has isotropic and very high saturation field, which is reminiscent of the disordered spin system. A second difference is absence or smallness of the hysteresis. In the case of  $\kappa$ -Cl, the residual magnetisation is large enough to be regarded as the spontaneous magnetisation [18, 33]. On the other hand, d8- $\kappa$ -Br has almost no residual magnetisation and no hysteresis down to 6.5 K. Although small hysteresis are observed at 4.5 and 5.5 K, as shown in the panel (a), we cannot exclude the possibility of contribution of the residual vortex, which may be caused by the misalignment of the sample against magnetic field. These results suggest that the ferromagnetic phase of d8- $\kappa$ -Br does not require so prominent domain structure to

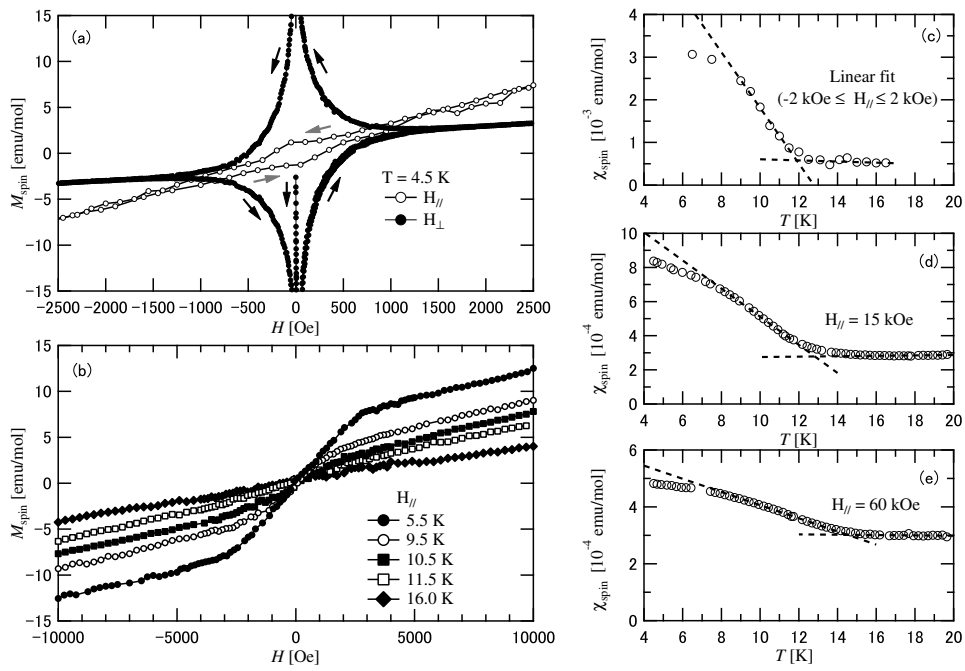


Figure 4.2.1: (a) (b) Isothermal magnetisation of d8- $\kappa$ -Br as a function of magnetic field in two directions at several temperatures. The core diamagnetism was already subtracted. (c) (d) (e) Spin susceptibility of d8- $\kappa$ -Br as a function of temperature (see text for details.)

compensate electromagnetic energy, which is very probably due to the disordered nature on the spin system.

Panels (c), (d) and (e) shows temperature dependence of susceptibility for various magnetic fields where susceptibility is defined as linear fits of  $M - H_{\parallel}$  in the range of  $-2 - 2$  kOe,  $M(15 \text{ kOe})/15 \text{ kOe}$  and  $M(60 \text{ kOe})/60 \text{ kOe}$ , respectively. As observed in the panels, the magnetic transition temperature is enhanced with increasing magnetic field. We defined  $T_N$  as the temperature at which two linear-fitted lines cross each other, as demonstrated by dashed lines. Obtained values are listed in Table 4.2.1 and ordering temperature seems to be enhanced by magnetic field.

$\chi$ (0 kOe)	$\chi$ (15 kOe)	$\chi$ (60 kOe)
$11.8 \pm 0.7 \text{ K}$	$12.8 \pm 0.2 \text{ K}$	$14.6 \pm 0.2 \text{ K}$

Table 4.2.1: Magnetic transition temperature of d8- $\kappa$ -Br.

To investigate the effect of magnetic field, zero-field  $\mu$ SR experiments are performed on d8- $\kappa$ -Br. Figure 4.2.2 showing  $\mu$ SR spectra of d8- $\kappa$ -Br in several temperatures. These spectra fitted with equation 4.2 with fitting parameter of  $A_s$ ,  $A_{\text{const}}$ ,  $B_i$ ,  $\lambda_0$ ,  $\lambda_i$ ,  $p_i$ ,  $p_3$ ,  $\Delta$  and  $\phi$ .

$$A(t) = \begin{cases} A_s e^{-\lambda_0 t} G_{\text{KT}}(\Delta, t) + A_{\text{const}} & (T > 10.2 \text{ K}) \\ A_s [\sum_{i=1}^2 p_i e^{-\lambda_i t} \cos(\gamma_{\mu} B_i t + \phi) + p_3 e^{-\lambda_3 t} G_{\text{KT}}(\Delta, t)] + A_{\text{const}} & (T < 10.2 \text{ K}) \end{cases} \quad (4.2)$$

Parameters  $A_s$  and  $A_{\text{const}}$  represents amplitude of signal from sample and background, respectively. In model function for rotational spectra, relaxational component (which is labeled as  $i = 3$ ) is composed of Kubo-Toyabe and exponential relaxation function, which may detect a relaxation component from nuclear dipole field as finite value of  $\Delta$ .

As same as in the case of  $\kappa$ -Cl, rotational signals are founded and fitted below 9.2 K. As for the spectrum of 10.2 K, we could not fit the data by above two models. However, a growth of the rapid relaxation component that has the static origin has already started at this temperature. Therefore, transition temperature into the magnetic phase is deduced to be between 12.1 and 10.2 K. The temperature dependence of  $B_1$  is shown in Fig. 4.2.3 (a). Low-temperature data were fitted

Material	$T_N$ [K]	$B_{\mu 1}(0)$ [G]	$B_{\mu 1}(0)$ [G]	$\lambda_1(T_N/2)$ [ $1/\mu\text{s}$ ]
d8- $\kappa$ -Br	$11.8 \pm 0.7$	$37.1 \pm 1.7$	$18.9 \pm 0.9$	$1.0 \pm 0.1$
$\kappa$ -Cl	$22.80 \pm 0.02$	$58.4 \pm 0.4$	$42.9 \pm 0.3$	$0.14 \pm 0.03$

Table 4.2.2: Magnetic properties and several parameters obtained from  $\mu\text{SR}$  for d8- $\kappa$ -Br and  $\kappa$ -Cl.  $T_N$  was estimated from magnetisation measurements.

by  $B_1(T) = a_1(1 - (T/a_2)^{a_3})$  and the value of  $B_1(0)$  ( $\equiv a_1$ ) was obtained as  $37.1 \pm 1.7$  Gauss. This extrapolated value of the internal field,  $B_1(0)$ , and that of the other internal field,  $B_2(0)$  are listed in Table 4.2.2. For comparison, these values of  $\kappa$ -Cl [33] are also listed in the table. The panel (a) also shows the corresponding relaxation rate,  $\lambda_1$ . In order to compare the nature of the precession signal of d8- $\kappa$ -Br with that of  $\kappa$ -Cl, a relaxation rate at a half of  $T_N$  is defined as  $\lambda_1(T_N/2)$ . This value is also tabulated for the two salts in the table, which will be discussed later. Figure 4.2.3 (b) shows the behaviour of relaxing components above and below  $T_N$ . As shown in the figure, below 12 K, the relaxation rate,  $\lambda_0$ , rapidly increases and the value of  $\Delta$  vanishes. This suggests that the low-temperature relaxing signal comes from the magnetically ordered phase or the paramagnetic phase with strong magnetic fluctuation. We also performed the longitudinal  $\mu\text{SR}$  at the lowest temperature and found that the spectrum was completely decoupled below 100 G. Therefore we can exclude the latter possibility. In this way, three components with indices  $i = 1, 2$  and  $3$  turn out to represent the static magnetic phase. This suggests that the large portion of the sample except for SC domain (8.9 %) is the magnetically ordered phase. (We could not detect the signal of the SC domain in the  $\mu\text{SR}$ .) A panel (c) shows volume fractions of the two precession signals and relaxation one. We also determined volume fractions of  $\kappa$ -Cl in our previous work [33]. The total volume of the rotational signal is approximately 38 and 30 % for d8- $\kappa$ -Br and  $\kappa$ -Cl at low-temperature region. The similar value may indicate that the rate of the muon that is stopping at the major two locations to the total muon are almost common for the two salts, which seems to indicate the muon sites are the same between the two salts.

In this material, from magnetisation measurement, magnetic ordering is believed to occur at approximately 14 to 15 K [27]. Our results of ZF study is far suppressed compared to the result under the finite magnetic field, which seems the

same situation [21] as  $\kappa$ -Cl. On the other hand, one of the important differences is the degree of disorder in the spin system. The  $^{13}\text{C}$ -NMR study reported that the line shape of d8- $\kappa$ -Br in the ordered phase was significantly broad [28]. We have also observed several pieces of evidence of the disorder effect such as large saturation field and the absence of the hysteresis in  $M - H$  curves. In addition, as listed in Table 4.2.2, a damping rate of the oscillation signal of d8- $\kappa$ -Br is seven times larger than that of  $\kappa$ -Cl, which suggests that d8- $\kappa$ -Br has more disordered internal field distribution. To investigate this scenario, we need to visit two origins of the structural disorder. One is incommensurate superlattice [52] formed below 200 K and the other is glass transition of the ethylene group at around 80 K [27, 53]. These two structural distortions will make the ordered moment to be modulated. On the other hand, the short range order may cause the disordered spin system. The d8- $\kappa$ -Br salt is believed to have a smaller value of  $U/t$  than that of  $\kappa$ -Cl where  $U$  is on-site Coulomb energy. This suggests that the intralayer exchange interaction of d8- $\kappa$ -Br is larger than that of  $\kappa$ -Cl. This situation, with the strong two-dimensionality of the spin system, seems to cause more often short-range order. These structural and electronic origins with their cooperation may cause disordered spin system.

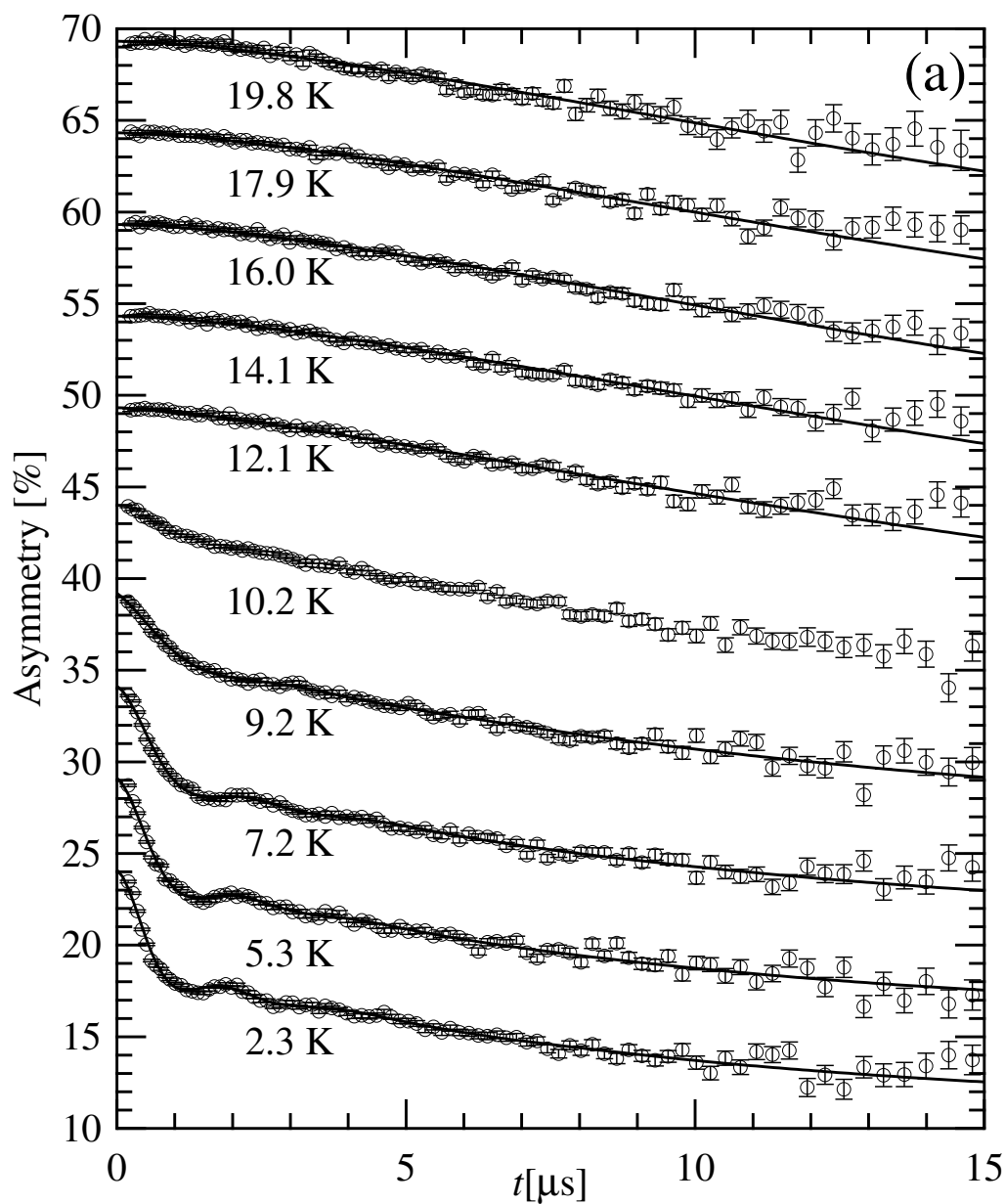


Figure 4.2.2:  $\mu$ SR spectra of d8- $\kappa$ -Br in several temperature. Each data was shifted by 5 % of asymmetry for clear demonstration.

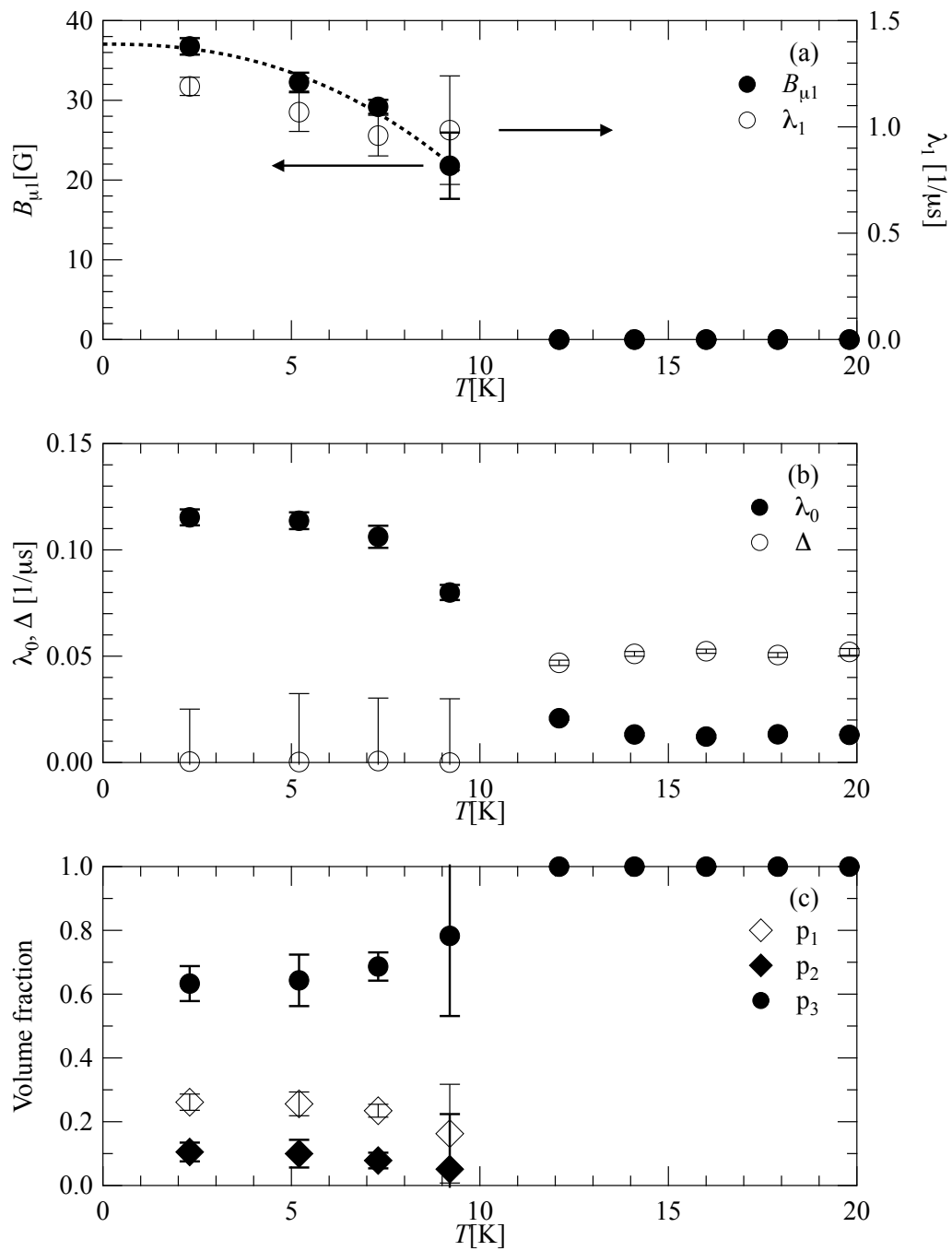


Figure 4.2.3: Fitted parameters of d8- $\kappa$ -Br as functions of temperature.

### 4.3 $\kappa$ -(d8-BEDT-TTF)<sub>2</sub>Cu[N(CN)<sub>2</sub>]Cl

As mentioned in the previous sections, we could not determine the critical exponent  $\beta$  of the magnetic ordering of  $\kappa$ -Cl and d8- $\kappa$ -Br. This is due to technical difficulties listed below.

- Fast relaxation at paramagnetic state that behave as background signal [ $\kappa$ -Cl]
- Fewer data points near ordering temperature [d8- $\kappa$ -Br]
- Rapid damping of precession signal due to disorder [d8- $\kappa$ -Br]
- Limitation of time resolution due to time structure of pulsed beam [both salts]

From these points, deuterated  $\kappa$ -Cl, d8- $\kappa$ -Cl with continuous-wave structure beam is a reasonable experimental condition due to higher  $T_N$  and time resolution. Figure 4.3.1 shows selected  $\mu$ SR spectra of d8- $\kappa$ -Cl taken from an experiment performed at Paul Scheller Institut (PSI). The time structure of the muon beam at PSI allow us to obtain the spectra only in a shorter time region ( $0 < t < 8 \mu\text{s}$ ). They clearly show precession behaviour at low temperatures, which suggests appearance of the magnetic ordering. To estimate the onset temperature of magnetic ordering, each spectrum should be fitted by reasonable model function.

Before constructing a model, the number of rotational components (i.e. the number of muon sites) should be clarified. For that purpose, we performed fast Fourier transformation (FFT) for time spectra at 1.6 K and result is shown in figure 4.3.2. Rotational frequency  $f$  was converted to the internal field by the relation  $B = 2\pi f \gamma_\mu$  with gyromagnetic ratio of  $\mu^+$ ,  $\gamma_\mu$ . Three arrows in fig. 4.3.2 are indicating founded peaks at around 40, 60 and 120 G. Internal fields of first two peaks seem to coincide with that of two precession signals of  $\kappa$ -Cl [33], but the third peak with the strongest internal field was not found in  $\mu$ SR spectra of  $\kappa$ -Cl even in the lowest temperature. This fact seems to be quite controversial if we consider the fact that only differences between both materials are hydrogen and deuterium situate the end of ET molecule. From this point, we need to investigate this third rotational component up to higher temperature nearby  $T_N$ . For that

reason, analytical function for d8- $\kappa$ -Cl was estimated as equation 4.3 with fitting parameters as  $p_i$ ,  $p_4$ ,  $B_i$ ,  $\lambda_i$ ,  $\lambda_4$ ,  $A_s$  and  $A_{bg}$  with  $i = 1, 2$  and  $3$ .

$$A(t) = A_s \left[ \sum_{i=1}^3 p_i \cos(\gamma_\mu B_{\mu i} t) e^{-\lambda_i t} + p_4 e^{-\lambda_4 t} \right] + A_{bg} \quad (4.3)$$

Fitted results for the spectra at 1.6 K were shown in table 4.3.1. It should be noted

Component	$p_i$	$B_i$ [G]	$\lambda_i$ [1/ $\mu$ s]
$i = 1$	$0.17 \pm 0.01$	$59.5 \pm 0.2$	$0.19 \pm 0.03$
$i = 2$	$0.11 \pm 0.01$	$44.2 \pm 0.2$	$0.33 \pm 0.07$
$i = 3$	$0.14 \pm 0.01$	$114 \pm 0.4$	$1.01 \pm 0.14$
$i = 4$	$0.58 \pm 0.01$	-	$0.35 \pm 0.01$

Table 4.3.1: Fitted parameter of  $\kappa$ -(d8-BEDT-TTF) $_2$ Cu[N(CN) $_2$ ]Cl at 1.6 K

that only the strongest-field component has comparably larger (i.e. faster) time constant of envelope. This fitting analysis also applied to the high-temperature spectra and figure 4.3.3 shows the relation between fitted internal fields. As observed in the fig. 4.3.3, two data sets show linear behaviour, which suggests that three components originate from identical ordered spins lying in BEDT-TTF dimer. Hereafter, the ratio between these internal fields are fixed as eq. 4.4.

$$B_{\mu 2}/B_{\mu 1} = 0.73, B_{\mu 3}/B_{\mu 1} = 1.92 \quad (4.4)$$

After this treatment, examples of revisited fitted results are shown in 4.3.4 (for clear view of fitting, only shorter time region is plotted). We succeeded in fitting all spectra without appearing any unreasonable fitted parameters such as negative time constant of the envelope. This fact raises a question about the number of the muon site. As mentioned above, the other antiferromagnets in  $\kappa$ -(ET) $_2$ X,  $\kappa$ -Cl and d8- $\kappa$ -Br, have only two rotational components, which suggests existence of magnetically independent two muon sites. Since the crystal structures of  $\kappa$ -Cl and d8- $\kappa$ -Cl are common, the different results seem to be unreasonable. To clarify the origin of this difference, we need to reconsider the previous results of  $\kappa$ -Cl.

Figure 4.3.5 shows each fitted rotational component and the total of rotational components,  $A(t) - (A_s * p_4 e^{-\lambda t} + A_{bg})$ . This figure indicates that the shape of

spectra in the range of  $0.5 - 1.0 \mu\text{s}$  seems to be quite important for detection of the strongest-field component. However, spectra data of  $\kappa\text{-Cl}$  in such time range is absent by extrinsic noises from kicker magnet, which makes detection of the third component harder. In the case of  $\text{d8-}\kappa\text{-Br}$ , disordered nature of its spin system also makes such detection harder. Due to these issues, the third precession signal may be overlooked in the previous work. It should be noted that previous works of  $\kappa\text{-Cl}$  and  $\text{d8-}\kappa\text{-Br}$  were performed using pulsed muon beam at Rutherford-Appleton laboratory. The pulsed beam structure has inevitable time uncertainty as mentioned earlier (see section 2.3 for details). Such time uncertainty may also interfere with the observation of third precession component. Therefore, the result of  $\text{d8-}\kappa\text{-Cl}$  may suggest that three antiferromagnets,  $\kappa\text{-Cl}$ ,  $\text{d8-}\kappa\text{-Br}$  and  $\text{d8-}\kappa\text{-Cl}$ , have three muon sites in common. Actually, in the case of the lowest-temperature spectrum of  $\kappa\text{-Cl}$ , we succeeded in fitting the spectra by the model functions composed of three precession components. Two of precession components have similar fitted value of internal field and time constant of envelope as in the case of previous two-precession model function.

Figure 4.3.6 shows temperature dependence of the largest internal magnetic field,  $B_{\mu 3}$ . As observed in the figure, the internal field vanishes around 24.5 K which is slightly larger than that of  $\kappa\text{-Cl}$  (22.8 K). This difference is expected to originate from enhancement of the electronic correlation by the deuteration. To investigate the criticality of this transition, we fit this data by a function (4.5) in the vicinity of  $T_N$  ( $15 \text{ K} < T < 25 \text{ K}$ ) with fitting parameters,  $B_{\mu 3}(0)$ ,  $T_N$  and  $\beta$ . Fitted results are displayed in fig. 4.3.6 and listed in table 4.3.2.

$$B_{\mu 3}(T) = B_{\mu 3}(0) \left(1 - \frac{T}{T_N}\right)^\beta \quad (4.5)$$

Above magnetic ordering, muons are expected to detect internal field which originates

Fitted parameter	$B_{\mu 3}(0)$ [G]	$T_N$ [K]	$\beta$
	$155.9 \pm 9.8$	$24.4 \pm 0.01$	$0.34 \pm 0.02$

Table 4.3.2: Fitted parameters of internal field of  $\kappa\text{-(d8-BEDT-TTF)}_2\text{Cu[N(CN)}_2\text{]Cl}$

the nuclear dipole. That causes tail around ordering temperature when magnetic field from ordered electron spin is comparable to that from the nuclear dipole. For

that reason, data points above 24.4 K are excluded from fitting analysis. From this fitted result, a critical exponent of  $\beta$  is estimated as  $0.34 \pm 0.02$  that agrees with 3D-Heisenberg model ( $\beta = 0.36$ ). This finding may suggest that magnetic ordering in d8- $\kappa$ -Cl reflects interlayer exchange that reported about to  $10^{-6}$  of intralayer exchange, as in the case of  $\kappa$ -Cl [23].

However, d8- $\kappa$ -Br should have larger interlayer exchange interaction  $J_{\perp}$  compared to  $\kappa$ -Cl due to its “pressurised” situation. In such case,  $T_N$  of d8- $\kappa$ -Br should be larger than that of  $\kappa$ -Cl. Nevertheless, in reality, d8- $\kappa$ -Br has the smallest  $T_N$  among three antiferromagnets. To solve such puzzling situation, we focused on the correlation between ordering temperature and internal field,  $B_{\mu 1}$ . Figure 4.3.7 shows a correlation between  $T_N$  and  $B_{\mu 1}$  with an eye-guide. As shown in the figure, magnetic ordering temperature correlates to internal field with finite intercept. Such intercept may relate to the frustration of spin due to triangular-lattice spin system. In  $\kappa$ -(ET)<sub>2</sub>X systems, the position of muon is considered to be around the centre of the six-membered ring (which will be shown in Appendix). In such situation, it seems to be reasonable to assume that observed internal field relates not to the magnetic structure but to the magnitude of the magnetic moment itself. This result agrees with localized moment in the ordered phases, which are  $0.4 - 0.5 \mu_N$  for  $\kappa$ -Cl [18, 20] and  $0.26 \mu_N$  for d8- $\kappa$ -Br [27]. This agreement strongly suggests that peculiar decrease of  $T_N$  is actually originates from the decrease of the localized moment.

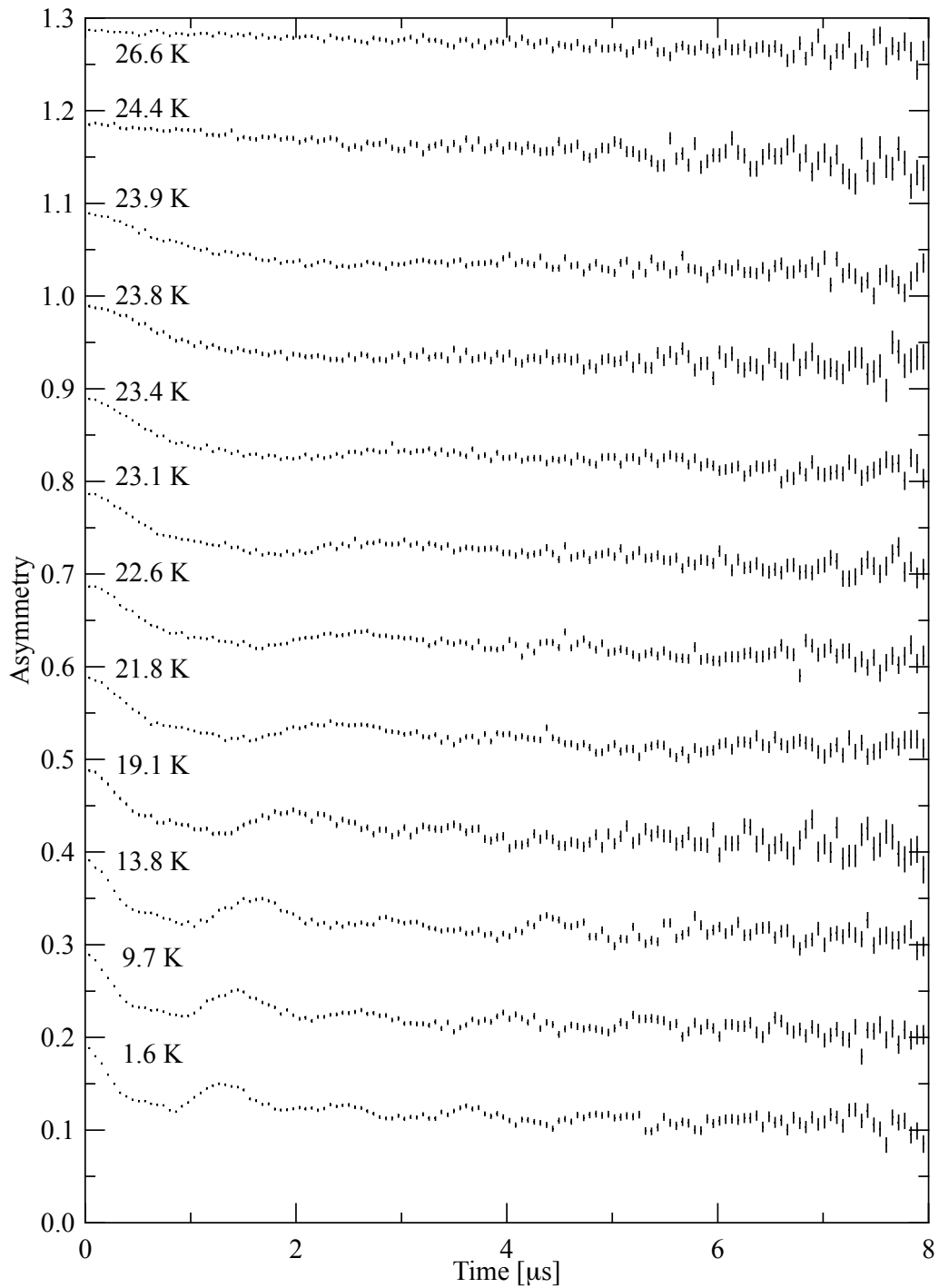


Figure 4.3.1:  $\mu$ SR spectra of  $\kappa$ -(d8-BEDT-TTF)<sub>2</sub>Cu[N(CN)<sub>2</sub>]Cl in several temperature. Each spectra are vertically shifted for clear view.

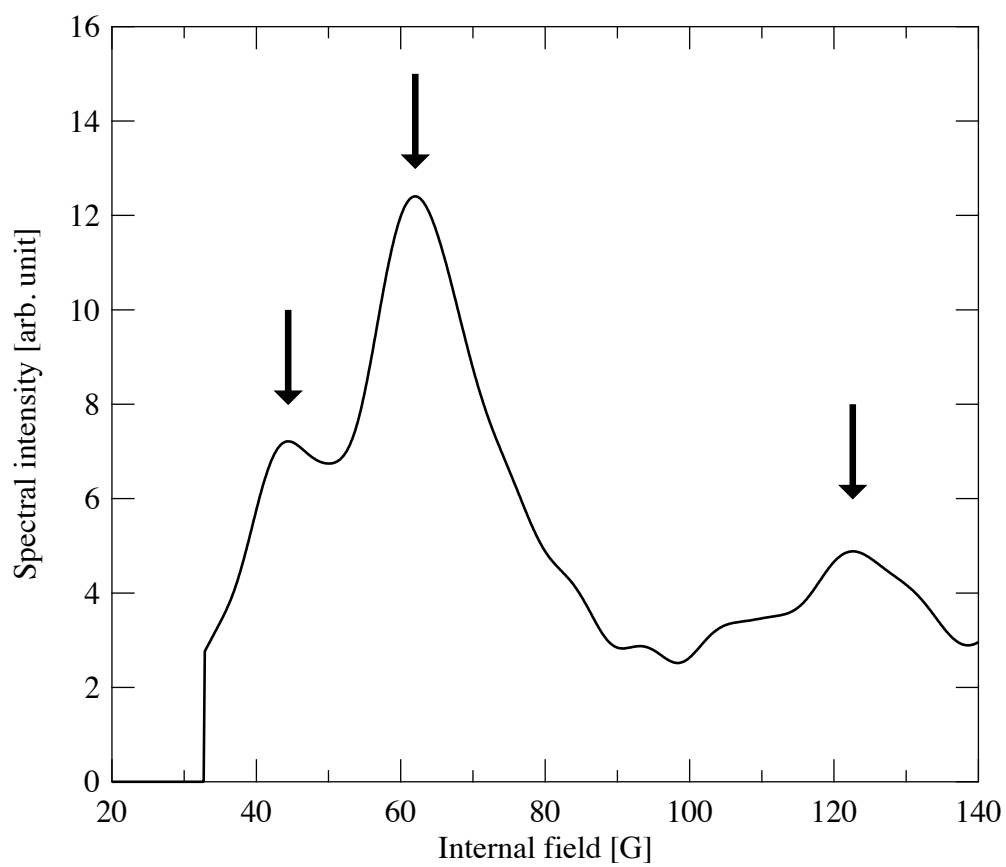


Figure 4.3.2: Internal field dependence of spectral intensity from fast Fourier transformation.

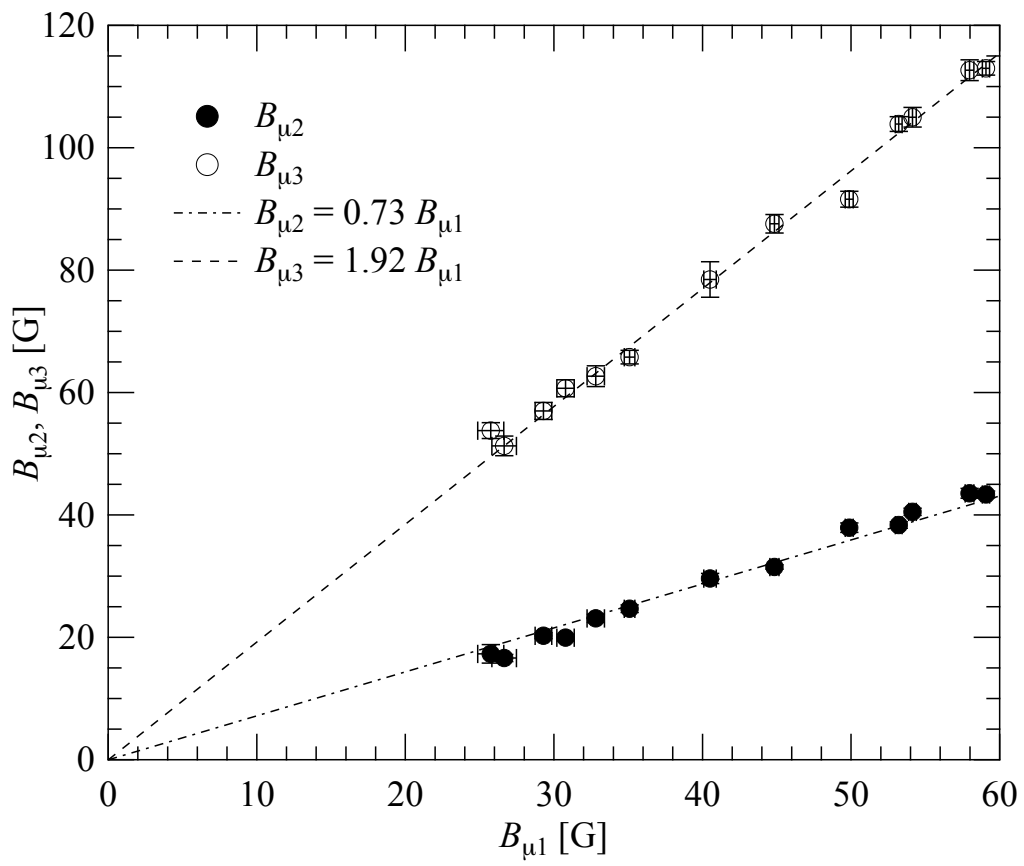


Figure 4.3.3: Relation between three internal fields with fitted lines.

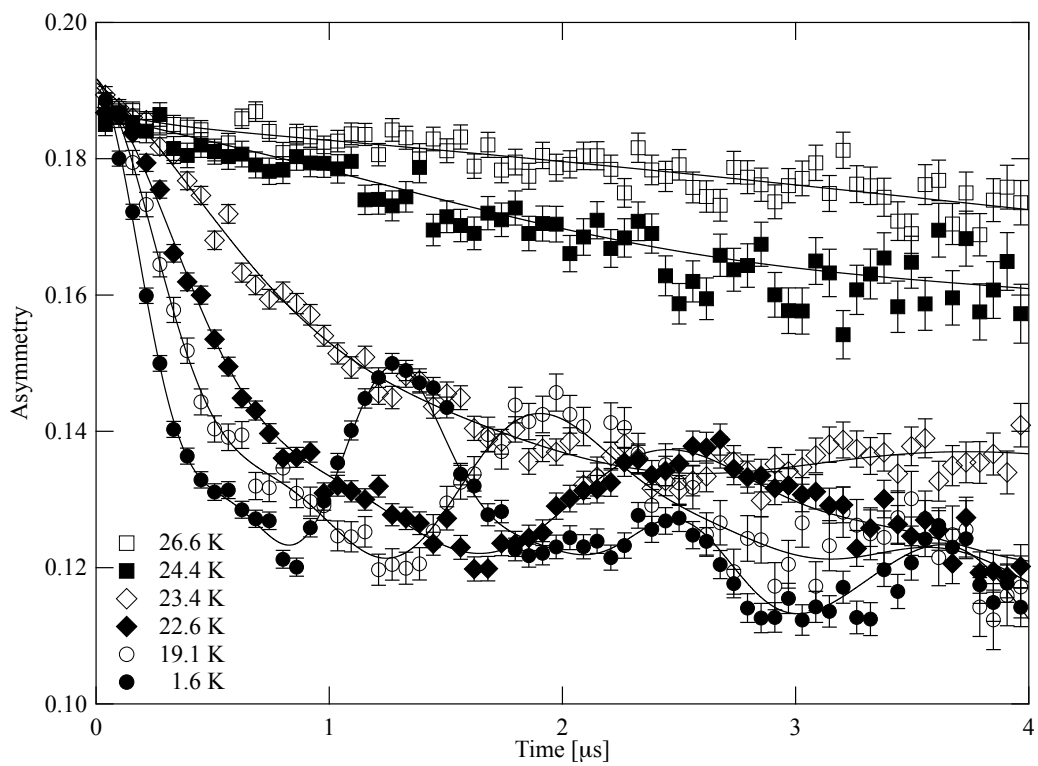


Figure 4.3.4: Examples of fitted results in several temperatures.

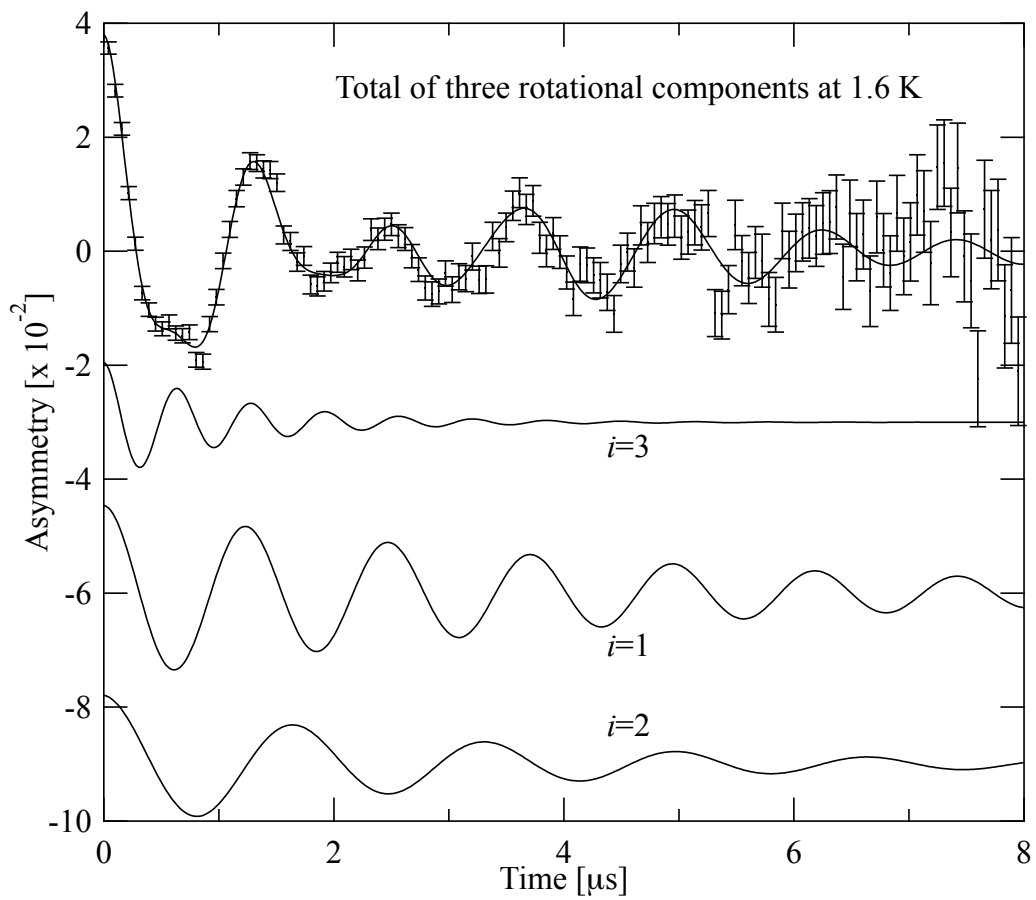


Figure 4.3.5: Detail of fitted rotation components at 1.6 K (see text for details).

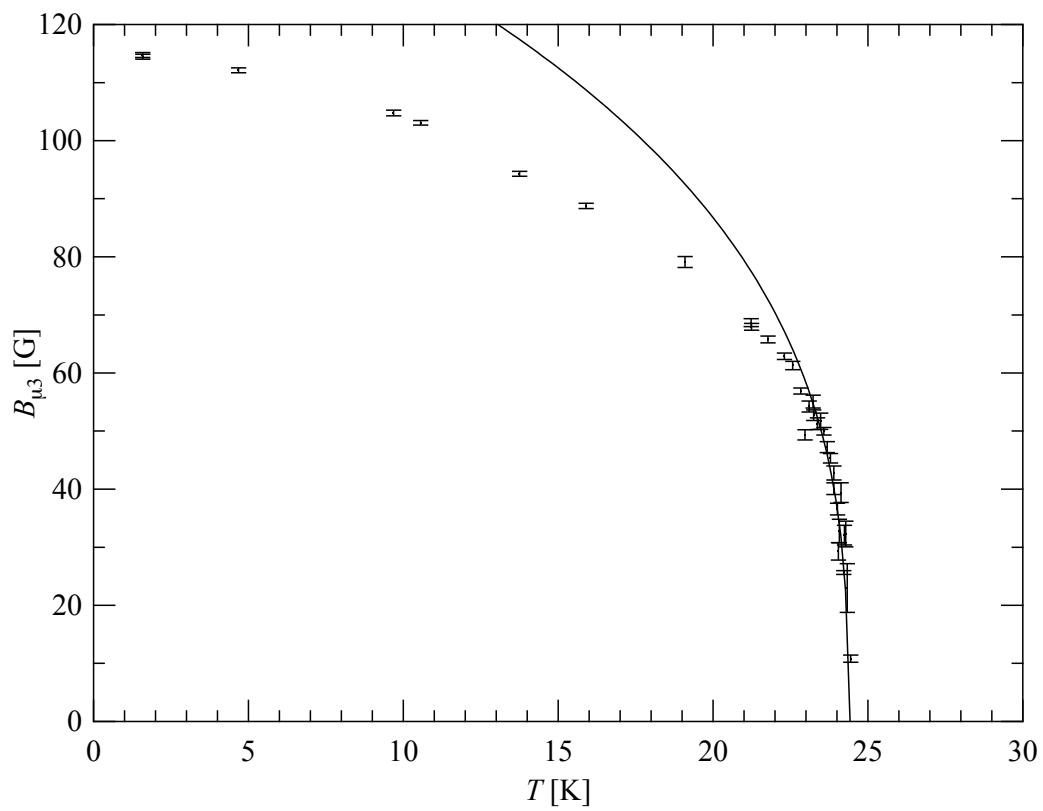


Figure 4.3.6: Temperature dependence of internal field of  $\kappa$ -(d8-BEDT-TTF) $_2$ Cu[N(CN) $_2$ ]Cl. Solid line represents the fitted result with eq. 4.5.

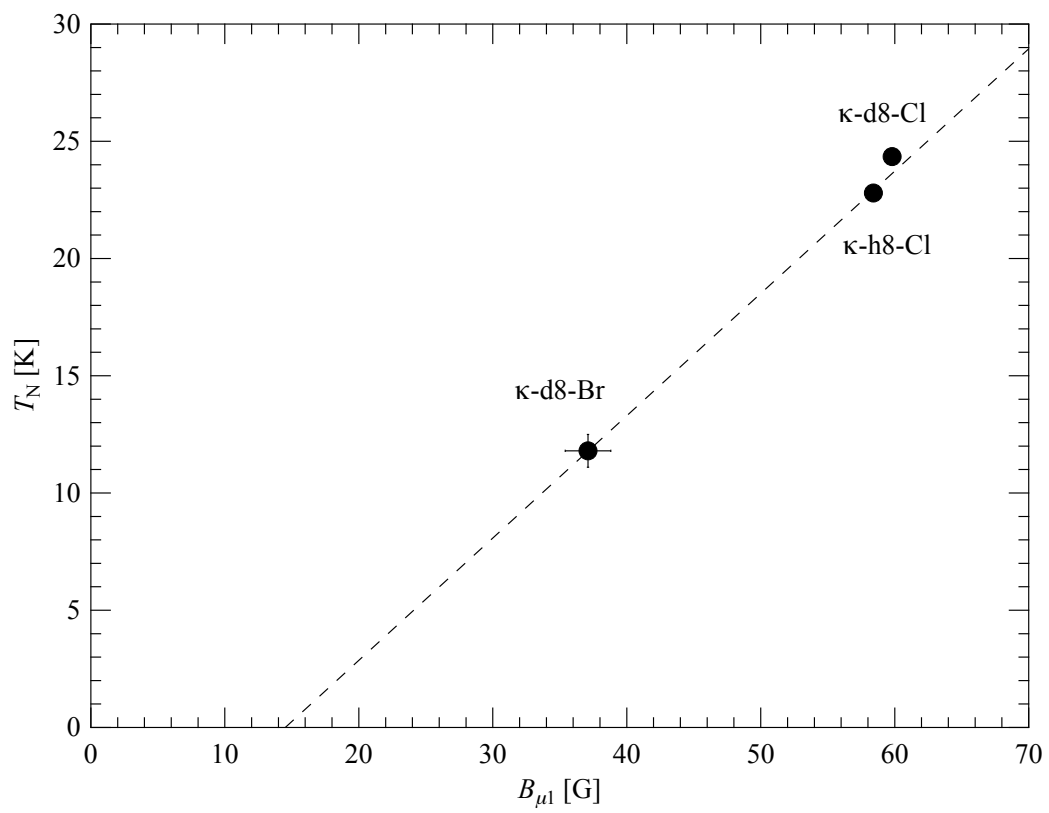


Figure 4.3.7: Correlation between ordering temperature and internal field.

## 5 Results for superconducting fluctuation

### 5.1 $\kappa$ -(BEDT-TTF)<sub>2</sub>Cu[N(CN)<sub>2</sub>]Br

The main panel of figure 5.1.1 shows the temperature dependence of magnetic susceptibility in two magnetic field directions respect to the conducting (i.e.  $ac$ ) plane. It's worth noting that magnetic susceptibility is defined as a  $M/H$  with magnetisation  $M$  and magnetic field  $H$  throughout this section. Core's contribution of  $-4.7 \times 10^{-4}$  emu/mol, which corresponds to inner-core electrons was already subtracted to display behaviour of electronic spin lying on BEDT-TTF molecules. As one can see, decreasing trend towards low temperature already started in this temperature region, which seems consistent with reported [54] results. The thin arrow in the main panel indicates that where two data show start to separate which seems to be comparable with reported  $T^*$  anomaly which is considered to be related to normal state physical property [55, 56]. Inset of fig. 5.1.1 shows magnetic susceptibility in several perpendicular fields. Thick arrow indicates where magnetic susceptibility of  $\kappa$ -Br under perpendicular field starts to show field dependence, which is around 20 K.

These results can be summarised as the following scenario. An anomaly starts at  $T^*$  came from the normal state properties, then the another anomaly which relate to SCF start at lower temperature. To investigate this scenario quantitatively, the anisotropy of magnetic susceptibility  $\Delta\chi$  is defined as  $\Delta\chi = \chi_{\parallel} - \chi_{\perp}$ . The main panel of figure 5.1.2 shows  $\Delta\chi$  in several magnetic fields in semi-logarithmic scale. The anisotropy clearly grows toward low temperature from approximately 35 K (data above this temperature are omitted because of large scattering due to its semi-logarithmic scale). Under a field of 70 kOe,  $\Delta\chi$  shows monotonic increase in this scale down to almost zero-field transition temperature,  $T_c$ , 11.6 K. 70 kOe of magnetic field may not enough to completely suppress SCF of this material but most part of that because its upper critical field is reported as 110 kOe at 0 K [57]. From this viewpoint, it can be assumed that  $\Delta\chi$  under 70 kOe contains normal-state anisotropy mostly and contribution from SCF can be found in the difference between 70 kOe and low-field data. Inset of figure 5.1.2 shows sample dependence of anisotropy from different synthesise batch and one can see

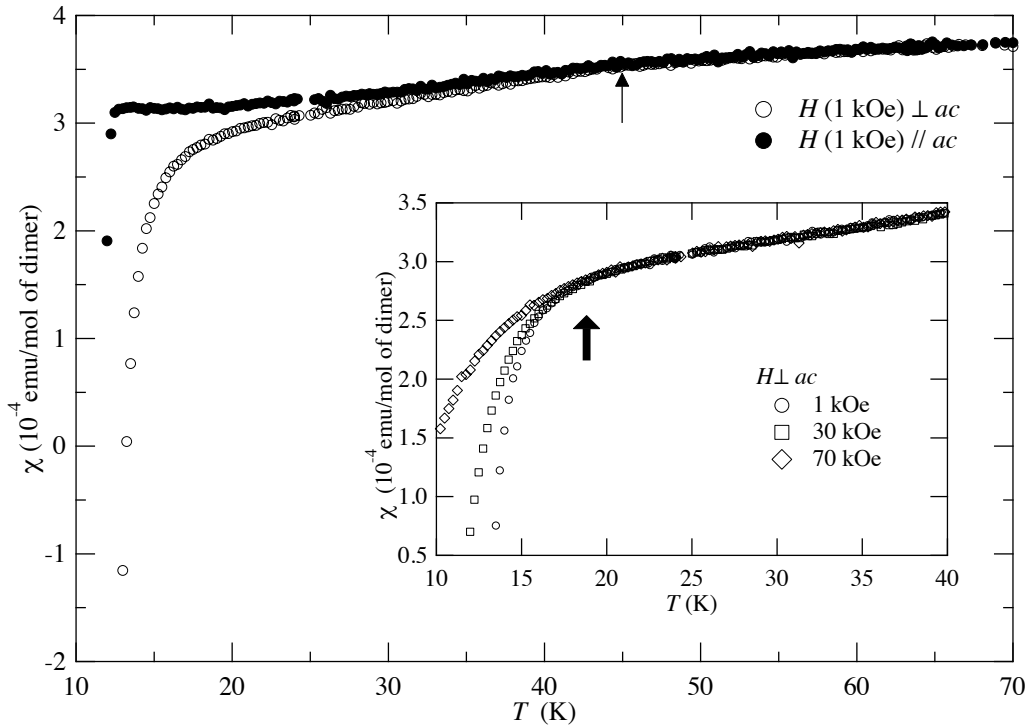


Figure 5.1.1: Temperature dependence of magnetic susceptibility of  $\kappa$ -Br.

the behaviour of anisotropy is reproducing in the precision of this measurement.

As the fact field-dependent component of  $\Delta\chi$  corresponds to SCF, it is needed to investigate its characteristic temperature dependence at low field limit.

The left panel of figure 5.1.3 shows  $\Delta\chi$  in the low field. Open symbols represent data measured under finite magnetic field and closed symbols represent fitted slope of  $\Delta M (= M_{\parallel} - M_{\perp}) - H$  plots. Some of the examples of  $\Delta M - H$  plots are shown in the right panel of figure 5.1.3. At 11.7 K, clear step observed around 0 Oe which indicates the formation of the superconducting domain. With increasing temperature,  $\Delta M - H$  curve became more smooth, which enables us to estimate  $\Delta\chi$  from its slope at 12.3 and 12.8 K and to regard them as the low-field limit at each temperature (see closed symbols on left panel).

To estimate growth of SCF component of  $\Delta\chi$ , figure 5.1.4 shows  $\Delta\chi$  at the lowest magnetic field in logarithmic scale. Panel (a) and (c) shows the relation between  $\Delta\chi$ , or  $\Delta\chi(500 \text{ Oe}) - \Delta\chi(70 \text{ kOe})$  against  $T - T_c$ . In this scale, these show almost completely linear behaviour. For estimation of the critical exponent,

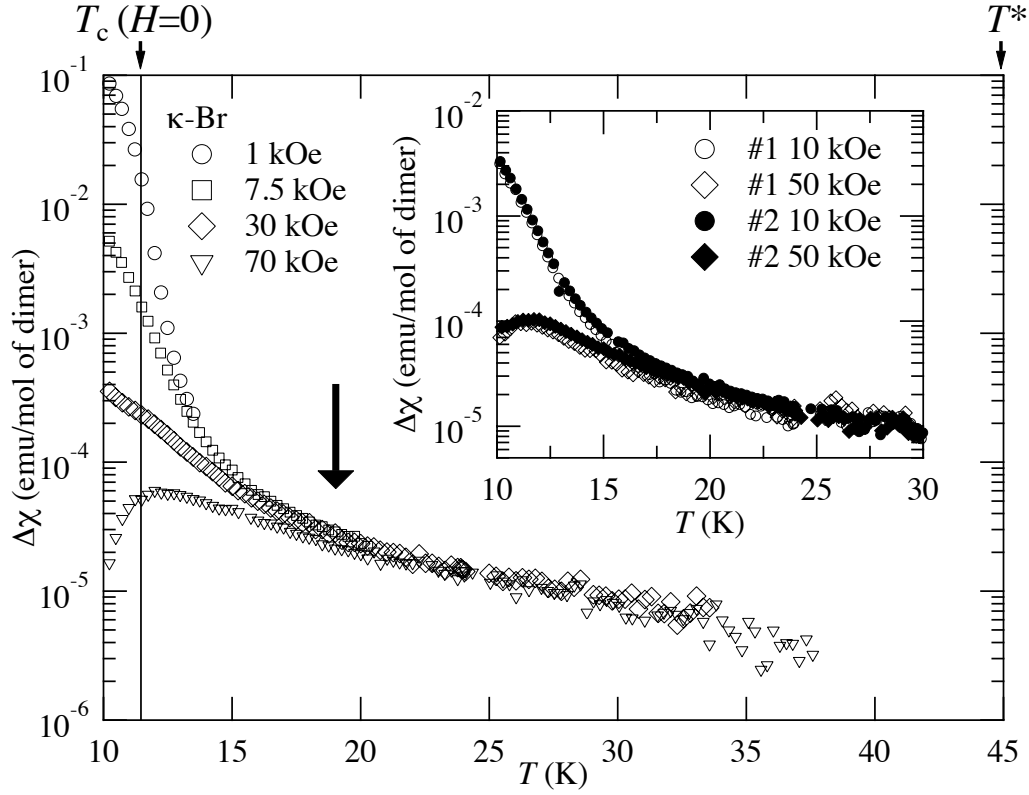


Figure 5.1.2: Anisotropy of magnetic susceptibility. Solid line represents superconducting transition and arrow indicates onset of field-dependent behaviour.

$\Delta\chi$  should give us the upper limit of the exponent, and  $\Delta\chi(500 \text{ Oe}) - \Delta\chi(70 \text{ kOe})$  should give us the lower limit of the exponent. From fitting with an equation  $\Delta\chi = A(T - T_c)^\alpha$  with fitting coefficient  $A$  and  $\alpha$ , the value of  $\alpha$  is limited in the range of  $-2.3 < \alpha < -2.0$ . Another possible model of temperature dependency is fitting equation such as  $\Delta\chi = BT(T - T_c)^\beta$  with  $\beta = 1$  which can be interpreted as the emergence of thermal amplitude fluctuation. From panel (b) and (d) of fig.5.1.4, results of  $\kappa\text{-Br}$  show linear behaviour in this scale but exponent value  $\beta$  was 2.1. This fact states that  $\kappa\text{-Br}$  shows more steep growth of SCF towards superconducting transition compared to a conventional superconductor. On the other hands, theoretical prediction with phase fluctuation states that, in triangular-lattice case, fluctuation magnetism can be expressed as  $M/T \propto (J/T)^{-3} \sin(H/H_0)$  with the constants  $J$  and  $H_0$ . This prediction also does fail to explain the steep

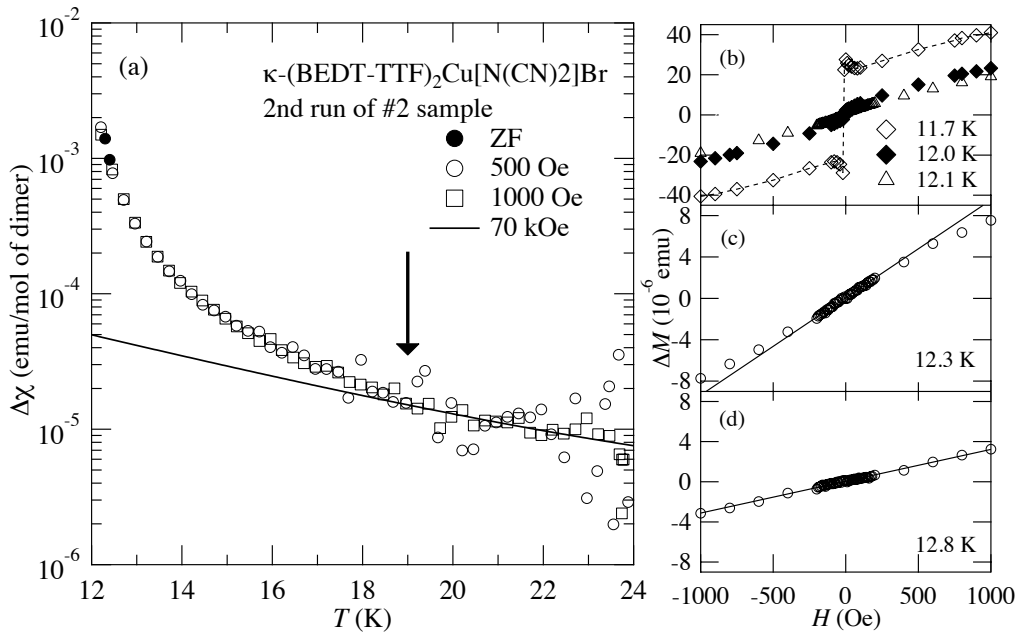


Figure 5.1.3: (a): Anisotropic component of susceptibility. Solid line represents fitted result for 70 kOe. (b)-(d): Anisotropic component of magnetisation. Dotted line is eye guide for 11.7 K and solid lines are fitted results in lower-field region.

increase of SCF component quantitatively, but the steep-growth nature of phase fluctuation can explain this results qualitatively.

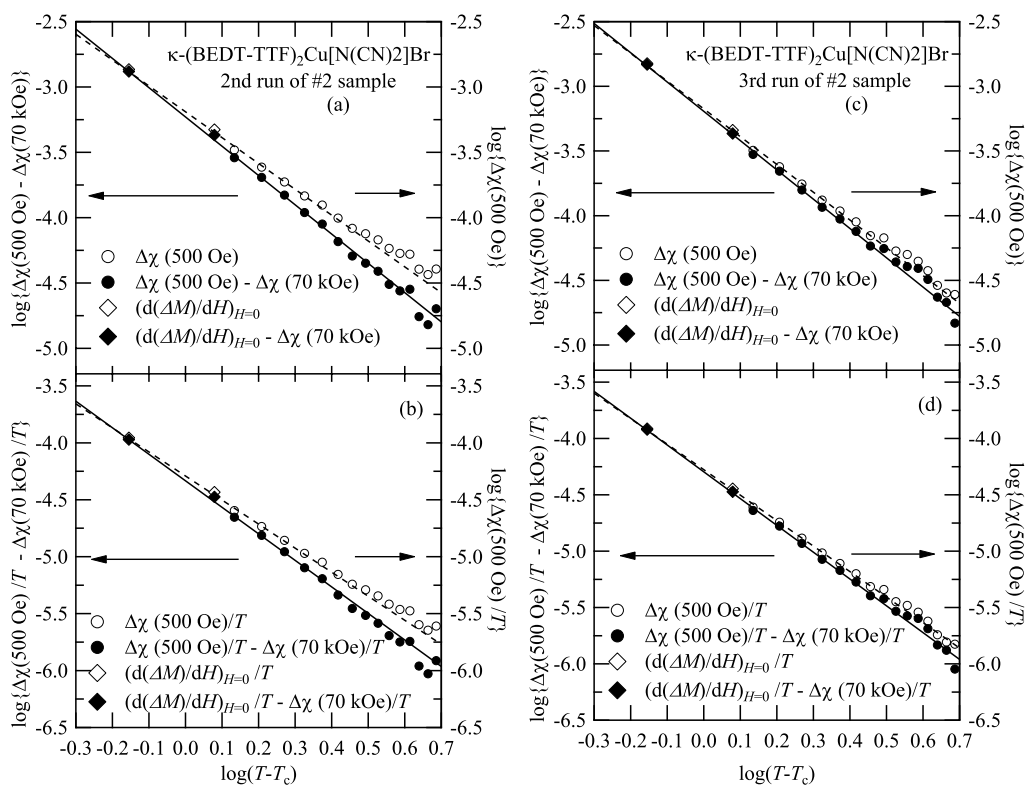


Figure 5.1.4: Temperature dependence of SCF components(see text for details).

## 5.2 Pressurised $\kappa$ -(BEDT-TTF)<sub>2</sub>Cu[N(CN)<sub>2</sub>]Cl

As mentioned in chapter 1.4, Nam *et al.* suggested the importance of Mott transition on SCF based on Nernst coefficient measurements on  $\kappa$ -Br with Cl substitution [45]. They reported that onset temperature of SCF rapidly increases while system approaches strong-correlation region.

We also investigated effect of electronic correlation on SCF by using insulating analogue of  $\kappa$ -Br,  $\kappa$ -Cl, with help of He-gas pressure. Such experiment enables us to investigate the effect of electronic correlation without inducing any disorder.

As discussed in the case of  $\kappa$ -Br, the value of contribution from SCF on magnetic susceptibility is small and even comparable to the paramagnetic signal. In addition to that, from restrictions on experiments such as the inevitable contribution from pressure cell, the precision of measurement on He-gas SQUID magnetometer is lower than that of ordinary SQUID magnetometer. Considering such situation, we compared two magnetic susceptibilities under 10 and 70 kOe and defined onset temperature of SCF by starting point of field dependence for both data sets.

Figure 5.2.1 shows spin susceptibility under 10 and 70 kOe at 13 and 18 K. At 13 K, two data sets under different fields show different pressure dependence starts at around 90 MPa (see thick arrow in figure). These points are defined as a onset point of SCF. On the other hand, at 18 K, the difference between two data sets is suppressed and onset pressure is also slightly suppressed. On the other hand, above 20 K, we could not detect this difference at metallic region (see figure 5.2.2 for example).

From these data, figure 5.2.3 shows onset points of SCF on the reported [9, 10] schematic phase diagram. As shown in the figure, onset temperature of SCF shows clearly different pressure dependence compared to that of superconducting transition. Also, the area of SCF shows almost no pressure dependence in lower-pressure region and suddenly be suppressed approximately 90 MPa. We will compare this result with three proposed mechanism of SCF.

Firstly, phase fluctuation with quantum-effect origin is proposed by Nam *et al.* [41,45]. This scenario describes reported [41,45] rapid enhancement of SCF in Nernst coefficient towards Mott transition. However, our results do not show such enhancement. This difference may suggest extrinsic surface contribution on Nernst

coefficient. Secondly, in case of classical amplitude fluctuation, the region of SCF is decided by Ginzburg number,  $G_i$  [58]. Such mechanism can explain pressure independent behaviour under 80 MPa, while it cannot demonstrate sudden drop around 90 MPa. Thirdly, a possibility of thermal fluctuation on phase is proposed [40, 59]. In such scenario, the appearance of fluctuation is decided by phase stiffness,  $V_0$  which is proportional to  $n_s/m^*$  with superfluid density  $n_s$  and effective mass  $m^*$ . These two values are supposed to be constant in this pressure region, which also fails to explain sudden drop around 90 MPa. However, possibility of dimensional crossover may describe such drop. In quasi-2D situation (low-pressure region), vortex which originates to fluctuation is supposed to form pancake vortex inside each superconducting layers. On the other hand, in anisotropic 3D system, vortices penetrate multiple superconducting layer. Such situation leads to higher cohesive energy and SCF should be suppressed. While system is pressurised, system tends to become anisotropic 3D due to enhancement of perpendicular coherence length  $\xi_{\perp}$  and suppression of transition temperature  $T_c$ . Such scenario may describe sudden drop around 80 MPa.

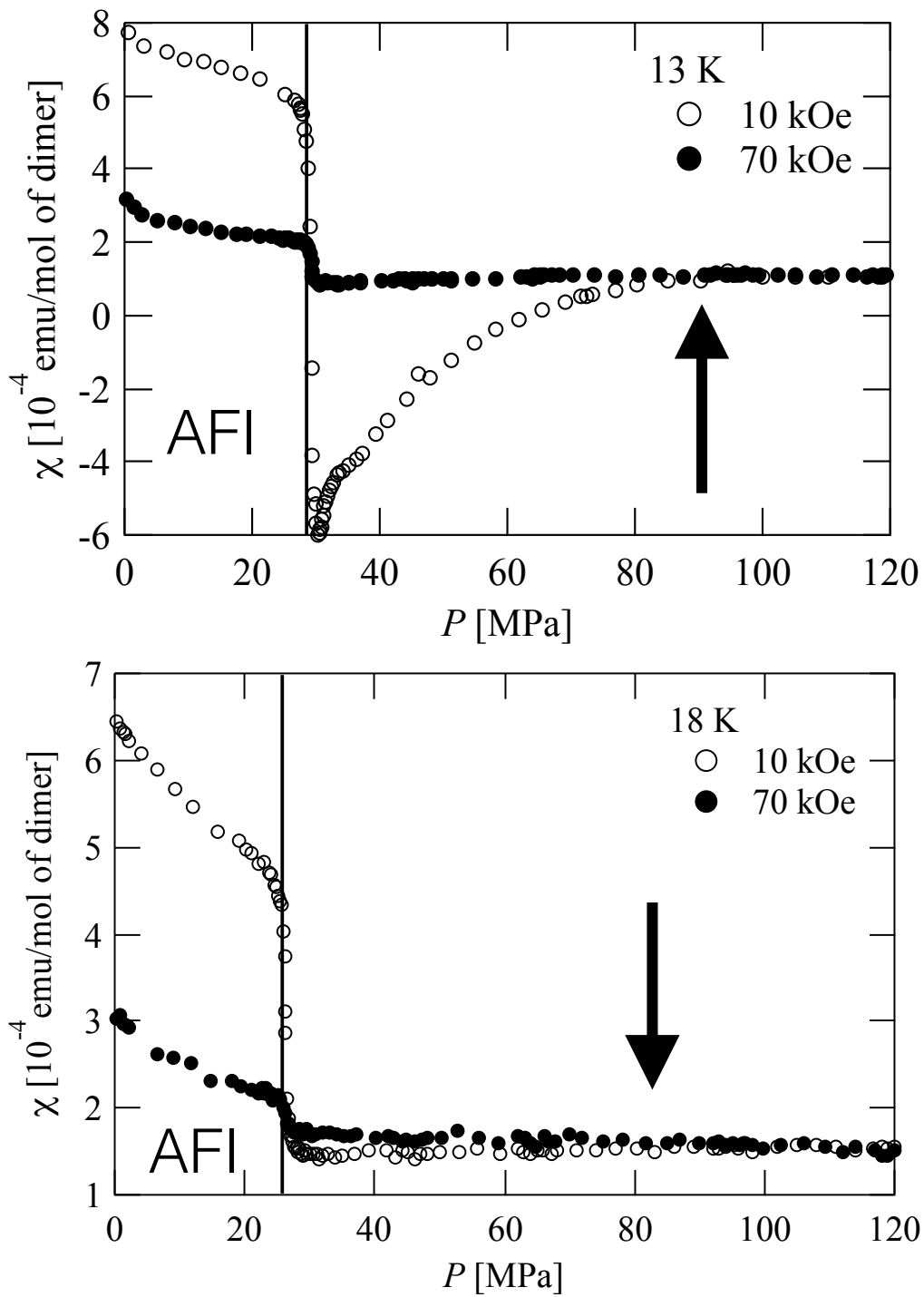


Figure 5.2.1: Spin susceptibility of  $\kappa$ -(BEDT-TTF)<sub>2</sub>Cu[N(CN)<sub>2</sub>]Cl in several temperature.

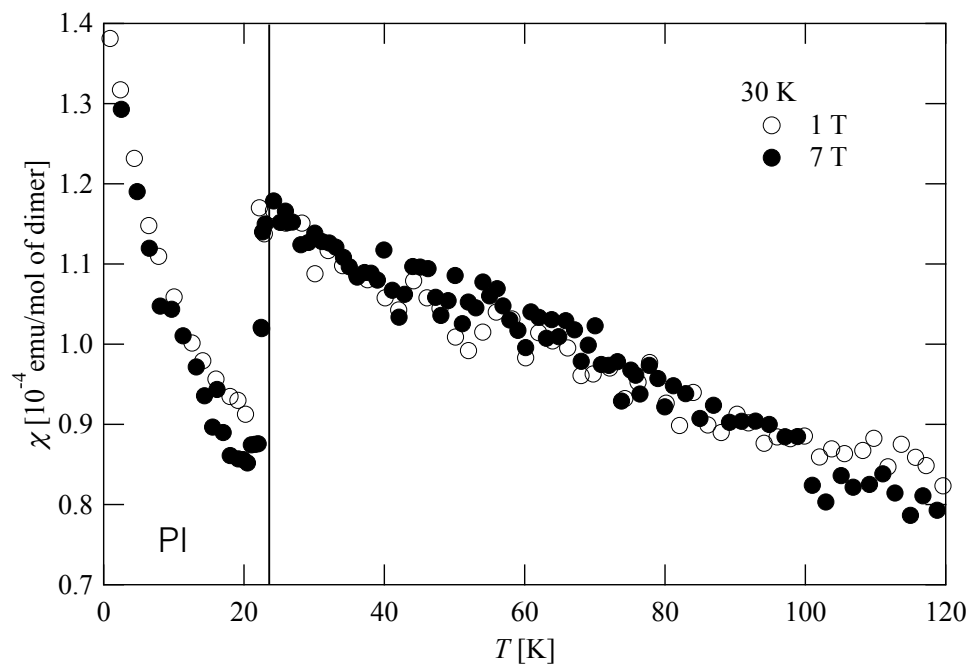


Figure 5.2.2: Spin susceptibility of  $\kappa$ -(BEDT-TTF)<sub>2</sub>Cu[N(CN)<sub>2</sub>]Cl in high temperature region.

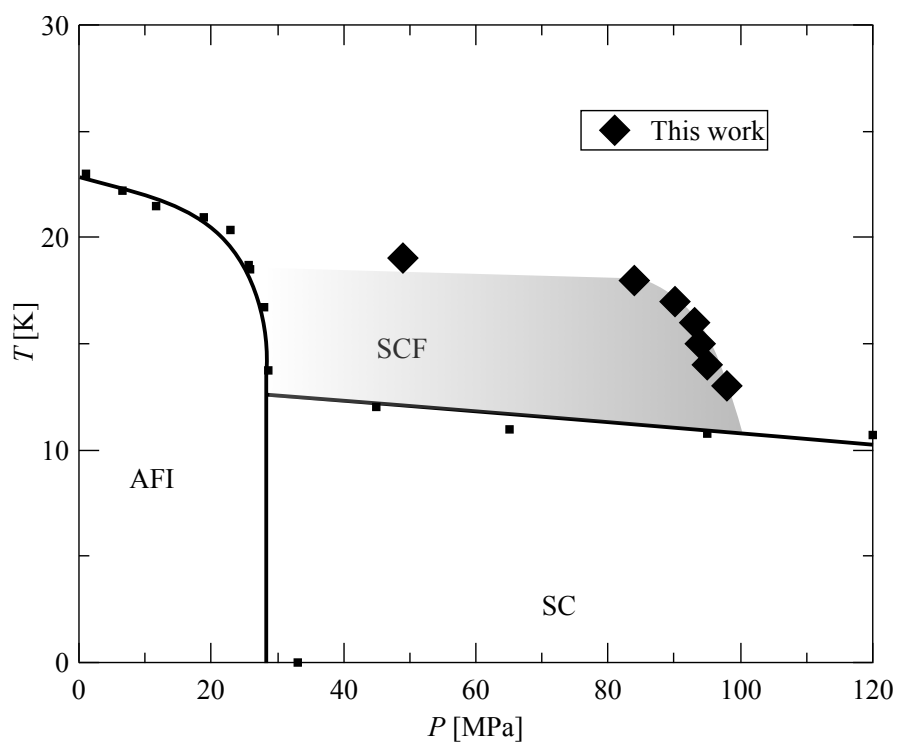


Figure 5.2.3: Onset pressure/temperature of SCF on phase diagram. Shaded region indicates SCF region.

## 6 Remarks

In this dissertation, we observed Mott transition by means of magnetisation for the first time. We also reported unique critical exponent,  $\beta = 1$ , as that of Mott transition in  $\kappa$ -(ET)<sub>2</sub>X system. This result agrees with a report from electrical conductivity measurement and theoretical prediction. This behaviour can be interpreted as emerging of quantum effect, which reflects lower critical endpoint compared to energy scale of Mott transition.

As a work on SCF, we observed rapid growth nature of SCF in  $\kappa$ -Br. Our result suggests magnetic susceptibility can detect bulk SCF behaviour with quite high sensitivity. We also found that onset of SCF has different pressure dependence compared to superconducting transition.

In investigation of magnetic ordering, we estimated zero-field  $T_N$  of  $\kappa$ -Cl and d8- $\kappa$ -Br for the first time. We also reported details of physical properties of d8- $\kappa$ -Cl and we find that d8- $\kappa$ -Cl shows critical behaviour which suggests 3D mechanism of ordering. From our detailed investigation by  $\mu$ SR method, we clarified the origin of magnetic ordering in this system.

# A Appendix

## A.1 Muon site estimation

The  $\mu$ SR spectrum is generally composed of contributions of electron spins and nuclear ones. In an analysis on the PM phase, we need to construct the model in which both contributions are taken into consideration. In the case of either absence of or undetectable magnetic fluctuation, the spectrum in the PM phase purely reflects the contribution of the nuclear dipoles. Such a state scarcely becomes a target of the research on electronic properties by  $\mu$ SR. However, a spectrum of such a state includes valuable information regarding the atomic environment of the implanted muons in the material. Furthermore, understanding of the origin of the spectrum may be available to the discussion on the electronic signal, appearing in different conditions or in related materials. In this respect, we focus on the  $\mu$ SR spectrum in the PM phase of organic materials.

In the main text, we discussed the results of  $\mu$ SR measurements at AFI phases of  $\kappa$ -Cl and d8- $\kappa$ -Br. Additionally, we concomitantly observed intriguing behaviours of the spectra in the PM phases. Using these datas, we developed the discussion on the origin of the PM spectrum in these materials. To discuss spectra in PM phases, we use the high-temperature spectra of  $\kappa$ -Cl and d8- $\kappa$ -Br. These materials are reported [56] to show glass transition at 70 and 75 K for  $\kappa$ -Cl and d8- $\kappa$ -Br, respectively. Therefore, an increase of the cooling speed at around these temperatures enhances the conformational disorder at low temperatures. We cooled down  $\kappa$ -Cl samples with cooling speed of 1 K/min and d8- $\kappa$ -Br samples with 0.4 K/min and  $\sim$ 100 K/min (quenched measurement, hereafter) to demonstrate the effect of conformational disorder.

Figure A.1.1 shows ZF  $\mu$ SR spectra at several temperatures for slow-cooled (1 K/min) h8- $\kappa$ -Cl [panel (a)], slow-cooled (0.4 K/min) d8- $\kappa$ -Br [panel (b)] and quenched ( $\sim$ 100 K/min) d8- $\kappa$ -Br [panel (c)]. At the lowest temperatures, all the spectra, represented by black symbols, show the precession behaviours, which suggest emerge of the magnetic orderings.

A precession signal in panel (c), which is newly-presented here, is weaker than that of slow-cooled d8- $\kappa$ -Br. This is attributable to the increase of the

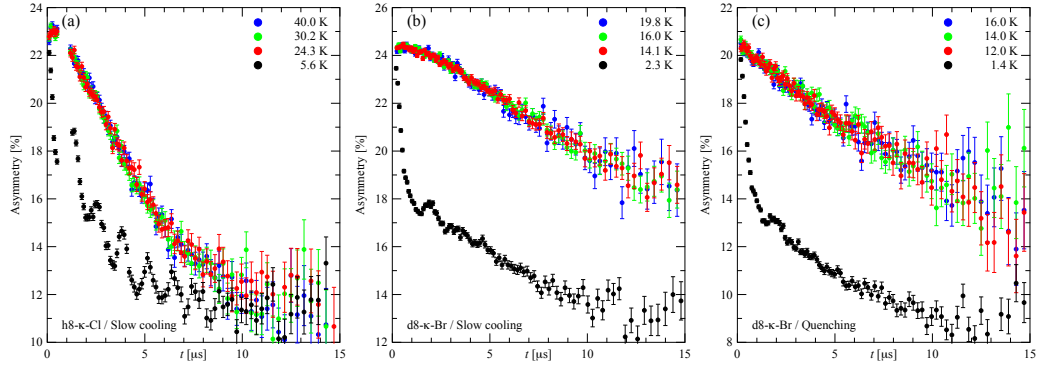


Figure A.1.1: Temperature dependence of  $\mu$ SR time spectra for slow-cooled (1 K/min) h8- $\kappa$ -Cl [panel (a)], slow-cooled (0.4 K/min) d8- $\kappa$ -Br [panel (b)] and quenched ( $\sim$ 100 K/min) d8- $\kappa$ -Br [panel (c)].

damping rate of this precession signal due to the inhomogeneous internal field. The conformational disorder enhanced by quenching is considered to be the origin for this inhomogeneity.

As observed in figure A.1.1, high-temperature spectra for the three panels, represented by blue, green and red symbols, do not show temperature dependence. These spectra seem to originate from the contributions of the nuclear dipoles. Low-temperature phases in the slow-cooling condition have been characterized as the magnetic phases with full [33] or almost full [60] volume fraction, which means that the sample asymmetries,  $A_s(t)$ , fulfills  $A_s(\infty) = 0$ . Hence, large gaps of d8- $\kappa$ -Br between the spectra of the ordered phase and PM one suggest a very slow relaxation of the PM-phase spectra compared to the relaxation of h8- $\kappa$ -Cl. It is emphasized that, because an accurate estimation of the background contribution is difficult for the spectrum in the PM phase, spectral information of the magnetically ordered phase is quite helpful to the quantitative evaluation of the PM phase spectra. In addition to such atomic-substitution dependence, the quenching seems to change the curvature of the PM-phase spectrum, as observed in panels (b) and (c). In order to gain a deeper insight into the origins of atomic-substitution and cooling-rate dependences of the PM spectrum, we plotted representative spectra normalized at the zero-time value after subtracting the background contributions in Fig. A.1.2.

Figure A.1.2 (a) show spectra of  $\kappa$ -Cl and d8- $\kappa$ -Br in the slow cooling condition, which highlights how the two spectra are different quantitatively. Basically,

relaxation spectra of the nuclear dipole system should be treated in terms of the Kubo-Toyabe function, [61]

$$G_{\text{KT}}(t) = \frac{1}{3} + \frac{2}{3}[1 - \Delta^2 t^2] \exp[-\frac{1}{2}\Delta^2 t^2] \quad (\text{A.1})$$

where  $t$  and  $\Delta$  are time and relaxation rate, respectively. This function is applicable to the system with homogeneous spin distribution and completely random spin direction. Note that such a system has a Gaussian distribution of the internal field. The time constant of Kubo-Toyabe function,  $\Delta$ , can be calculated by equations [62],

$$\Delta^2 = \sum_i \begin{cases} \frac{2}{3}\gamma_\mu^2 \mu_i^2 r_i^{-6} & (Q = 0) \\ \frac{2}{3}\gamma_\mu^2 \mu_i^2 r_i^{-6} & (Q \neq 0) \end{cases} \quad (\text{A.2})$$

where  $\gamma_\mu$  is the gyromagnetic ratio of muon,  $\mu_i$  are dipole moment of nuclei and  $r_i$  are distances between nuclei and muon. Within this framework, to understand the origin of the difference in the spectra, we need to consider the effect of two kinds of substitutions: hydrogen to deuterium at BEDT-TTF molecule and chlorine to bromine in anion layer. If distances between halogens and muons are so short as to affect the relaxation spectrum largely and almost unchanged by this substitution, the relaxation of d8- $\kappa$ -Br should be faster than that of h8- $\kappa$ -Cl. This is because bromines have larger dipolar moment than chlorines, as listed in Table A.1.1. The actual result is shown in Fig. A.1.2 (a) is just the opposite of this assumption. Accordingly, the other substitution, i.e. deuteration, is an only possible origin for the large difference of the relaxation spectra; the faster relaxation of h8- $\kappa$ -Cl is attributable to the larger dipole moment of hydrogen than that of deuterium. We should note that, two salts have the same crystal structure, similar lattice constants, and quite similar static potentials because valent of hydrogen and deuterium or chlorine and bromine is same. From this point, it is virtually certain that, if the muon sites are common between these isostructural salts, the majority of the muons of the two salts is situated closely to ethylene groups of BEDT-TTF.

Figure A.1.2 (b) shows cooling rate dependence of time spectrum of d8- $\kappa$ -Br. One of the distinct features of Kubo-Toyabe function is a convex shape at around  $t = 0$ . Whereas the slow-cooled d8- $\kappa$ -Br barely show such convex behaviour, the

	Dipole moment [ $\mu_N$ ]	quadruple moment	Natural abundance
H	2.79	$Q = 0$	-
D	0.86	$Q \neq 0$	-
$^{35}\text{Cl}$	0.82	$Q \neq 0$	0.76
$^{37}\text{Cl}$	0.68	$Q \neq 0$	0.24
$^{79}\text{Br}$	2.11	$Q \neq 0$	0.51
$^{81}\text{Br}$	2.27	$Q \neq 0$	0.49
$^{63}\text{Cu}$	2.88	$Q \neq 0$	0.69
$^{65}\text{Cu}$	3.07	$Q \neq 0$	0.31

Table A.1.1: Nuclear parameters of constituent nuclei of h8- $\kappa$ -Cl and d8- $\kappa$ -Br. [63] Dipole moments are displayed in unit of nuclear magneton,  $\mu_N$ .

spectrum of the quenched d8- $\kappa$ -Br is almost linear in the measured time windows. This behaviour is quite unusual as a time spectrum of the nuclear dipole system and rather similar to so-called static Lorentz Kubo-Toyabe function, [64]

$$G_{\text{LKT}}(t) = \frac{1}{3} + \frac{2}{3}[1 - at] \exp[-at] \quad (\text{A.3})$$

with relaxation rate,  $a$ . This function is applicable to the system of isotropic and static moment with Lorentzian distribution. The behaviour of dilute spin glass system is a famous example [62] of this function. In that way, the  $G_{\text{LKT}}$  behaviour of quenched d8- $\kappa$ -Br may be a key to elucidating the mechanism of the relaxation in these salts.

Nuclear dipoles in the present system, irrespective of cooling rate, can be regarded as a homogeneous spin system. Inevitably, one muon feels Gaussian-distributed internal field. In the case of the absence of the disorder in the arrangement of the nuclear dipole, other muons also feel similar Gaussian fields. The  $\mu\text{SR}$  spectra turn out to reflect such individual Gaussian field. On the other hand, in the case of strongly disordered nuclear dipole systems, individual muons feel various Gaussian field with various dispersions. The total distribution, which is a summation of such an individual Gaussian, possibly has Lorentzian-type shape. In this way, the strong deviation from the Gaussian behaviour in the quenched d8- $\kappa$ -Br is considered to originate from the disordered arrangement of the deuteriums, which is, of course, due to the freezing of the glassy conformation of ethylene groups.

Since the conformational disorder in ethylene groups is inferred to change Gaussian behaviour into Lorentzian one, it is worthy of examining a fitting analysis by using a function,

$$A(t) = e^{-(\sigma t)^\beta} \quad (\text{A.4})$$

where parameters  $\sigma$  and  $\beta$  represent a relaxation rate and curvature of the spectrum, respectively. This is because this function can formulate both of Gaussian behaviour ( $\beta = 2$ ) and Lorentzian one ( $\beta = 1$ ). The obtained values of two fitting parameters are summarized for all of PM-phase spectra in Table A.1.2. The variations in these parameters seem to accurately indicate the change of state or constituent in a molecular assembly. In the case of parameter  $\sigma$ , values of h8- $\kappa$ -Cl are almost three times larger than those of d8- $\kappa$ -Br in both cooling rates. Hence, this increase must be caused by the effect of the substitution of deuteriums by hydrogens. On the other hand, the value of  $\beta$  indicates Lorentzian-like behaviour ( $\beta \sim 1$ ) for the quenched experiment and larger but not exactly Gaussian-like behaviour for slow-cooled experiments ( $\beta \sim 1.5$ ). The libration mode of ethylene group in BEDT-TTF is not completely ordered even in the slow-cooled condition [56] and cause the wider distribution of internal field than Gaussian. Thus, the atomic environment around muons for the two salts has been understood through variation of the values of  $\sigma$  and  $\beta$ .

	$T$ [K]	$\sigma$ [ $1/\mu\text{s}$ ]	$\beta$
h8- $\kappa$ -Cl (1 K/min)	40.0	$0.175 \pm 0.002$	$1.57 \pm 0.03$
h8- $\kappa$ -Cl (1 K/min)	30.2	$0.178 \pm 0.002$	$1.55 \pm 0.03$
h8- $\kappa$ -Cl (1 K/min)	24.3	$0.172 \pm 0.002$	$1.53 \pm 0.03$
d8- $\kappa$ -Br (0.4 K/min)	19.8	$0.064 \pm 0.003$	$1.56 \pm 0.06$
d8- $\kappa$ -Br (0.4 K/min)	16.0	$0.062 \pm 0.002$	$1.52 \pm 0.04$
d8- $\kappa$ -Br (0.4 K/min)	14.1	$0.062 \pm 0.002$	$1.51 \pm 0.04$
d8- $\kappa$ -Br ( $\sim 100$ K/min)	16.0	$0.059 \pm 0.008$	$0.96 \pm 0.05$
d8- $\kappa$ -Br ( $\sim 100$ K/min)	14.0	$0.062 \pm 0.006$	$1.05 \pm 0.06$
d8- $\kappa$ -Br ( $\sim 100$ K/min)	12.0	$0.063 \pm 0.007$	$1.02 \pm 0.05$

Table A.1.2: Fitted parameters,  $\sigma$  and  $\beta$ , for the  $\mu\text{SR}$  spectra in PM phases.

After slow cooling, the h8- $\kappa$ -Cl and d8- $\kappa$ -Br salts show similar values of  $\beta$ . On the basis of above arguments, this fact seems to indicate that the degree of conformational disorder of the two salts is at a similar level. This is quite

reasonable because both salts show glass transition of ethylene groups. On the other hand, the disorder in the spin system in the ordered phase has been quite different between the two salts, as reported in  $^1\text{H}$ - and  $^{13}\text{C}$ -NMR studies [18, 27] as well as our  $\mu\text{SR}$  studies discussed in the main text. This contrast is attributable to the difference in the location of the phase diagram, as pointed out in our previous paper [60]. Roughly speaking, the structural disorder can be regarded as a distribution of “internal” pressure. Since pressure dependence of  $T_{\text{N}}$  of d8- $\kappa$ -Br is several times larger than that of h8- $\kappa$ -Cl, reflecting a steep decrease of  $T_{\text{N}}$  toward antiferromagnet-superconductor phase boundary, the spin system of d8- $\kappa$ -Br is strongly affected by the conformational disorder.

Next, we discuss the possible location of the muons by using obtained values of  $\sigma$ . As observed in Table A.1.2, cooling-rate dependence of  $\sigma$  is small, in contrast to the dependence of  $\beta$ . Hence, the value of  $\sigma$  in the case of absence of structural disorder will not deviate from the value of slow-cooling case largely. Therefore, we discuss possible locations of the muons while regarding  $\sigma$  in the slow-cooling case as  $\Delta$ . As mentioned earlier, we observed two kinds of precession signals in the ordered phases for the two salts. We proposed [33, 60] the center of six-membered rings of BEDT-TTF as a strong candidate of the other muon site ( $B_{\mu 1}$ ) through comparing the internal field calculated using the value of the local moment per dimer estimated by  $^{13}\text{C}$ -NMR [18, 20, 27] with experimental value. We calculated<sup>1</sup> the expected  $\Delta$  at this site with the values in Table A.1.1 using Eq. (2) and obtained the values of  $0.21 \mu\text{s}^{-1}$  and  $0.054 \mu\text{s}^{-1}$  for h8- $\kappa$ -Cl and d8- $\kappa$ -Br, respectively. These values show good coincidence with the experimental values ( $\sim 0.17 \mu\text{s}^{-1}$  and  $\sim 0.062 \mu\text{s}^{-1}$  for h8- $\kappa$ -Cl and d8- $\kappa$ -Br). Although there are at least two muon sites for the two materials, the observed spectra may be largely affected by the contribution of this  $B_{\mu 1}$  site. Indeed, the population<sup>2</sup> of this site is larger (27% and 41% for h8- $\kappa$ -Cl and d8- $\kappa$ -Br) than that of the  $B_{\mu 2}$  site (15% and 12% for h8- $\kappa$ -Cl and d8- $\kappa$ -Br).

From these results, we can draw some conclusion. Firstly, at least in  $\kappa$ -(ET)<sub>2</sub>X, deuteration on BEDT-TTF molecule causes slowdown of relaxation due

<sup>1</sup>Since atomic coordinates of hydrogen or deuterium in h8- $\kappa$ -Cl or d8- $\kappa$ -Br were not reported we estimated such positions on the basis of the results of neutron diffraction [65] on  $\beta'$ -(BEDT-TTF)<sub>2</sub>ICl<sub>2</sub>.

<sup>2</sup>Populations were estimated by multiplying the weightings of the precession signals by 1.5.

to the nuclear dipole. Such situation makes investigation of states of electronic spin easier, because of slowdown actually works as a suppression of background components. For example, antiferromagnet [66, 67]  $\beta'$ -(BEDT-TTF)<sub>2</sub>ICl<sub>2</sub>, spin-liquid candidate [68, 69]  $\kappa$ -(BEDT-TTF)<sub>2</sub>Cu<sub>2</sub>(CN)<sub>3</sub> and non-Fermi liquid system [70, 71]  $\kappa$ -(BEDT-TTF)<sub>4</sub>Hg<sub>2.89</sub>Br<sub>8</sub> are worth of examine with deuterated BEDT-TTF molecules. Secondary, we demonstrated that, we can detect the degree of the structural disorder by the shape of PM spectra. Such application of  $\mu$ SR is not widely reported. Such estimation of disorder may be applied to saturated-band organic polymers for investigation of crystallinity.

In summary, we demonstrated that the deuteration and quenching significantly vary the  $\mu$ SR spectra in the PM phase of  $\kappa$ -type BEDT-TTF compounds. These findings suggest that the PM-phase spectra of these materials are dominated by the contribution of the nuclear dipole of hydrogen (or deuterium). In addition, quenching changes the total distribution of the nuclear dipole fields into the Lorentzian distribution. Through these findings, we confirmed the common degree of conformational disorder between h8- $\kappa$ -Cl and d8- $\kappa$ -Br and the validity of the muon sites proposed in our published works. Possible applications of such deuteration method and structural-disorder evaluation method to  $\mu$ SR studies in other materials were supposed.

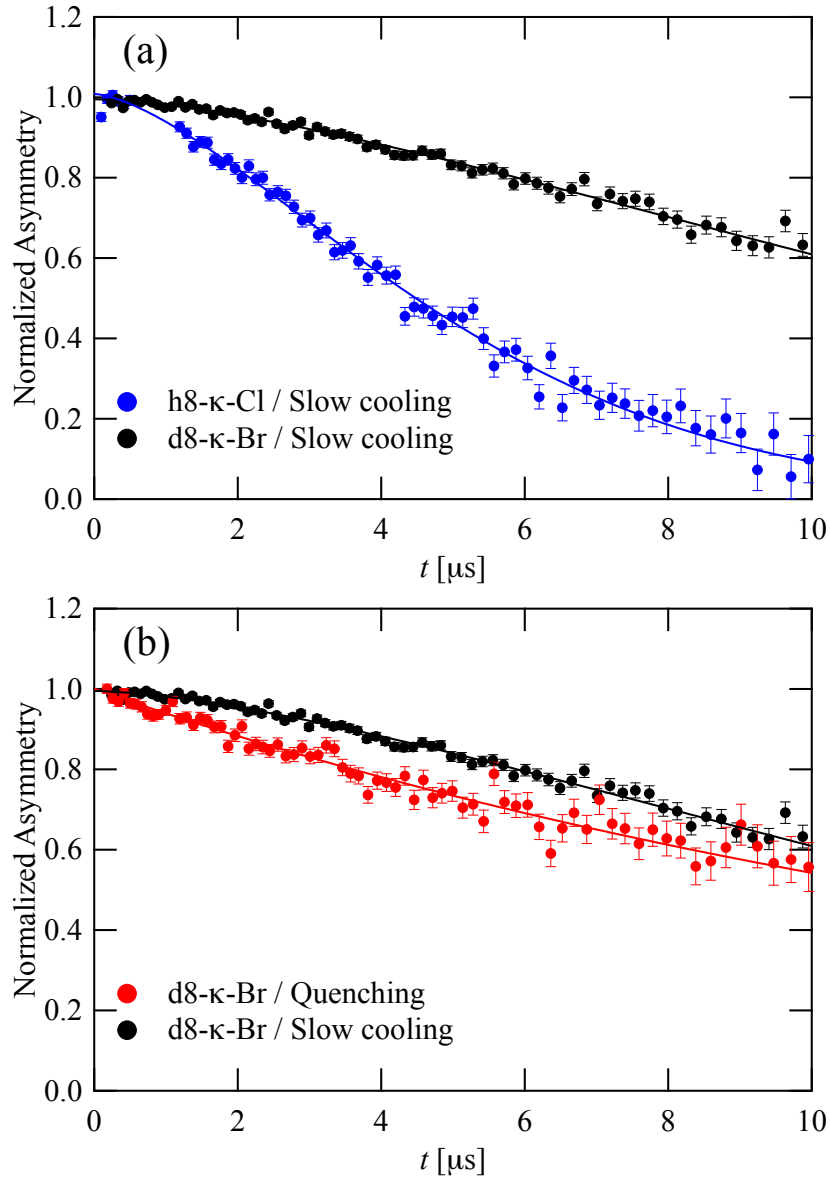


Figure A.1.2: Atomic-substitution dependence of  $\mu\text{SR}$  spectrum (a) and cooling-rate dependence of spectrum of d8- $\kappa$ -Br (b). Solid lines are fitting lines of Eq. (4).

## References

- [1] T. Ishiguro, K. Yamaji, and G. Saito, *Organic Superconductors (Springer Series in Solid-State Sciences)* (Springer, 2001).
- [2] N. Toyota, M. Lang, and J. Müller, *Low-Dimensional Molecular Metals (Springer Series in Solid-State Sciences)* (Springer, 2007).
- [3] S. Kagoshima, H. Nagasawa, and T. Sambongi, *One-Dimensional Conductors (Springer Series in Solid-State Sciences)* (Springer, 2012).
- [4] S. Blundell, *Magnetism in Condensed Matter (Oxford Master Series in Physics)* (Oxford University Press, 2001).
- [5] M. Tinkham, *Introduction to Superconductivity: Second Edition (Dover Books on Physics)* (Dover Publications, 2004).
- [6] J. F. Annett, *Superconductivity, Superfluids, and Condensates (Oxford Master Series in Condensed Matter Physics)* (Oxford University Press, 2004).
- [7] T. Takahashi, T. Erata, N. Nishida, and H. Bando, *Bussei sokutei no shinpo I (Advancement of physical property measurement I) [in Japanese]* (Maruzen, 1997).
- [8] U. Geiser, A. J. Schultz, H. H. Wang, D. M. Watkins, D. L. Stupka, J. M. Williams, J. E. Schirber, D. L. Overmyer, D. Jung, J. J. Novoa, and M. H. Whangbo, *Physica C: Superconductivity* **174**, 475 (1991).
- [9] K. Kanoda, *Hyperfine Interactions* **104**, 235 (1997).
- [10] S. Lefebvre, P. Wzietek, S. Brown, C. Bourbonnais, D. Jérôme, C. Mézière, M. Fourmigue, and P. Batail, *Phys. Rev. Lett.* **85**, 5420 (2000).
- [11] D. B. McWhan, A. Menth, J. P. Remeika, W. F. Brinkman, and T. M. Rice, *Phys. Rev. B* **7**, 1920 (1973).
- [12] P. Limelette, A. Georges, D. Jérôme, P. Wzietek, P. Metcalf, and J. M. Honig, *Science* **302**, 89 (2003).
- [13] L. P. Kadanoff, W. Götze, D. Hamblen, R. Hecht, E. A. S. Lewis, V. V. Palciauskas, M. Rayl, J. Swift, D. Aspnes, and J. Kane, *Rev. Mod. Phys.* **39**, 395 (1967).
- [14] C. Castellani, C. D. Castro, D. Feinberg, and J. Ranninger, *Phys. Rev. Lett.* **43**, 1957 (1979).

- [15] G. Kotliar, E. Lange, and M. J. Rozenberg, *Phys. Rev. Lett.* **84**, 5180 (2000).
- [16] F. Kagawa, K. Miyagawa, and K. Kanoda, *Nature* **436**, 534 (2005).
- [17] M. Imada, *Phys. Rev. B* **72**, 075113 (2005).
- [18] K. Miyagawa, A. Kawamoto, Y. Nakazawa, and K. Kanoda, *Phys. Rev. Lett.* **75**, 1174 (1995).
- [19] U. Welp, S. Fleshler, W. K. Kwok, G. W. Crabtree, K. D. Carlson, H. H. Wang, U. Geiser, J. M. Williams, and V. M. Hitsman, *Phys. Rev. Lett.* **69**, 840 (1992).
- [20] D. Smith, S. De Soto, C. Slichter, J. Schlueter, A. Kini, and R. Daugherty, *Phys. Rev. B* **68**, 024512 (2003).
- [21] F. Kagawa, Y. Kurosaki, K. Miyagawa, and K. Kanoda, *Phys. Rev. B* **78**, 184402 (2008).
- [22] P. Lunkenheimer, J. Müller, S. Krohns, F. Schrettle, A. Loidl, B. Hartmann, R. Rommel, M. de Souza, C. Hotta, J. A. Schlueter, and M. Lang, *Nat Mater* **11**, 755 (2012).
- [23] A. Antal, T. Feher, A. Janossy, E. Tatrai-Szekeres, and F. Fulop, *Phys. Rev. Lett.* **102**, 086404 (2009).
- [24] N. D. Mermin, *Physical Review* **176**, 250 (1968).
- [25] Y. Nakazawa and K. Kanoda, *Phys. Rev. B* **53**, R8875 (1996).
- [26] S. Yamashita and Y. Nakazawa, *J Therm Anal Calorim* **99**, 153 (2009).
- [27] A. Kawamoto, K. Miyagawa, and K. Kanoda, *Phys. Rev. B* **55**, 14140 (1997).
- [28] K. Miyagawa, A. Kawamoto, and K. Kanoda, *Phys. Rev. Lett.* **89**, 017003 (2002).
- [29] M. Tokumoto, N. Kinoshita, Y. Tanaka, and H. Anzai, *J. Phys. Soc. Jpn.* **60**, 1426 (1991).
- [30] H. Taniguchi, A. Kawamoto, and K. Kanoda, *Phys. Rev. B* **59**, 8424 (1999).
- [31] X. Su, F. Zuo, J. A. Schlueter, M. E. Kelly, and J. M. Williams, *Phys. Rev. B* **57**, R14056 (1998).
- [32] N. Yoneyama, T. Sasaki, T. Nishizaki, and N. Kobayashi, *J. Phys. Soc. Jpn.* **73**, 184 (2004).

- [33] M. Ito, T. Uehara, H. Taniguchi, K. Satoh, Y. Ishii, and I. Watanabe, *J. Phys. Soc. Jpn.* **84**, 053703 (2015).
- [34] D. E. Prober, M. R. Beasley, and R. E. Schwall, *Phys. Rev. B* **15**, 5245 (1977).
- [35] R. Bel, K. Behnia, and H. Berger, *Phys. Rev. Lett.* **91**, 066602 (2003).
- [36] N. P. Armitage, P. Fournier, and R. L. Greene, *Rev. Mod. Phys.* **82**, 2421 (2010).
- [37] Z. A. Xu, N. P. Ong, Y. Wang, T. Kakeshita, and S. Uchida, *Nature* **406**, 486 (2000).
- [38] H. Kontani, *Phys. Rev. Lett.* **89**, 237003 (2002).
- [39] I. Ussishkin, S. Sondhi, and D. Huse, *Phys. Rev. Lett.* **89**, 287001 (2002).
- [40] V. J. Emery and S. A. Kivelson, *Nature* **374**, 434 (1995).
- [41] M.-S. Nam, A. Ardavan, S. J. Blundell, and J. A. Schlueter, *Nature* **449**, 584 (2007).
- [42] A. M. Kini, U. Geiser, H. H. Wang, K. D. Carlson, J. M. Williams, W. K. Kwok, K. G. Vandervoort, J. E. Thompson, and D. L. Stupka, *Inorg. Chem.* **29**, 2555 (1990).
- [43] S. Tsuchiya, J.-i. Yamada, S. Tanda, K. Ichimura, T. Terashima, N. Kurita, K. Kodama, and S. Uji, *Phys. Rev. B* **85**, 220506 (2012).
- [44] S. Tsuchiya, J.-i. Yamada, T. Terashima, N. Kurita, K. Kodama, K. Sugii, and S. Uji, *J. Phys. Soc. Jpn.* **82**, 064711 (2013).
- [45] M.-S. Nam, C. Mézière, P. Batail, L. Zorina, S. Simonov, and A. Ardavan, *Sci. Rep.* **3**, 3390 (2013).
- [46] I. Watanabe, Y. Ishii, T. Kawamata, T. Suzuki, F. L. Pratt, R. Done, M. Chowdhury, C. Goodway, J. Dreyer, C. Smith, and M. Southern, *Physica B: Condensed Matter* **404**, 993 (2009).
- [47] S. J. Blundell, *Appl Magn Reson* **13**, 155 (1997).
- [48] S. J. Blundell, *Contemporary Physics* **40**, 175 (1999).
- [49] T. Misawa, Y. Yamaji, and M. Imada, *J. Phys. Soc. Jpn.* **75**, 083705 (2006).

- [50] T. Misawa and M. Imada, *Phys. Rev. B* **75**, 115121 (2007).
- [51] H. Taniguchi, K. Kanoda, and A. Kawamoto, *Phys. Rev. B* **67**, 014510 (2003).
- [52] Y. Nogami, J. P. Pouget, H. Ito, T. Ishiguro, and G. Saito, *Solid State Communications* **89**, 113 (1994).
- [53] H. Akutsu, K. Saito, and M. Sorai, *Phys. Rev. B* **61**, 4346 (2000).
- [54] T. Sasaki, N. Yoneyama, A. Matsuyama, and N. Kobayashi, *Phys. Rev. B* **65**, 060505 (2002).
- [55] K. Frikach, M. Poirier, M. Castonguay, and K. D. Truong, *Phys. Rev. B* **61**, R6491 (2000).
- [56] J. Müller, M. Lang, F. Steglich, J. A. Schlueter, A. M. Kini, and T. Sasaki, *Phys. Rev. B* **65**, 144521 (2002).
- [57] W. K. Kwok, U. Welp, K. D. Carlson, G. W. Crabtree, K. G. Vandervoort, H. H. Wang, A. M. Kini, J. M. Williams, D. L. Stupka, L. K. Montgomery, and J. E. Thompson, *Phys. Rev. B* **42**, 8686 (1990).
- [58] M. Lang, F. Steglich, N. Toyota, and T. Sasaki, *Phys. Rev. B* **49**, 15227 (1994).
- [59] D. Podolsky, S. Raghu, and A. Vishwanath, *Phys. Rev. Lett.* **99**, 117004 (2007).
- [60] T. Uehara, M. Ito, J. Angel, J. Shimada, N. Komakine, T. Tsuchiya, H. Taniguchi, K. Satoh, K. Triyana, Y. Ishii, and I. Watanabe, *J. Phys. Soc. Jpn.* **85**, 024710 (2016).
- [61] R. Kubo and T. Toyabe, *Magnetic Resonance and Relaxation* (North-Holland, Amsterdam, 1967).
- [62] Y. Uemura, T. Yamazaki, D. Harshman, M. Senba, and E. Ansaldo, *Phys. Rev. B* **31**, 546 (1985).
- [63] N. J. Stone, *Atomic Data and Nuclear Data Tables* **90**, 75 (2005).
- [64] R. Kubo, *Hyperfine Interactions* **8**, 731 (1981).
- [65] M. Watanabe, private communication.

- [66] N. Yoneyama, A. Miyazaki, T. Enoki, and G. Saito, *Synthetic metals* **86**, 2029 (1997).
- [67] K. Satoh, H. Taniguchi, A. Kawamoto, and W. Higemoto, *Physica B: Condensed Matter* **374-375**, 99 (2006).
- [68] S. Ohira, Y. Shimizu, K. Kanoda, and G. Saito, *J Low Temp Phys* **142**, 153 (2007).
- [69] F. L. Pratt, P. J. Baker, S. J. Blundell, T. Lancaster, S. Ohira-Kawamura, C. Baines, Y. Shimizu, K. Kanoda, I. Watanabe, and G. Saito, *Nature* **471**, 612 (2011).
- [70] R. N. Lyubovskaya and E. I. Zhilyaeva, *JETP Lett.* **46**, 25 (1987).
- [71] K. Satoh, H. Fujita, K. Katayama, H. Taniguchi, T. U. Ito, K. Ohishi, and W. Higemoto, *Physica B: Condensed Matter* **404**, 597 (2009).